Department of Electronic and Electrical Engineering
University College London
University of London

Amplitude, temperature, and frequency dependence of quantum pumps in semiconductor heterostructures

Hume Howe
Supervisor: Prof. Sir Michael Pepper

Submitted in fulfilment of the requirements
for the degree of Doctor of Philosophy
at the University of London

June 2015

I, Hume Howe, declare that the work presented in this thesis is my own. Where information has been obtained from other sources, I declare this has been clearly indicated in the thesis.

Publications

Work directly pertaining to the subject matter of this thesis:
J. D. Fletcher, P. See, H. Howe, M. Pepper, S. P. Giblin, J. P. Griffths, G. A. C. Jones, I. Farrer, D. A. Ritchie, T. J. B. M. Janssen, and M. Kataoka
'Clock-controlled emission of single-electron wave packets in a solid-state circuit'
Phys. Rev. Lett., vol. 111, p. 216807, Nov 2013.

Work not pertaining to the subject matter of this thesis, but to the developed measurement setup:
A. Mehonic, A. Vrajitoarea, S. Cueff, S. Hudziak, H. Howe, C. Labbe, R. Rizk, M. Pepper, and A. J. Kenyon
'Quantum conductance in silicon Oxide resistive memory devices'
Sci. Rep., vol. 3, Sep 2013.

Abstract

In the rapidly growing field of integrated quantum devices, two particular areas of interest are the development of an on-chip cryogenic current comparator (CCC) for completing the metrological triangle and the development of integrated devices for fast qubit operations [1]. This thesis aims to significantly further our understanding of a quantum pump, a device integral to the CCC and potentially critical for realising fast qubit operations. A quantum pump is a device that transfers a discrete number of electrons between two electrically isolated regions when a potential barrier is cyclically oscillated. Initially, quantum pumps were single electron turnstile devices, which were limited in operational frequency by the Coulomb potential of the turnstile. Modern quantum pumps, utilising a dynamic quantum dot in a 2-dimensional electron gas (2DEG), are not limited by frequency. The fast operation of these modern pumps makes them very promising devices for accurately measuring the electron charge and performing fast qubit operations. In this study, we address the technical challenges of measuring a AlGaAs/GaAs quantum pump and detail the processing and measurement setup. One of the challenges is rectified current swamping pump current. We develop a model for the rectified current and investigate ways to suppress it. We then show how the accuracy of a quantum pump changes as a function of amplitude, temperature, and frequency, and develop a model towards explaining the changes.

Acknowledgements

I have so many people to thank that doing you all justice would put me over my word limit, so apologies to those I have had the pleasure of working with who are not mentioned. First, I would like to thank my primary supervisor Prof Sir Michael Pepper, who has always made himself available despite his busy schedule. The PhD has been a difficult one, with immense setbacks, but the support he has given me, and the trust he has placed in me to do good work throughout, has sustained my optimism during the hard parts. For that I am very thankful, and look forward to working with him in the future. Next, I would like thank Dr. David English. He has been my advisor and friend, and this work would be nowhere without him. I've learnt a lot from him and learnt a lot with him. The above I extend to Dr. Mark Blumenthal, who I consider my co-advisor. It's been a great team dynamic, and I look forward to our continual collaborative work.

In NPL, where I spent my first year and learnt a lot from the great QD group there: Dr. Masaya Kataoka, Dr. Jon Fletcher, Dr. Stephen Giblin, and Dr. J. T. Jannsen. I would very much like to visit again and catch up.

In the LCN, where I moved to set up pump measurements, I would like to thank Dr. Sanjeev Kumar, who had task of setting up a new lab. It was under Sanjeev that I learnt to be organised and structured. Also to Dr. Neil Curson, who has been ever supportive.

In the Cavendish laboratory, where I fabricated devices, I have so many to thank. Dr. Patrick See, who fabricated some working devices for us when we were initially troubleshooting the processing and measurement steps. He is an exceptional device fabricator who produces pumps with a very high yield. The wafers were grown by Dr. Ian Farrer and Dr. Harvey Beere. Harvey has been exceptional in always taking the time to discuss points of wafer growth with me and I have enjoyed all of our discussions. I thank Jonathan Griffiths, who runs the EBL, for his advice and skills, and Richard Hall for his EBL during his time there. Beyond fabrication, I'd like to thank Prof Chris Ford, who I don't think I've ever seen not helping a student in some way or another. I certainly benefitted from my discussions with him. I'd like to thank Egle for showing us how to use the fridge, and Joanna, Yash, Jessop, Ugo, Eric, David, Joel, Chong, and many more

for making the Cavendish homely. Lastly for the Cavendish, a special thanks to Dr. Graham Creeth and Yilmaz Gul for all the help inside and outside of the cleanroom.

Outside of these, I thank Dr. Frank Arhles for his kind permission to use Modulab.

Lastly, to all my friends from Oxford and UCL, and my sister, Sei Howe, who have put up with my absence over the past 4 years. I will make time.

For my parents
Mendy Howe & James Howe

Contents

List of Figures

Acronyms

2DEG 2-dimensional electron gas

AB Aharanov-Bohm

AC Alternating current

AWG Arbitrary waveform generator

BNC Bayonet NeillConcelman

CCC Cryogenic current comparator

DAC Digital to analogue converter

DC Direct current

DI Deionized

DMM Digital multimeter

DOS Density of states

DX Donor impurity

EBL Electron beam lithography

ESD Electrostatically sensitive device

GE General Electric (company)

GF Gate filter

HBT Hanbury-Brown-Twiss

HCL Hydrochloric acid

HEMT High electron mobility transistor

HF Hydroflouric acid

HOM Hong-Ou-Mandel

IPA Isopropanol

JE Josephson effect

LCC Leadless Chip Carrier

LCN London Centre for Nanotechnology

LOR lift-off resist

MBE Molecular beam epitaxy

MOS Metal-oxide-semiconductor

MS Metal-semiconductor

NPL National Physical Laboratory

PCB Printed circuit board

PMMA poly-methyl-methacrylate

PR photoresist

PTB Physikalisch-Technische Bundesanstalt

PTR Pulse tube refrigerator

QHE Quantum Hall effect

QMT Quantum metrological triangle

QPC Quantum point contact

RF Radio frequency

RTA Rapid thermal annealer

SAW Surface acoustic wave

SEM Scanning electron microscope

SET Single electron transport

SI Le Systéme International

SMA Subminature version A

SMU Source-measure unit

UDC Universal decay cascade

UCL University College London

UV Ultraviolet

WKB Wentzel Kramers Brillouin

Chapter 1

Introduction

1.1 Introduction

Collaborative science requires that all measurements are made with reference to invariable and known standards. In the early 1800's when the metric system was first introduced, Gauss promoted the use of all measurements based on the metric system for mass, length, time, and later current [2]. These four developed into the seven Le Systéme International (SI) base units (meter, kg, second, ampere, kelvin, mole, candela) from which all other SI units are derived. As measurements can only be made as precisely as the units they are based on, the precision of the SI units must better the precision of measurements. Towards this, the SI units are redefined from time to time based on increasingly accurate reproducible measurements. As the limiting factors on reproducible measurements can be a function of the environment in which the experiments are made, it is best to define the SI units in terms of universal constants, which are invariable. The ampere, the unit for measuring current, has yet to be defined in terms of universal constants; as it is part of every derived unit of electromagnetism, defining it invariably and measuring it to a high degree of accuracy is of major importance [3]. The focus of many metrological institutions is to redefine the ampere in terms of the fundamental constant of charge, e. The most promising device for achieving this is the quantum pump.

1.2 The metrological triangle

The quantum metrological triangle (QMT) is a relationship between three electrical standards (the Josephson voltage standard K_J, the Quantum Hall resistance standard R_K, and the current standard Q_X), and the fundamental constants of charge, e, and Plank's constant, h. The triangle links the voltage standard, resistance standard, and current standard through Ohm's law, $V = IR$, and provides a consistency check for the fundamental constants, (Figure 1.1).

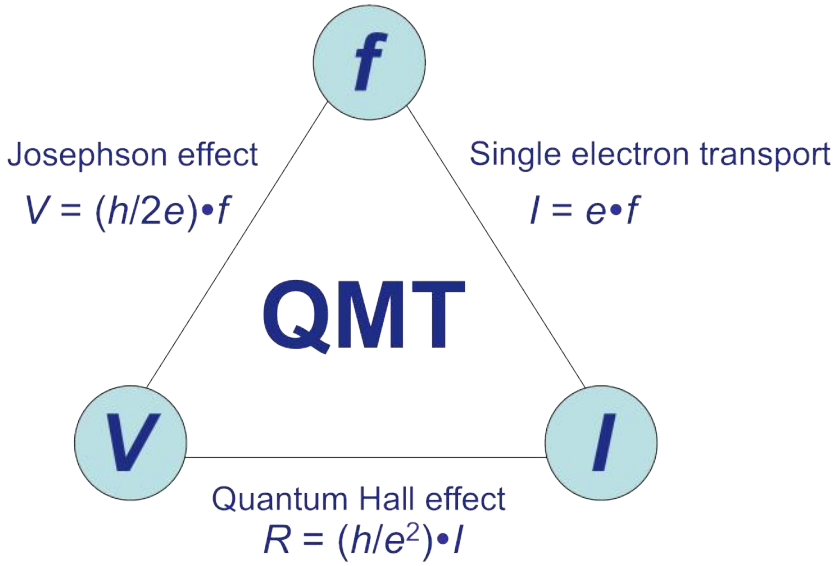

Figure 1.1: A diagram of the Quantum Metrological Triangle relating relating voltage V, resistance R, and current I by Ohms law $V = IR$, frequency f, the electron charge e and Planck's constant h.

The QMT was first proposed in 1885 when work on the Josephson effect (JE) suggested that it could be used as a voltage standard [4]. From the JE, $K_J = 2e/h$, and from the Quantum Hall effect (QHE), $R_K = h/e^2$. These were accepted as voltage and resistance standards in 1990 with the values $K_{\text{J-90}} = 483597.9\,\text{GHz/V}$ with a relative uncertainty of 8.5×10^{-8}, and $R_{\text{K-90}} = 25,812.8074434\,\Omega$ with a relative uncertainty of 2×10^{-9}. K_J, R_K, and Q_X are related by Ohm's law, and closing the metrological triangle requires $K_J \times R_K \times Q_X = 2$. As the uncertainty in R_K varies with the resistance of the device, for Q_X to be used as a current standard, the relative uncertainty for a current larger than 1 nA must be less that 10^{-8}.

Several institutions worldwide are attempting to reach the required level of accuracy in measuring current. In the UK the dedicated centre for metrological research, the National Physical Laboratory (NPL), is using their considerable expertise and in-house calibrated frequency and resistance standards to measure current extremely accurately, so contributing to closing the metrological triangle. NPL collaborates with the Cavendish laboratory, Cambridge, who contribute their molecular beam epitaxy (MBE) and fabrication expertise, and more recently with London Centre for Nanotechnology (LCN) at University College London (UCL).

There are two proposed devices for realising a new standard for the Ampere: the quantum phase slip [5], which is an analogue of the Josephson junction with a superconducting 1D wire rather than a tunnel junction, and the quantum pump.

1.3 Quantum pump overview

A quantum pump is a device that generates quantised current as a function of the frequency of an oscillating gate. Initially, quantum pumps were developed from single electron turnstile devices fabricated in metal-oxide tunnel junctions; these metal-oxide devices were succeeded by semiconductor pumps, surface acoustics wave pumps (SAWs), and most recently by a pump that has a pair of metal gates fabricated on top of a narrow channel of two dimensional electron gas (2DEG), hereafter simply called the quantum pump. This type of quantum pump is the main focus of this work. Figure 1.2 shows a scanning electron microscope (SEM) image of the quantum pump used most in this work, the geometry of which is different from that of a normal pump. A normal pump can be formed using the 2 leftmost gates, but our pump has a different geometry in that the exit gate is a split gate. A quantum dot (yellow) is formed between the radio-frequency (RF) entrance (red) and exit gates (green). The yellow arrow indicated the direction of pumping. Despite the different geometry, the basic pumping operation is the same as that of a normal pump.

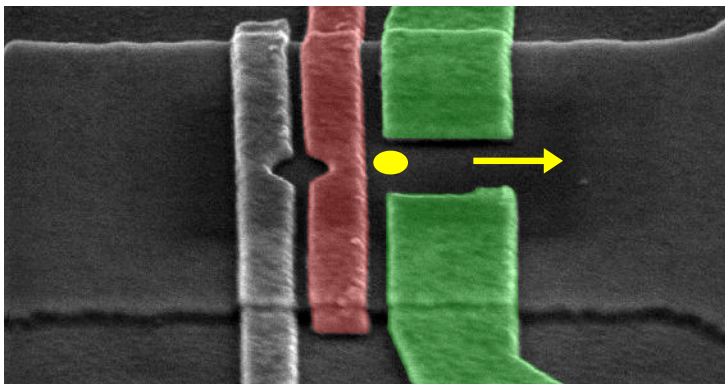

Figure 1.2: A false-colour SEM image of a quantum pump device in a split-gate configuration with the entrance RF gate (red), exit gates (green), and the quantum dot and the direction of pumping (yellow)

Figure 1.3 shows the basic operation of the pump, with one of the gates fixed at a negative voltage to form a barrier, and the other gate oscillated to pump the electrons over that barrier. It shows an electron being collected from the Fermi sea and transferred over the fixed exit barrier.

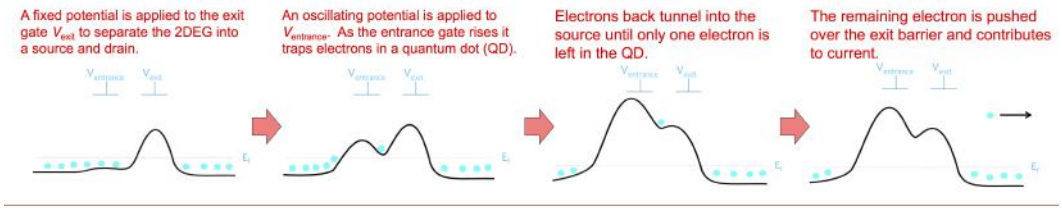

Figure 1.3: A diagram of the quantum pump operation showing an electron being collected from the Fermi sea and transferred over the fixed exit barrier.

Chapter 2

Theory

2.1 Introduction

The physics of electron transport in a device changes with its size. In the macroscopic regime, where the characteristic lengths (e.g. mean free path and phase coherence length) are smaller than the device dimensions, classical physics applies. In the mesoscopic regime, where characteristic lengths and the sample dimensions are comparable, the quantum mechanical nature of electrons needs to be considered and semi-classical physics applies, which has elements of both classical and quantum physics. The electrons behave mostly classically, but have a quantised energy distribution, called the density of states (DOS), that depends on the number of dimensions in which they are free to move.

This chapter is a review of physics relevant to etched and gated low-dimensional semiconductor heterostructures. It covers the relevant length scales, the density of states (DOS) for various dimensions, semiconductor-semiconductor interfaces (2DEG heterostructures), metal-semiconductor interfaces (Schottky barriers, Fermi pinning, and Ohmics), the Coulomb blockade, the universal decay cascade model (UDC). The material has been sourced from a number of textbooks and teaching modules [6–8].

2.2 Length scales

Different length scales are important because the energy spacing changes as the size of the device changes. In a bulk material, an electron is free to move in three dimensions. When the sample size becomes comparable with a characteristic length, the dimensions are reduced, and the DOS changes.

The most important characteristic length is the mean free path λ, which is the average distance an electron will travel before scattering. At very low temperatures, electrons are assumed to be at the Fermi energy. The mean free path of electrons at this energy, $\lambda_F = v_F\tau$, where v_F is the Fermi velocity and τ is the average scattering time. An electron trapped in a quantum well of potential V and width L, with $L < \lambda$, becomes confined in that direction. The next most important length is the phase coherence length l_Φ, which is the length beyond which any information about the electron's original phase is lost.

2.3 Bulk (3D)

2.3.1 Density of states (3D)

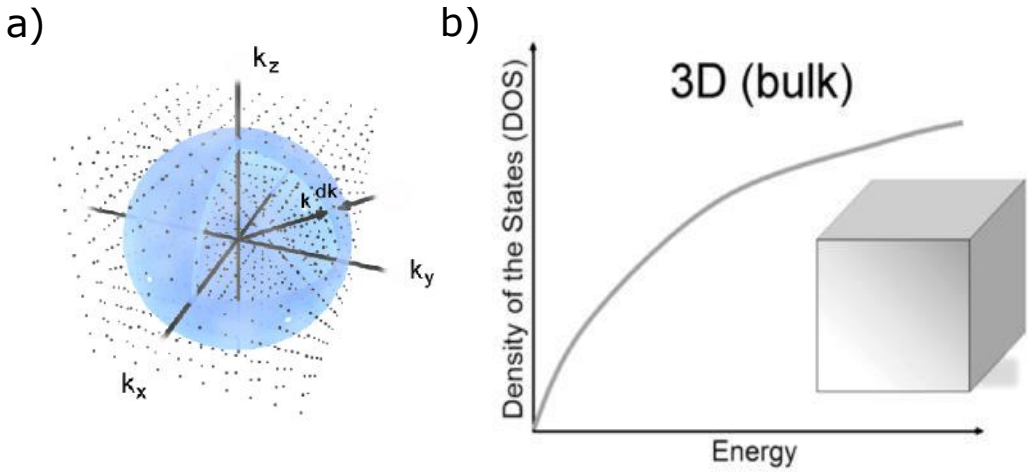

Figure 2.1: (a) The region of available **k**. (b) The 3D DOS. [Images taken from [9] and [10]].

The characteristics of a bulk semiconductor are explained by the nearly free electron model and tight binding model, which lead to the theory of band structures. When the electrons are not restricted, $\mathbf{k}^2 = (k_x^2 + k_y^2 + k_z^2)$. Figure 2.1a shows the available $\mathbf{k}$ states, which are in the region between surface $\mathbf{k}$ and $\mathbf{k}+\mathrm{d}\mathbf{k}$; the total volume of the region $v_{3\mathrm{D}} = 4\pi|\mathbf{k}|^2\mathrm{d}\mathbf{k}$. The volume of one state is $V_{3\mathrm{D}} = (2\pi/L)^3$.

The number of states, $g_{3\mathrm{D}}(\mathbf{k})\mathrm{d}\mathbf{k}$, that can fit within this region is given by the total volume divided by the volume of one state.

$$g_{3\mathrm{D}}(\mathbf{k})\mathrm{d}\mathbf{k} = 2 \times \frac{v_{3\mathrm{D}}}{V_{3\mathrm{D}}} = \frac{|\mathbf{k}|^2 L^3}{\pi^2}\mathrm{d}\mathbf{k}. \tag{2.1}$$

$g_{3\mathrm{D}}(\mathbf{k})\mathrm{d}\mathbf{k}$ contains a factor of 2 to account for spin degeneracy. To calculate the density of states in terms of energy we use the solution to the time-independent Schrodinger equation

$$\left[-\frac{\hbar^2}{2m^*}\nabla^2 + V(r) \right]\Psi(r) = E\Psi(r). \tag{2.2}$$

The solution is $E = \frac{\hbar^2\mathbf{k}^2}{2m^*}$. Solving for $\mathbf{k}$ and $\mathrm{d}\mathbf{k}$

$$|\mathbf{k}| = \sqrt{\frac{2Em^*}{\hbar^2}} \tag{2.3}$$

and

$$\mathrm{d}\mathbf{k} = \frac{1}{2}\sqrt{\frac{2m^*}{\hbar^2 E}}\mathrm{d}E. \tag{2.4}$$

Substituting equations 2.3 and 2.4 into 2.1 and dividing by the volume, L^3, gives the density of states in energy per unit volume, (Figure 2.1b)

$$g_{3\mathrm{D}}(E)\mathrm{d}E = \left(\frac{2m^*}{\hbar^2}\right)^{3/2}\frac{\sqrt{E}}{2\pi^2}\mathrm{d}E. \tag{2.5}$$

2.4 Heterostructures (2D)

2.4.1 2 dimensional electron gas (2DEG)

Much of semiconductor physics is done in a 2 dimensional electron gas (2DEG), where the electrons are confined to a 2D plane by a potential well. One way to create the well is to modulation-dope a heterostructure; when two semiconductors with different band gaps are brought into contact (a heterostructure) and the semiconductor with the larger band gap is doped (modulation-doping), a triangular potential well is formed, (Figure 2.2). If the width of this triangular well is small compared with λ, a sub-band is formed and electrons are trapped in the XY plane. Additionally, when the dopants are spatially separated from the 2DEG by a spacer layer, the electrons do not scatter off the dopants and at low temperatures, phonon scattering is suppressed, so the mobility of the trapped electrons increases further.

At the Cavendish Laboratory, the 2DEG wafers most commonly used are $GaAs/Al_xGa_{1-x}As$ heterostructures. The wafers are grown using molecular beam epitaxy (MBE), where elements are heated and deposited on a substrate in a high vacuum. Because the deposition rate is slow, and because GaAs and $Al_xGa_{1-x}As$ have similar lattice constants when $x < 0.4$, the sample can change from GaAs to $Al_xGa_{1-x}As$ abruptly. MBE growth also allows the region to be doped to be carefully controlled.

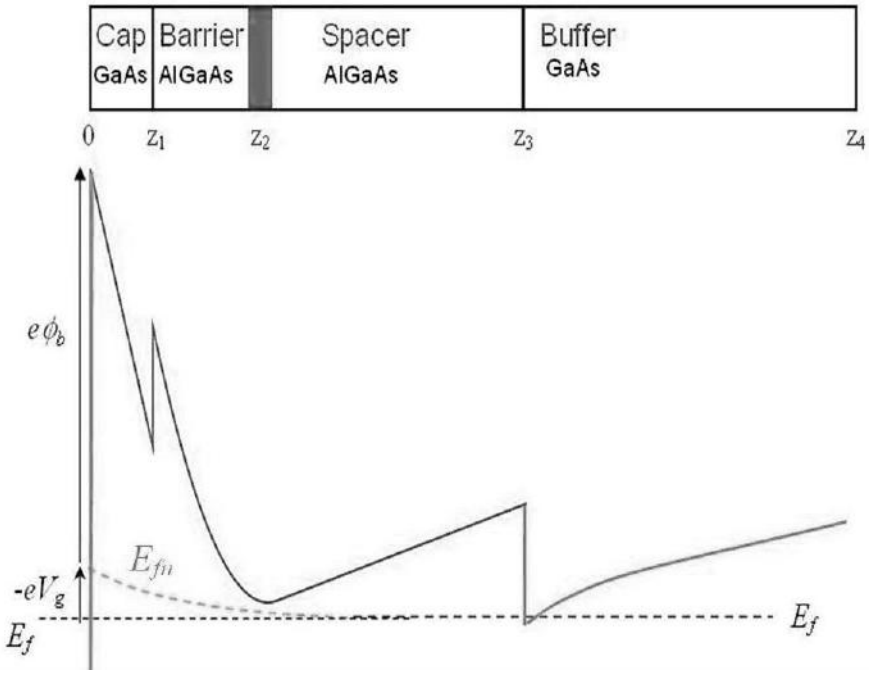

Figure 2.2: Diagram showing the band structure of a modulated doped GaAs/AlGaAs heterostructure. Source: [11]

While electron mobility can be high, it is still a challenge to fabricate high mobility 2DEGs. There are 4 additional types of scattering object that can hinder high mobility: ionised donors, background impurities, interface roughness, and alloy scattering. Despite the inclusion of a spacer layer, the potential fluctuations caused by ionised donors are still the largest contributor to scattering.

2.4.2 Density of states 2D

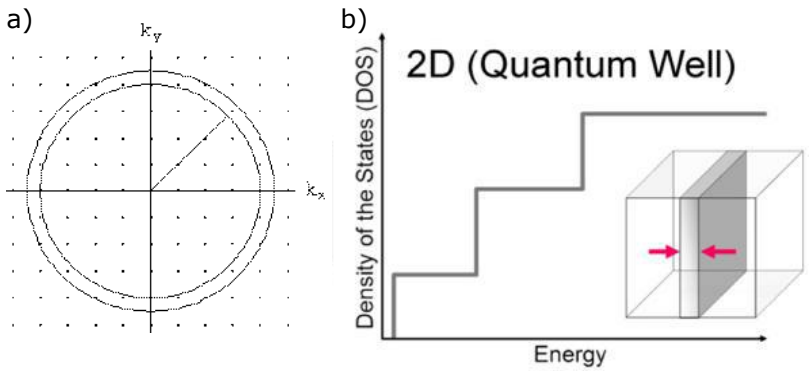

Figure 2.3: (a) The region of available **k**. (b) The 2D DOS [Images taken from [8] and [10]].

When one of the dimensions is smaller than λ, the available energy distribution of the electron changes from the bulk energy distribution. When electrons are restricted in z, the **k** comprises only k_x and k_y, $\mathbf{k}^2 = (k_x^2 + k_y^2)$. Figure 2.3a shows the available k states, which are in the region between **k** and **k** + d**k**; the total area of the region is $v_{2D} = 2\pi|\mathbf{k}|\mathrm{d}\mathbf{k}$. The area of one state is $V_{2D} = (2\pi/L)^2$. The number of states that can fit within this region is given by the total area of the region available divided by the area of one state.

$$g_{2D}(\mathbf{k})\mathrm{d}\mathbf{k} = 2 \times \frac{v_{2D}}{V_{2D}} = \frac{|\mathbf{k}|L^2}{\pi}\mathrm{d}\mathbf{k} \tag{2.6}$$

$g_{2D}(\mathbf{k})\mathrm{d}\mathbf{k}$ contains a factor of 2 to account for spin degeneracy. Substituting equations 2.3 and 2.4 into 2.6 and dividing by the area, L^2, gives the density of states in energy per unit area, (Figure 2.3b).

$$g_{2D}(E)\mathrm{d}E = \frac{m^*}{\pi\hbar^2}\mathrm{d}E. \tag{2.7}$$

2.5 Metal-Semiconductor junctions

A semiconductor that cannot be controlled or measured is of little use. To control the depletion in the 2DEG, metal is deposited which forms a metal-semiconductor (MS) junction with bulk semiconductor, called a Schottky barrier. To measure the conduction of the 2DEG, the deposited metal is annealed to form a MS junction with the quantum well of the 2DEG, forming an Ohmic contact.

2.5.1 Schottky barriers

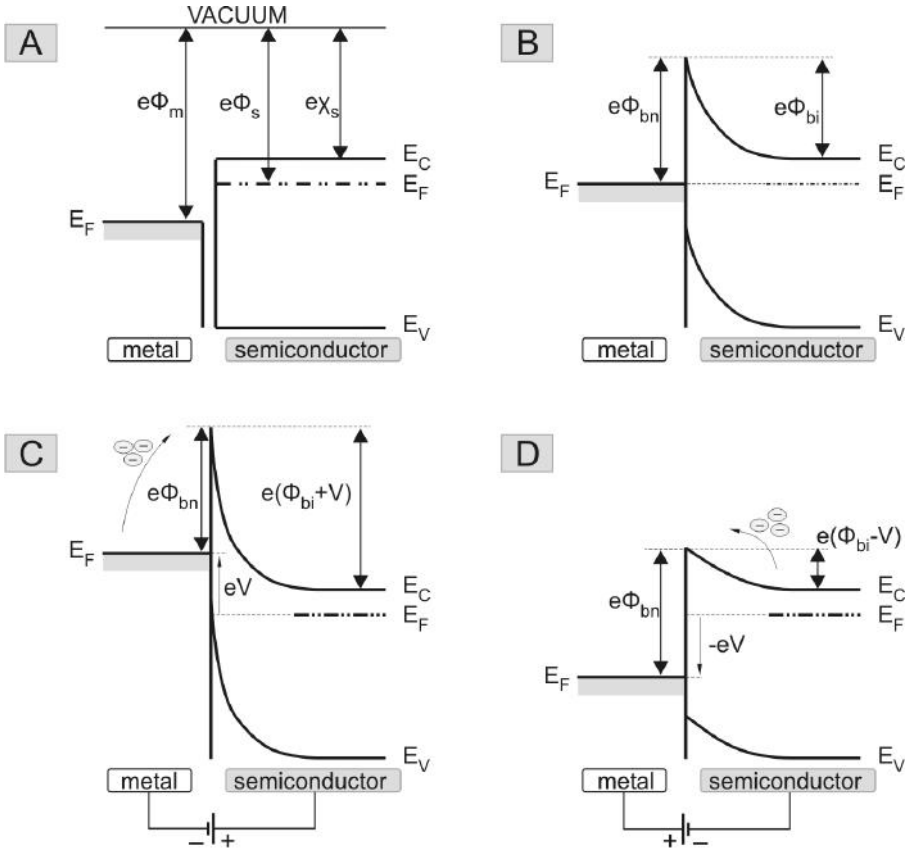

Figure 2.4: Diagram showing the formation of a Schottky barrier with the metal and semiconductor (a) separated, (b) in contact, (c) with a negative voltage bias, and (d) with a positive voltage bias. ϕ and V are voltages E are energies [Image taken from [12]].

Figure 2.4a shows the band structure of a metal and a semiconductor before contact and their respective work functions $e\Phi_m$ and $e\Phi_s$. When the metal and semiconductor are brought into contact, the bands of the semiconductor bend such that the work function of the semiconductor equals the work function of the metal, (Figure 2.4b). On contact, the Fermi levels are equal, and the bending creates a potential barrier at the interface, called a Schottky barrier. To a first approximation, the height of the barrier is given by the Mott-Schottky rule

$$e\Phi_{bn} = e\Phi_m - e\chi_s. \tag{2.8}$$

The potential barrier is a diode; applying a negative potential to the metal lowers the bands with respect to the metal, so no current will flow, (Figure 2.4c). Applying a positive voltage to the gate raises the bands with respect to the metal so current can flow from the semiconductor to the gate, (Figure 2.4d). The Schottky barrier forms the basis for the field effect, where a negative potential applied to a metal gate creates an electric field that depletes the carriers in the 2DEG below it.

While the Schottky-Mott rule gives the right level of surface states associated with defects and dangling bonds, the atomic planes of the surface redistribute charge to shield the semiconductor from the metal. Surface states are filled up by the metal up to the charge neutrality level, and the Fermi level in the semiconductor becomes pinned to this level, called Fermi pinning.

2.5.2 Ohmics

There are a few proposed ways of making Ohmic contacts through band engineering, e.g. by contacting metal to a semiconductor where $e\Phi_m < e\Phi_s$, or by inserting a thin insulating layer between the metal and the semiconductor. In practice, Ohmic contacts to a 2DEG are made by annealing a metal alloy so that it diffuses into the 2DEG. The MS interface is still affected by Fermi pinning.

2.6 Lateral confinement (1D)

2.6.1 Etched and gated 1D wires

The electrons confined in a 2DEG can be further confined to a narrow portion of 2DEG, a 1D wire, or a 0D quantum dot (QD) by means of etching away the 2DEG or depleting carriers using metal gates. Etching away the doped $Al_xGa_{1-x}As$ layer will remove carriers from that region, and can thus be used to constrict a 2DEG. To control the amount of constriction during an experiment, which is usually what is desired, carriers can be removed by placing a metal gate over the regions to be depleted and applying a negative potential to the gate. A Schottky barrier is formed at the interface between the metal and the $GaAs/Al_xGa_{1-x}As$ interface. When a negative potential is applied to the gate, the barrier height increases, and the bands in the $GaAs/Al_xGa_{1-x}As$ bend upwards. This has the effect opposite to that caused by modulation doping, which reduces the carrier concentration in the well.

2.6.2 DOS 1D

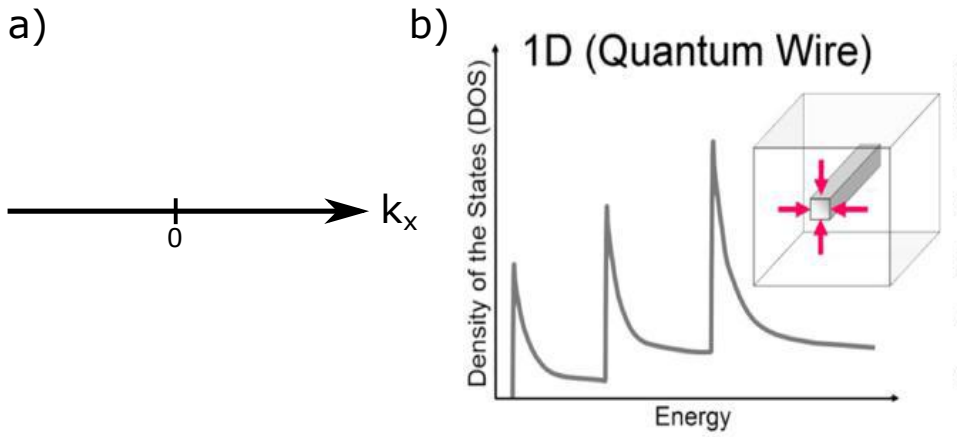

Figure 2.5: (a) The region of available **k**. (b) The 1D DOS [Image taken from [10]].

When the electron is restricted in z and y, **k** comprises only k_x, $\mathbf{k}^2 = k_x^2$. Figure 2.5a shows the available **k** states, which are in the region along length of d**k**; the

total length of the region $v_{1D} = 2\mathrm{d}\mathbf{k}$. The length of one state is $V_{1D} = (2\pi/L)$.

The number of states that can fit within this region is given by the total length of the region available divided by the length of one state.

$$g_{1D}(\mathbf{k})\mathrm{d}\mathbf{k} = 2 \times \frac{v_{1D}}{V_{1D}} = \frac{2L}{\pi}\mathrm{d}\mathbf{k} \tag{2.9}$$

$g_{1D}(\mathbf{k})\mathrm{d}\mathbf{k}$ contains a factor of 2 to account for spin degeneracy. Substituting equation 2.4 into 2.9 and dividing by the length, L, gives the density of states in energy per unit length, (Figure 2.5b).

$$g_{1D}(E)\mathrm{d}E = \frac{1}{\pi}\sqrt{\frac{2m^*}{\hbar^2 E}}\mathrm{d}E. \tag{2.10}$$

2.7 Landau levels

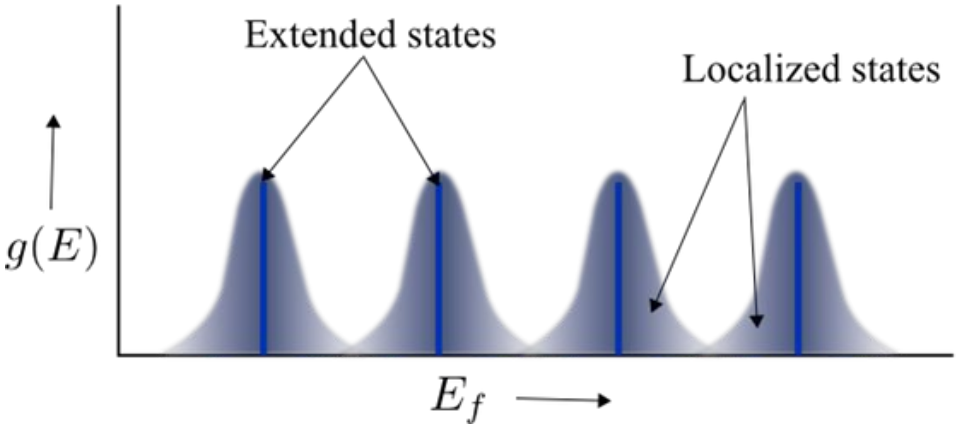

Figure 2.6: Diagram showing Landau levels in the ideal case (above) and with broadening due to impurities (below). Source: [13]

Classically, an electron confined to a plane acted on by a perpendicular magnetic field feels the Lorentz force $F = -e(\mathbf{v} \times \mathbf{B})$, and performs cyclotron motion with angular frequency $\omega_c = \frac{eB}{m^*}$. But, in a 2DEG, we need to treat it quantum mechanically, as electron motion is restricted. For a magnetic field $\mathbf{B} = (\mathbf{0}, \mathbf{0}, \mathbf{B})$ we can use the Landau gauge $\mathbf{A} = (\mathbf{0}, \mathbf{Bx}, \mathbf{0})$. The momentum operator $\mathbf{P}$ now

has added momentum from the magnetic field $e\mathbf{A}$. The Schrodinger equation becomes

$$\frac{(\mathbf{P}+\mathbf{eA})^{\mathbf{2}}}{2m^*}\Psi = E\Psi \tag{2.11}$$

This takes the same form as a one-dimensional harmonic oscillator, so the energy eigenvalues can be given by

$$E_n = \big(n+\frac{1}{2}\big)\hbar\omega_c,\ \ n = 0,1,2,3,.... \tag{2.12}$$

The energy levels become quantised into Landau levels. This does not take into account spin. As electrons can align either parallel or anti-parallel to the magnetic field, the Landau levels undergo Zeeman splitting.

$$E_n = (n+\frac{1}{2})\hbar\omega_c \pm \frac{1}{2}g\mu_B B,\ \ n = 0,1,2,3,... \tag{2.13}$$

where g is the Landé g-factor, μ_B is the Bohr magneton. Ideally the Landau levels should exist at discrete evenly spaced energies. However, the Landau levels experience broadening due to localised states. Electrons can contribute to current only when they have energy in a Landau level extended state.

2.8 Edge states

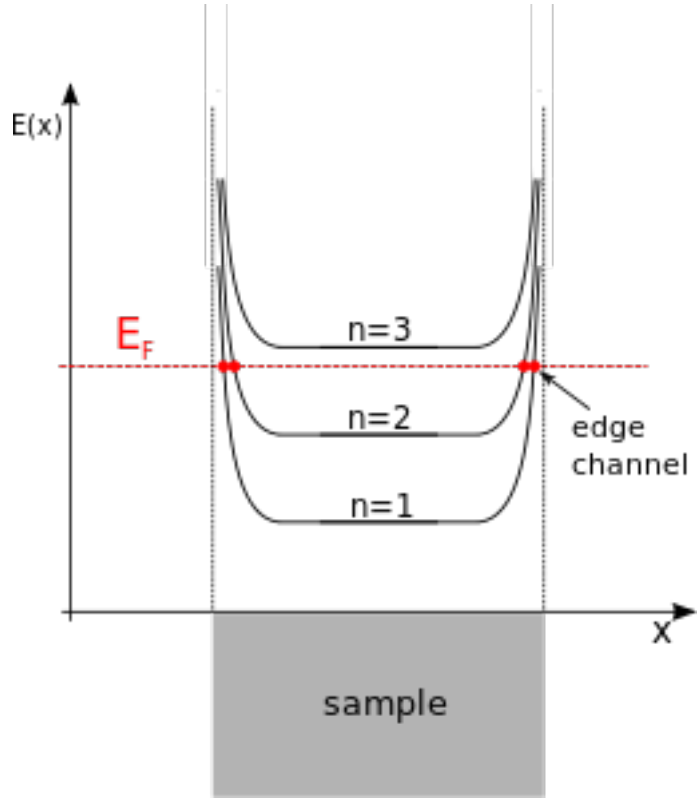

Figure 2.7: Diagram showing bending of the Landau levels near the edges of a sample. Source: [14]

Landau levels are spaced by $\hbar\omega_c$ in the bulk of the 2DEG. But, near the edges, the Hamiltonian has an additional confinement potential that has the effect of bending the Landau levels up, as shown in Figure 2.7. This may seem inconsistent with the degeneracy of the Landau levels in the bulk, but it is consistent because the number of available states changes near the edge: it scales as L^2 in the bulk to L at the edge. The Landau levels bend to meet a boundary condition at the edges of the sample.

2.9 Quantum Dots (0D)

An electron in a quantum dot is restricted in x, y, and z. QDs in semiconductors are made by patterning gates over a 2DEG to restrict electrons in the xy plane by the field effect, or by using a combination of etched wires and gates to define a 0D region.

2.9.1 DOS 0D

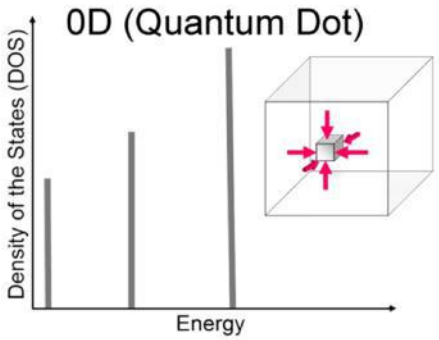

Figure 2.8: The 0D DOS [Image taken from [10]].

As there are no allowed values for $k_{x,y,z}$, the QD is atom-like and DOS for a QD is just a set of discreet energy levels.

2.10 Coulomb blockade

If two conducting regions are brought close together, separated by a small insulator, a small capacitor is formed; and if that capacitor is small enough that electrons can tunnel through the insulator, a small leaky capacitor is formed. If the thermal energy kT is less than the charging energy of the capacitor $E_c = e_c^2/2C$ where C is the capacitance, electrons are prevented from crossing the barrier. The Coulomb blockade is a purely classical charging effect: as electrons are built up to one side of the barrier, an electrostatic potential difference $\Delta\phi = e/C + \Delta\phi_{ext}$ is built up. Adding more electrons causes $\Delta\phi$ to increase linearly until $E_c = e\Delta\phi$,

at which point the electrons have enough energy for an electron to overcome the barrier. When one electron is transferred $\Delta\phi$ jumps from $e/2C$ to $-e/2C$, and electrons are prevented from crossing the barrier until electrons have built up again for $E_c = e\Delta\phi$ [15]. In mesoscopic devices the scale of the capacitor is small enough to allow electrons to tunnel through the barrier. Placing two insulators in close proximity creates an island, which can store charge. When the potential on an island is varied, single electrons can be transferred across it. This forms the basis of the single electron transistor.

2.11 Universal decay cascade (UDC) model

This section describes the model for predicting the amount of pumped current from the work done by Kashcheyevs. His work is first presented in his universal cascade decay paper [16], and since then it has undergone a number of iterations in an attempt to explain some of the new data that was emerging [17–19].

The main premise of the UDC model is that a large number of electrons are collected in a dot, the majority of which back-tunnel into the source lead before the dot is raised enough to be considered decoupled from the source. Kashcheyevs' theoretic work aims at providing a framework for predicting the number of remaining electrons in the dot, based on the ratio of the decay rates of the electrons in the dot. The pumped current $I_P = \langle n \rangle ef$, where $\langle n \rangle$ is the average number of electrons pumped per cycle, e is the electron charge, and f is the pumping frequency. Working in a regime with perfect ejection, $\langle n \rangle$ is given by the probabilities of having n electrons in the dot by the quantum decoupling time, $\langle n \rangle = \sum nP_n(t_d)$.

A quantum dot containing n electrons that is coupled to a lead will have a time evolution of $P_n(t)$ that depends on four processes:

- The rate that an electron enters the dot such that there are n electrons left in the dot.
- The rate that an electron leaves the dot such that there are n electrons left in the dot.

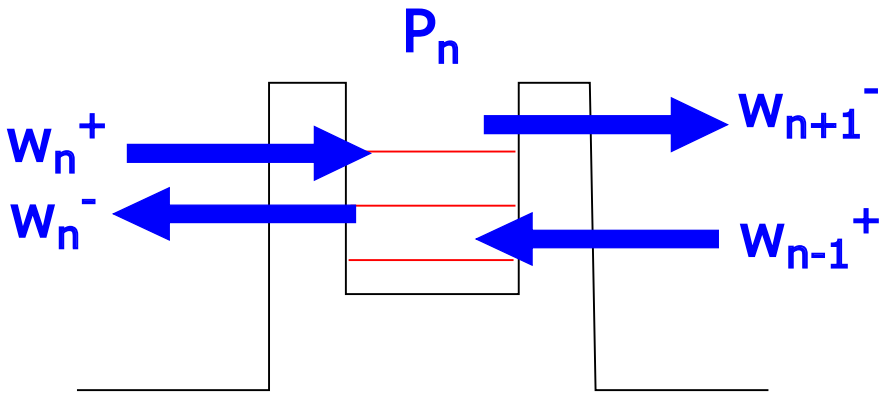

Figure 2.9: A schematic of the tunnelling rates in and out of a dot.

- The rate that an electron enters the dot that has n electrons in it.
- The rate that an electron leaves the dot that has n electrons in it.

These are drawn in Figure 2.9. The sum of these processes makes up the master equation:

$$\frac{dPn(t)}{dt} = -\Gamma_n\Big[(1-f(\mu_n))P_n(t) - f(\mu_n)P_{n-1}(t)\Big] + \Gamma_{n+1}\Big[(1-f(\mu_{n+1}))P_{n+1}(t) - f(\mu_{n+1})P_n\Big] \tag{2.14}$$

where $\Gamma_n = W_n^- + W_{n-1}^+$, the sum of the tunnelling rates in and out of the dot.

Kashcheyevs gives the exact iterative solution to a simplified form of equation 2.14:

$$P_n(t) = \int_{t_0}^{t} e^{-\int_{t'}^{t}\Gamma_n(\tau)d\tau}\Gamma_{n+1}(t')P_{n+1}(t')dt'. \tag{2.15}$$

However, the final fitting equation that is used is a general fitting function for a

double exponential curve.

$$\langle n \rangle = \sum_{n} \exp(-e^{-\alpha(V-V_0)+\delta_n}) \tag{2.16}$$

This model has just two fitting parameters, α and δ_n. If this model is correct, α and δ_n must contain all the information about the physical parameters of the pumping process. α is not explicitly stated in the paper, but we think it is a constant that relates the gate voltage to the height of the confining barrier. Kashcheyevs argues the δ_n contains information about the ratio of the tunnelling probabilities of different electrons in the dot, as well as a Δ_{ptb} term and temperature term.

$$\delta_n = \frac{\Gamma_n}{\Gamma_{n-1}} + \frac{E_C}{\Delta_{\text{ptb}}} \tag{2.17}$$

Here Γ_n is the back-tunnelling rate of the n^{th} electron in the dot, E_C is the charging energy of the dot, and Δ_{ptb} is the shift of the energy levels in the dot relative to the entrance barrier energy in the time it takes for the tunnelling rate to drop to e^{-1} of its original tunnelling rate. While some parameter values such as the dot charging energy have been successfully extracted from this model, the connections to other parameters are not as accessible. The difficulty is carrying the physical description of the dot occupancy probability based on back-tunnelling rates from equation 2.15 through the calculation to equation 2.16. As a result, relating the change in measured data to physical process during the pumping cycle becomes challenging, and there is a lot of ongoing discussion with Kashcheyevs to reconcile interpretations of measured data with his model.

Chapter 3

Development stages of the quantum pump

This chapter chronicles some of the papers that made important advances in single electron transport devices. These papers cover the theoretical and experimental methods that have progressed single electron transport (SET) to its present level with regard to defining a current standard, and so completing the quantum metrological triangle. This chapter is in four parts: the metal-oxide single electron turnstile, semiconductor pumps, pumps driven by surface acoustic waves (SAWs), and the modern Gigahertz pump. A good review of quantum pumps is given by Keastner & Kashcheyevs [20].

3.1 The metal-oxide pump (1983)

The first major paper on the subject of SET was in 1983 by Thouless [21]; he showed theoretically that current could be quantised by a slow periodic variation of potential. He starts with the Schrödinger equation with a potential that is both time and space dependent - a travelling wave - and solves it in these two cases of periodic dependence separately. The separation of time and space dependence is important because a quantum pump requires periodic time dependence to be suitable for reaching the current standard. Additionally, a potential com-

prised of many incommensurate potentials also allows for a quantised current. Incommensurate potentials are looked at in much greater detail by Prange and Grempel [22]. They show that the extent to which eigenstates are localised is dependent on the ratio of the periods.

A single electron transistor was first used to observe SET and the Coulomb blockade; this comprised two tunnel junctions and a gate. In earlier pumps, poor fabrication techniques meant the devices worked poorly, and no single electron effects could be observed. Subsequently, Fulton & Dolan were the first to report the successful observation of single electron effects in the I-V curve [23]. They used a new fabrication technique, angled metal-oxide deposition, to fabricate smaller tunnel junctions, which increased the charging energy E_C, making quantised effects more noticeable. Their setup, shown in Figure 3.1, consisted of an island separated by three tunnel junctions. They passed a current through the two outer junctions and used the middle junction as a voltage probe. However, their device was not a usable pump, as it did not generate current. Although they made 20 such devices in different sizes, with junction areas ranging from $0.001 - 0.03\,\mu\text{m}^2$ and junction resistance R in the range $1 - 100$ kΩ, they presented results for just two of them, one small with small capacitance S, and one large with large capacitance L. As expected on the basis of the Coulomb blockade, at a given temperature, S shows a greater Coulomb step and more single electron effects than L. Figure 3.1 shows the I-V curve of S and L. As electrons are added to one side of the tunnel junction, the voltage V_{off} increases until $eV_{off} = e^2/C$. Since $C \propto A$, where A is the area of the junction, $V_{\text{off}} \propto A^{-1}$.

The Coulomb blockade nature of the pump puts a limit on the resistance. Fulton & Dolan [23] state that as the Coulomb blockade is a classical effect, valid only when the lifetime energy broadening $\hbar/\tau$ is much smaller than the charging energy $e^2/2C$, which places a limit on $\tau >> 2\hbar C/e^2$, where τ is the average time before changing states, the reciprocal of the driving frequency. The current is equal to the charge e divided by the average time before changing states, $I = e/\tau$. By imposing the limit on τ, $I << e^3/2\hbar C$. Coulomb effects are seen when the energy gained by an electron in tunnelling through a barrier eV is of the order of the charging energy $e^2/2C$, or V is of the order of $e/2C$. Ohm's law gives a lower limit for the junction resistance, $R > \hbar/e^2$.

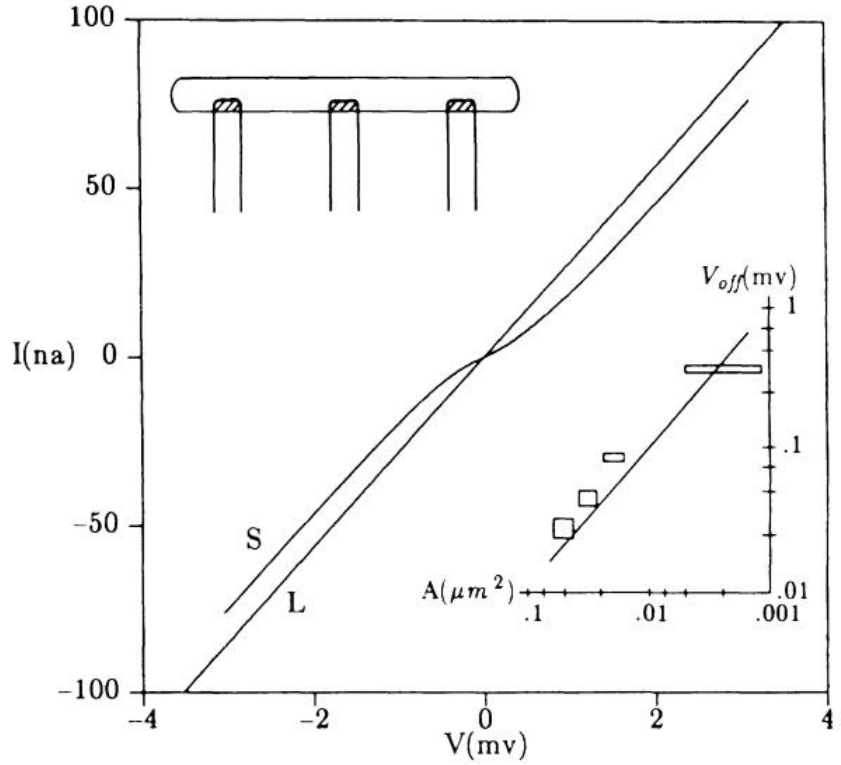

Figure 3.1: I-V curves for junctions with small capacitance S and large capacitance L. Upper Left Inset: A schematic diagram or their device. It comprises three metal channels connected to a metal island via metal-oxide tunnel junctions (dark areas). Bottom right inset: Offset voltage across the tunnel junction vs. junction-area, $V_{\text{off}} \propto A^{-1}$. Source: (Fulton & Dolan, 1987) [23]

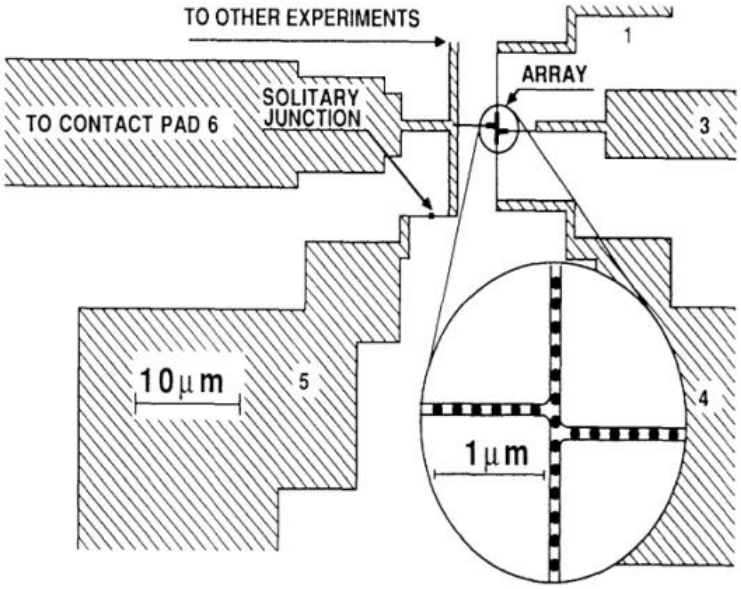

Figure 3.2: Diagram of a solitary junction and a 25 junction array. The shaded areas are the Ohmic contacts. Source: (Delsing et al., 1989) [24]

Neither the electron transistor nor the electron trap can accurately pump electrons: the electron transistor has an associated stray capacitance from it being directly connected to the source and drain, and the electron trap has no means of applying a gate voltage.

Delsing et al. [24] were the first to test a single electron turnstile, which combines the electron transistor and trap. Using the same fabrication technique as Fulton & Dolan, they made similar metal-oxide junctions and investigated the differences in current suppression between a solitary junction and a junction in the centre of an array. They arranged 25 junctions in a cross to form two 13-junction 1D arrays as shown in Figure 3.2. The I-V characteristics of the solitary junction were determined using a 2-point measurement, so it includes the resistances of the contacts. The I-V characteristics of the central junction were determined by passing a current through two of the leads and measuring the voltage across the other two leads. This is a 4-point measurement, which has an advantage over a 2-point measurement in that it excludes the stray resistance due to the Ohmic contacts. Additionally, the pairs of contacts can be swapped to verify that there is no interference from the contacts; variations in resistance did not exceed 20%.

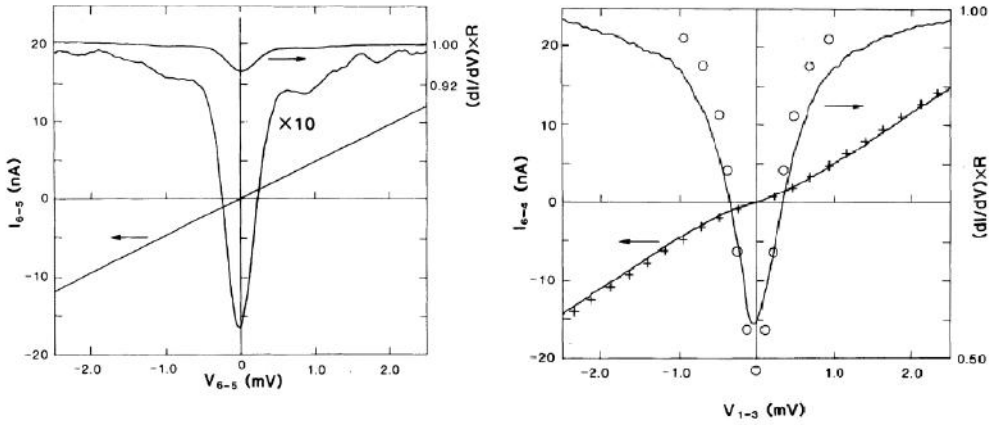

Figure 3.3: I-V curves for the solitary junction (left) and the junction array (right). Source: (Delsing et al., 1989) [24].

Figure 3.3 (right) shows the I-V curve of the middle junction. A Coulomb plateau can be seen, but the derivative curve shows the quantisation much more clearly. The derivative curve, based on experimental data (graphed in solid lines) agrees well with theory (graphed as circles and crosses). However, the results for a solitary junction were not similar to those for the junction array. Figure 3.3 (left) shows the I-V curve of the solitary junction - a Coulomb plateau cannot easily be seen other than in the derivative curve. This reflects resistance being more suppressed in the solitary junction than in the array. From orthodox theory, the requirement for observing Coulomb effects is that the junction resistance is greater than the quantum resistance, $R > \hbar/e^2$. In their commentary, Delsing et al. suggest that stray capacitance causes a problem in single current junctions that is eliminated in the arrays.

In a second 1989, paper Delsing et al. observed the first reliable time correlation between current and an applied DC voltage with a radio frequency (RF) signal [25]. As such correlation was not observable due to the stray capacitance between the junction leads, they isolated stray capacitance from the middle section by using a 1D array. When they tackled this in their earlier paper, they were unable to reliably observe time correlation because the temperature was too high. For their second 1989 paper they used a newly developed dilution refrigerator, and were able to do the experiment at 50 mK. As in the earlier experiment, they applied a current and measured the voltage, except this time they investigated time correlation by also applying a microwave RF signal. Figure 3.4 shows the

peaks in dynamic resistance $R = dV/dI$ as a function of frequency. Increasing the temperature broadens these peaks. The dilution refrigerator allows the peaks to be distinguished. Interestingly, they found that the currents at which the voltages peaked were multiples of the applied microwave frequency $I = nef$.

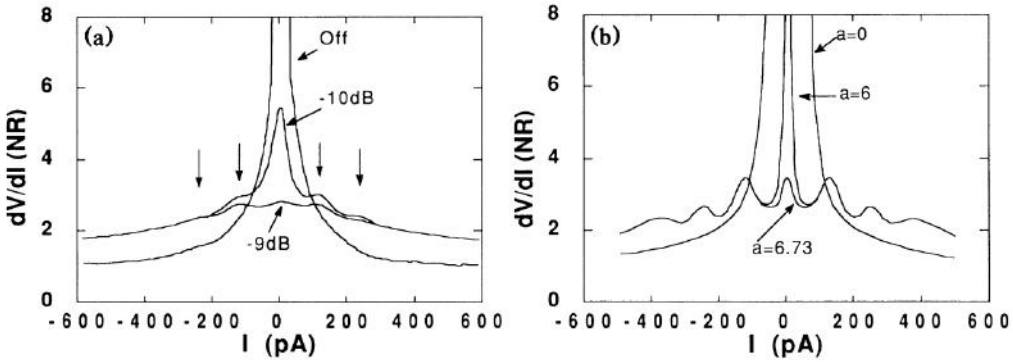

Figure 3.4: Dynamic resistance as a function of I for the array (left) and a numerical simulation (right). The curves correspond to different values of microwave power. Source: (Delsing et al., 1989). [25]

Geerlings et al. expanded on work done by Delsing et al. Whereas Delsing et al. observed a quantised current clearly only in the derivative I-V curve, Geerlings et al. were the first to observe a quantised current in the I-V curve, which required a much improved accuracy [26]. Accuracy is determined by the width and flatness of the Coulomb plateau. None of the terms that make up the current $I = nef$ depend on V, so ideally, I should be flat, (with the exception of n which jumps discretely at certain voltages, resulting in other plateaus). Deviation from this lowers accuracy. The shorter the plateau, the less statistically significant the data becomes. Geerlings et al. found that the widths of the plateaus were dependent on the amplitude of the applied AC voltages. Figure 3.5 shows the change in I-V curve when AC voltages of different frequencies were applied. The dotted curve shows the characteristics with no AC voltage. The large zero current plateau is expected because of the Coulomb blockade. When an AC voltage of the order of E_C is applied, multiple electron transport is possible; this is shown in the inset of Figure 3.5, where the oscillations overlap.

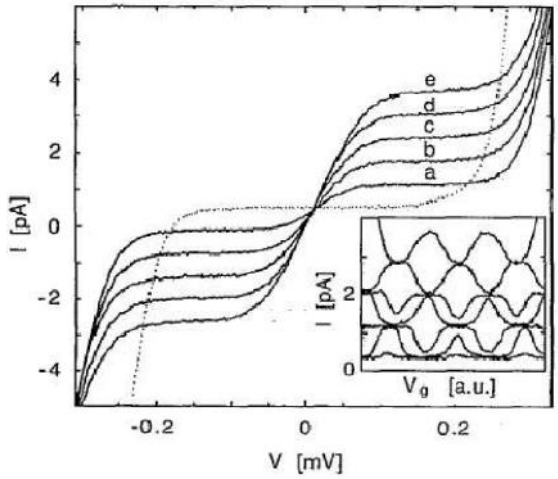

Figure 3.5: I as a function of V for the different frequencies. Source: (Geerlings et al., 1990) [26]

Geerlings et al. used rate equations to place upper and lower limits on the applied frequency. The rate equation for electron transport is given by $\Gamma = \frac{1}{RC}(\frac{\Delta E}{2E_C})\frac{1}{e^{\Delta E/kT}-1}$. For a tunnel with $\Delta E = -0.1e^2/C$, this gives a tunnelling rate of $\Gamma = (10RC)^{-1}$. For the device used, $C \approx 2$fF, so $(10RC)^{-1} \approx 5$GHz, or $\Gamma \approx 100$MHz. An equivalent but different definition of accuracy is given by the lower of two probabilities: that an electron misses a cycle and that an electron leaks due to thermal excitation. If the barriers are raised and lowered too fast, i.e. the frequency is too high, the electron may not have time to tunnel though. The probability of missing a cycle is given by $e^{-\Gamma/f} = e^{-500\text{MHz}/f}$. If the temperature is too high, electrons have a higher probability of being thermally excited over the barrier. From the rate equation, the leakage current $\Gamma_{Leak} = \Gamma\frac{1}{e^{\Delta E/kT}} \approx \Gamma e^{-\Delta E/kT}$ for $\Delta E >> kT$. At the frequency required for a current standard, the probability of missing a cycle is $e^{-0.5} \approx 0.6$.

3.2 Semiconductor pumps (1991)

Using a similar model to Geerlings et al., but with a different etching process, Kouwenhoven et al. observed a quantised current in a quantum dot (QD) device [27]. The capacitance of the dot is given as $C = 0.24$ fF, which is an order of

magnitude smaller than the capacitance of the metal-oxide dot. As the energy difference between states ≈ 0.03 meV is much smaller than the charging energy $E_C = e^2/2C \approx 1$ meV, the continuous equation for the tunnelling rate is used.

Using the same treatment for accuracy used by Geerlings et al. but with the semiconductor characteristics, the accuracy in Kouwenhoven et al. can be compared. As noted in 3.1 accuracy is given by the lower of the two probabilities: that an electron misses a cycle and that an electron miss-tunnels, or leaks, due to thermal excitation. The tunnelling rate $\Gamma = (10RC)^{-1} = 10^3$ MHz. At a frequency of 10 MHz, the probability of a missed cycle is $e^{-1/fRC} = e^{-1000}$, compared with e^{-50} for the metal-oxide junction at the same frequency. In respect of miss-tunnelling, $\Gamma_{\text{Leak}} = 0.1$ MHz, corresponding to a miss-tunnelling probability of roughly 10^{-2}. Its errors are an order of magnitude smaller than 0.6 for the metal-oxide pump.

As noted in 1.2, quantum pumping for a current standard requires accuracy of 10^{-8} and a current $I > 1$nA, corresponding to a frequency of roughly 1 GHz. At this frequency, the probability of missing a cycle is $e^{-10} \approx 10^{-5}$ for the semiconductor pump compared with $e^{-0.5} \approx 0.6$ for the metal-oxide pump. Although this is at least four orders of magnitude smaller than for the metal-oxide barrier, it is still too high for use as a current standard.

3.3 Semiconductor arrays

Several small improvements have been made on the work of Geerlings et al., the most well known, and one of the most important, was the 7 junction array by Keller et al. Placing 7 tunnel junctions in series, Keller et al. achieved an accuracy of 1.5×10^{-7}, relatively close to the accuracy required for a current standard [28]. Currently it is the only device that has achieved this accuracy.

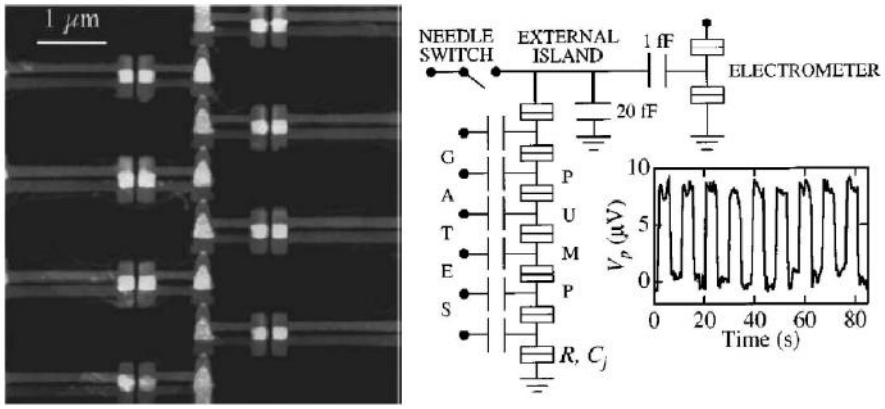

Figure 3.6: Left: Scanning force microscope image of the array. The tunnel junctions are the little bright spots at the tips of the triangles. Right: A schematic of the setup used and a calibration graph for electrons being added and removed every 4.5s. Source: (Keller et al., 1996) [28]

The device of Keller et al. is shown in Figure 3.6. The junctions are the bright spots where the islands overlap. Keller et al. reduced the overall capacitance by using angled metal-oxide evaporation to make the junctions small, and used a quartz substrate, which has a small dielectric and thus reduces stray capacitance. Pumps like that of Keller et al., which manipulate electrons using the Coulomb blockade, are not completely coherent: when a voltage is applied to a gate, it polarises not just the nearest island, but to some extent the neighbouring islands as well. To correct for this, they applied small voltages with opposite polarity to the neighbouring islands. In practice, tuning a correction voltage to exactly offset the polarisation due to the original is very difficult, and errors due to it probably remain. They used a seemingly unique method to determine accuracy: instead of looking at the characteristics of an I-V curve, they looked at the variation in the charge of an island over time. Electrons were pumped onto the island, then back off the island, at a frequency $f = 5.05$ MHz. The time the electrometer took to measure the voltage of the island was much longer than the time the pump took to add and remove the electrons. The electrometer effectively saw a static charge. However, if there was an error in one of the pump cycles, with either co-tunnelling or a missed tunnel event occurring, the charge on the island would be changed by $\pm e$, which would be picked up by the electrometer. This assumes that errors are rare enough that at most one error will occur per electron measuring time; if there were many errors they might cancel each other out and not be registered.

Despite these caveats, Keller et al. were quite successful in increasing accuracy and did produce a current large enough for a capacitance standard [29]. However currents were of the order of picoamperes, 3 orders of magnitude smaller than is required.

3.4 Surface Acoustic waves (1996)

Up to 1996, current could be measured to an accuracy of $\approx 10^{-2}$. The factors limiting accuracy of measurement were the stray capacitances of the Ohmic contacts used to measure current and the need to apply a bias voltage. To improve current and accuracy, a new driving mechanism was developed that did not rely on the Coulomb blockade. Surface acoustic waves (SAWs) could pass through a 2DEG gas and transfer some of their momentum to the electrons, creating a small current, called an acoustoelectric current. Observed by Shilton et al. in 1996 [30–32], the current did not exhibit quantisation or a Coulomb step, but peaked periodically with gate voltage shown in Figure 3.7. The reason for not observing the steps is the non-linearity of the I-V curve. Only electrons close to the Fermi energy can contribute to the current. Of these, only the electrons in the upper sub-band of the quantum point contact (QPC) have Fermi velocities V_f close enough to the SAW velocity S to contribute to the current.

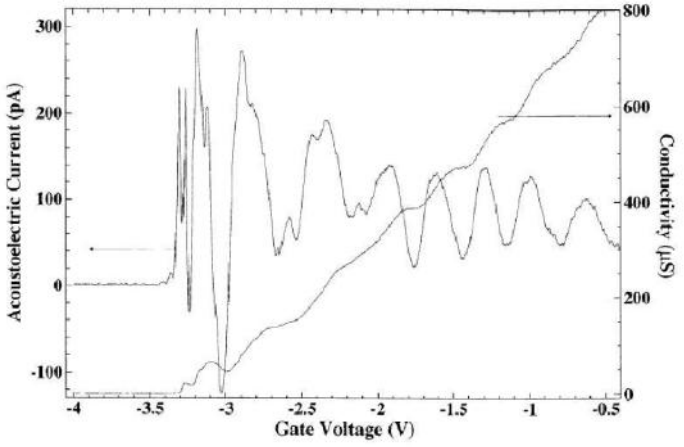

Figure 3.7: I-V curve showing an oscillating current, rather than the usual Coulomb plateau. Source: (Shilton, et al., 1996) [30]

To ensure that a current could be measured, the QPC had to be quite long $L \approx 500$ nm; at such lengths, parts can be sufficiently detached from the bulk of the 2DEG to avoid screening of the SAW. Unfortunately, a long QPC contains more impurities, which distort the current at low gate voltages. This was observed by Shilton, et al. and can be seen around the threshold voltage in Figure 3.7. The current around the threshold voltage is very difficult to describe. It varied between devices, and even varied at different times in the same device. Because of the volatility near the threshold, Shilton et al. discuss only the more regular oscillations for $V > -2.5$ V. The regularity in the oscillations reflects the more effective screening of impurity potential. Unfortunately they can only be driven at one frequency, which is determined by the spacing of the interdigitated transducers, and are negatively affected by heat [33, 34].

3.5 Gigahertz charge pumping (2003-present)

While theoretical applications for SAWs were making headway, a group in Tokyo University and, independently, a group in the Cavendish Laboratory, developed a method of pumping that was a throwback to the old turnstile pump of the early 90s, but allowed high frequency pumping. While others have made contributions to the gigahertz pump, notably the National Institute of Standards and Technology, NPL, and Delft University, this section will focus on the advances in Cambridge and Tokyo.

3.5.1 Gigahertz pumps

Current quantisation was first achieved by Fujiwara et al. in 2004 [35]. Their setup, shown in Figure 3.8 (left), consisted of two poly-Si metal-oxide-semiconductor (MOS) finger gates fabricated across a 30 nm wide Si wire that has been etched into a Si MOS. Although it has three gates, only two are used: the third gate is a backup. A wide upper gate determines the base potential for the system and hence the number of electrons that sit in the well. Due to the already very advanced Si etching and lithography techniques, the device could be made very small, and hence have small capacitance and large charging energy compared

with other non-Si semiconductor devices. This means Si devices can be operated at a higher temperature than other semiconductor devices. All Fujiwara's experiments were done at $T = 20$ K. Figure 3.8 (right) shows the mechanics of the system. As pulses of voltage are applied to the two gates out of phase, the potential at the gates rises and falls periodically allowing a certain number of electrons through, depending on the upper gate voltage.

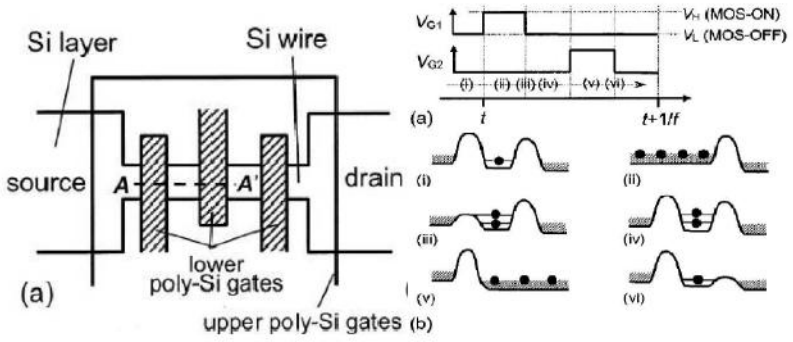

Figure 3.8: Left: Schematic of the Fujiwara pump. Right: The transfer sequence. (a) Gates G1 and G2 are pulsed out of phase. (b) Schematic of how the electrons are picked up and deposited over time. Source: (Fujiwara, et al., 2004) [35]

The relationship between gate voltage and current plateaus in the I-V curve is shown in Figure 3.9. The plateaus were observed at frequencies up to 100MHz, with a base plateau accuracy of 10^{-2}. Beyond this frequency, pulse distortion and cross-talk could have an adverse effect on the results. As stated by Fujiwara et al. the source and drain are disconnected from the gates; so the bias voltage has little effect on the potential and hence does not contribute to the capacitance. This is markedly different from the single electron turnstile pumps, where the stray capacitance due to the source and drain was a big factor in limiting the frequency at which electrons could be pumped.

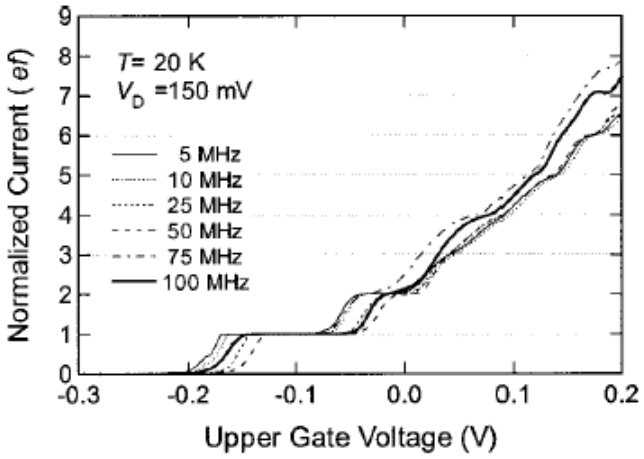

Figure 3.9: Normalised I-V curve showing the frequency dependence of the Coulomb plateau. Source: (Fujiwara, et al., 2004) [35]

In 2007 Blumenthal et al. greatly improved the frequency at which electrons could be pumped by introducing oscillating potentials [36]. Rather than using timed pulses, they proposed that three potential barriers be raised and lowered in such a way as to achieve SET. The three barriers were labelled left, middle, and right, as shown in Figure 3.10. The middle junction does away with the need for a wide upper gate voltage, and can be modulated by the same parameters as the other two finger gates. The left and middle barriers oscillated in phase while the right barrier oscillated out of phase. To ensure that electrons were pumped in the correct direction, even when no bias voltage is present, the left and middle barriers oscillated with much greater amplitude than the right barrier.

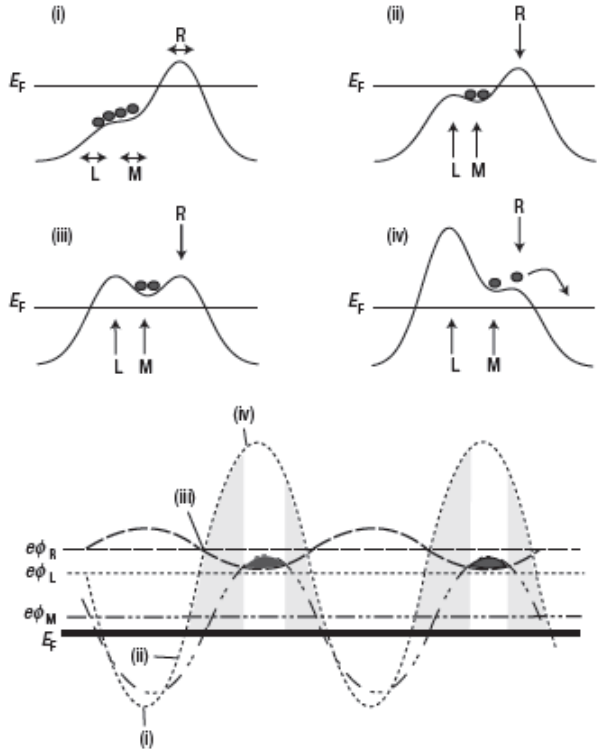

Figure 3.10: Top: Schematic of how the gates will transport an electron. Bottom: The relative amplitudes and phases of the three gates as a function of time. Respectively, the lightly shaded and dark areas correspond to when the electron is trapped and deposited. Source: (Blumenthal et al., 2007) [36]

From section 3.1, the limit on RC for turnstile pumps puts a limit on the driving frequency $f < 20$MHz. The gigahertz pump allowed a driving frequency of 3.5GHz and showed quantised steps at $1,072$ MHz. It can achieve these high frequencies because the electrons are not being driven against a Coulomb blockade. The tunnel resistance R varies with applied voltage, similar to a SAW, and goes below the quantum resistance $R_Q = h/e^2$ when the electrons leave the well. Also the high frequencies involved make the process non-adiabatic. So for many reasons orthodox theory no longer holds. Errors due to the non-adiabatic nature of the pumping were treated in SAW devices as corrections to the Hamiltonian by Flensberg et al. [37]. They state that the corrections depend only on a single parameter τ_0, the time it takes for a barrier to go from transparent (at the Fermi level) to opaque (virtually zero probability of tunnelling). Accuracy is determined by the slope and length of the plateau. Without taking into account

length, which depends on experimental factors, the expression for the slope S can be given theoretically: $S \approx 2\frac{E_c}{kT_{eff}}e^{-E_c/kT_{eff}}$. Here T_{eff} is the effective temperature the electron experiences taking into account the non-adiabatic nature of the oscillations. $T_{eff} = \sqrt{T^2 + (0.88h/k\tau_0)^2}$. Note that in an adiabatic system, the electron sees a static barrier, $\tau_0 \to \infty$, so $T_{eff} = T$. To reduce S and prevent thermal fluctuations, the condition $kT_{eff} << E_C$ must hold.

The device used by Blumenthal et al. had a charging energy $E_C = e^2/2C \approx 1$ meV, which places an upper limit on $T_{eff} << 11.6$ K. Most experiments were done at 1.8 K, so were within this limit. To try to achieve the greatest accuracy, some experiments were done at 300 mK. At a driving frequency $f = 1$ GHz, τ_0 was estimated to be 0.1 ns. Placing all this in the equation for the slope gives $S \approx 10^{-8}$. This error is small enough to be used as a quantum standard, but it was noted that the exponential dependence on τ_0 means that future work will have to be done to ensure that τ_0 can be reliably calculated. It was noted that the limitations found in SAWs described by Ebbeck et al. are not present in gigahertz pumps [33]. Most notably, frequency can now be varied, and there are no issues involving heat being generated.

3.5.2 Single oscillating barrier

In Tokyo in 2008, Fujiwara et al. greatly simplified their earlier pump (from 2003) in a way that allowed them to achieve pumping up to 2.3 GHz and a current of at least a nanoampere with an accuracy of 10^{-2} [38] and later by Kaestner et al. [39, 40]. Instead of two oscillating barriers, or three as Blumenthal et al. had, they had only one barrier that oscillated, which in each cycle pushed an electron over a constant potential barrier as shown in Figure 3.11. Here the first barrier oscillates while the second barrier remains fixed. It is advantageous to have fewer oscillating barriers because there are fewer elements that can contribute to an error. This method has been adopted by nearly all recent groups using gigahertz pumps.

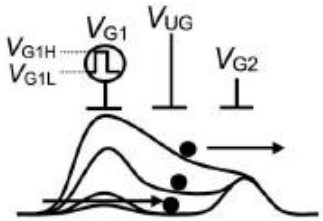

Figure 3.11: Operation of a ratchet pump. The pump is able to pump because of the asymmetry of G1 provided by the upper gate. Source: (Fujiwara et al., 2008) [38]

Wright et al. extended this to look at improving accuracy using pumps in parallel [41] and found that operating pumps in parallel increased current without heavily affecting accuracy.

3.5.3 Applied magnetic fields

Accuracy can be increased by applying a magnetic field [42]. Since work was done on the first quantum pumps, there have been very few major papers that detail the effects of quantum pumping in a magnetic field. The only pre-Blumenthal et al. pump paper that discussed magnetic fields was Cunningham et al. [43], who showed that magnetic fields destroyed current in SAWs. Recently, work has been done by Wright et al. [42] and Kaestner et al. [44]. In an attempt to entangle electrons, they used a magnetic field applied through an Aharonov-Bohm ring The entanglement was unsuccessful, but quantisation was enhanced. This led to further experiments that focused on how a gigahertz pump current varies with an applied magnetic field.

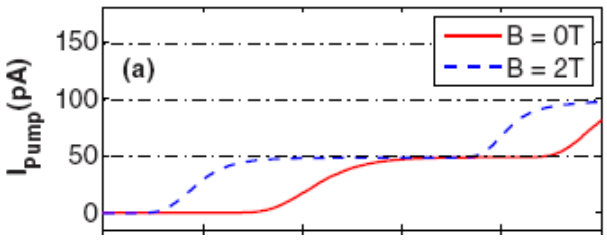

Figure 3.12: I-V curve with and without an applied magnetic field $B = 2$T. Source: (Wright et al., 2008) [42]

Figure 3.12 shows the current plateau with and without an applied magnetic field of $B = 2$ T. Initially these slopes look similar, but taking the 2^{nd} derivative with respect to voltage, the slopes of the plateaus were measured as 21.1pA/V for $B = 0$T, and 9.5pA/V for $B = 2$ T. Using the relation between slope of the plateau and accuracy of quantisation by Janssen & Hartland [45], Wright et al. calculated an improvement in accuracy of 55%. The same experiment was done in a much more rigorous manner by Kaestner et al., who achieved a more significant improvement by using a larger magnetic field $B = 10.2$ T. This improvement was thought to relate to the probability of back tunnelling. As a magnetic field is increased, the electron wave function gets narrower, making it more confined, so reducing the probability of back tunnelling.

3.6 Pump energy experiment

Fletcher et al. at NPL to studied the energy of electrons leaving a gigahertz pump [46]. To measure the energy, they designed a device based on a paper by Taubert et al. where a beam hot electrons from a split-gate hit a barrier; the energies of the electrons could be deduced by measuring at what barrier heights electrons made it over the barrier [47]. Figure 3.13 shows a schematic of the device used by Fletcher et al.; it is similar in operation to the Taubert et al. device but with a pump in place of a split-gate. The measurement of electrons leaving the barrier was calibrated the same way it was done by Taubert et al. but using only the exit gate of the pump. The current reflected by the barrier and through the barrier was measured when the pump was operated normally. Because of RF cross-talk between the gates and the barrier, an attenuator and phase delay were added to cancel it out. Electrons were measured to leave the pump at 150 meV, could be used as a single phonon source, and by changing the phase delay, different electrons could be selected to pass through the barrier [46]. This paper was followed up by Joanna Waldie at the Cavendish, who investigated using an arbitrary waveform generator (AWG) [48].

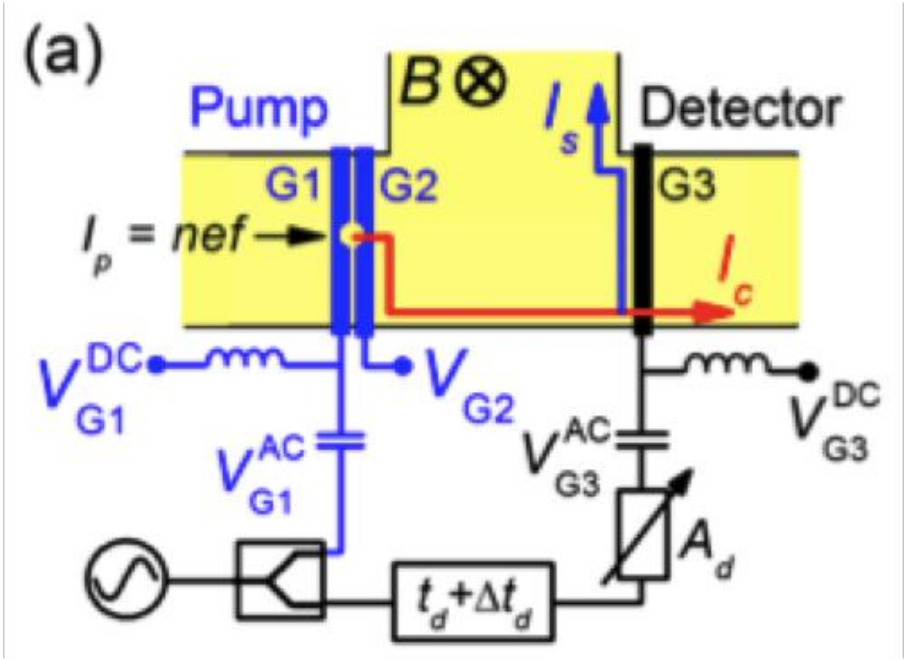

Figure 3.13: A schematic of the device for the pump energy experiment, with the entrance RF gate and exit gate (blue), and the barrier (black). Source: [46]

3.7 Summary

This chapter has chronicled some of the most important papers on quantum pumps. It describes the Coulomb blockade, which was first observed via a small single electron transistor. The experimental observations confirmed the orthodox theory of quantum pumps. Once the first quantised current was observed, the effects of temperature and stray capacitance on the charging energy, and hence quantisation, could be tested. Further studies showed that errors in quantum tunnelling impact heavily on accuracy, which can be determined by the slope and width of the Coulomb plateau.

The chapter then compares semiconductor turnstiles and metal-oxide turnstiles, and shows the former are better suited for attempting to reach a current standard, being smaller, so having a larger charging energy, their quantisation is more pronounced. Despite the marked improvement in the metal-oxide pump, it was far off from reaching the current standard. Because they are scalable, arrays were developed to address this. Keller et al. developed an array that could be

considered to have reached the minimum accuracy required for a current standard. Unfortunately, the current produced was very low compared to the minimum current required.

Looking for alternative pumping methods that avoided the limitations of turnstile pumps, surface acoustic waves (SAWs) were exploited and used as quantum pumps. In some respects, SAWs are advantageous compared to turnstile pumps: they do not rely on the Coulomb blockade, so they can achieve higher driving frequencies, and do not have an associated capacitance, so they avoid the problem of stray capacitance. However, the physical process by which SAWs are produced – applying a voltage to interdigitated transducers on a piezoelectric substrate – means that the device is frequency locked. There are also additional problems associated with heating.

The gigahertz pump, developed independently in Tokyo and in Cambridge, incorporated the benefits of both the turnstile pump and SAW, and led to many experiments that accelerated the movement towards meeting the current standard. The gigahertz pump has many advantages: it can vary frequency and has no heating issues. Recently, the developers of the original pump in Tokyo greatly simplified it and, using a single oscillating barrier, they achieved a current of at least a nanoampere, with an accuracy of 10^{-2}. The next advance, in Cambridge, was the introduction of parallel pumps, which increased current without heavily affecting accuracy, and the application of magnetic fields, which addressed the problem of back tunnelling. The development of the gigahertz pump, both in Tokyo and Cambridge, are part of the steady development towards both the advancement of quantum pumps to SET and the realisation of the metrological triangle.

Chapter 4

Processing

4.1 Introduction

This chapter describes the processing steps used to fabricate the devices presented in this thesis. The devices were fabricated in the clean room at the Cavendish Laboratory in Cambridge University. Initially, quantum pump devices, like the completed device in section 1.3, had a very low yield, which we attribute to various failure modes during processing. To further add to this, completed devices were extremely electrostatically sensitive (ESD), which introduced additional failure modes during measuring. As a result of these factors, few devices initially worked and fewer remained working long enough to usefully measure.

A large part of this thesis was spent identifying the various failure modes and providing solutions to them. The low yield can be explained almost exclusively by problems with the fabrication techniques, which are detailed in this chapter. The failure of completed devices can be explained by poor handling and issues with the measurement setup, the details and solutions of which are presented in section 5.6.

The standard processing steps for these devices that were inherited from previous work in this field are detailed in the thesis by Dr. Samuel Wright [49]. We have identified certain key failure modes and provide solutions in the processing steps. The main processing steps that have been updated are the use of surfactant and

the type of etchant used for the shallow etch, the thickness of deposited gate metal, and the use of an oxide layer to protect a finished device.

At the start of the chapter we describe the types of devices we fabricated. Then, we identify the failure modes and the processing steps responsible for the failures. We detail the updated processing steps for fabricating quantum pumps, a condensed form of which is presented in Appendix A. Explicit reference to the updates we propose as a result of the work done is described in the subsections titled 'Failure mode considerations'. Finally, we introduce new protective steps to prevent completed devices from failing.

4.2 Devices

The most recent style of pump is NPL's gate-defined pump. Defining the dot with the gates was initially done to improve yield, because of problems with non-conducting channels, but it had the further advantage of being able to tune the dot shape and size by changing the gate geometry. Figure 4.1 shows an SEM image of one of these pumps.

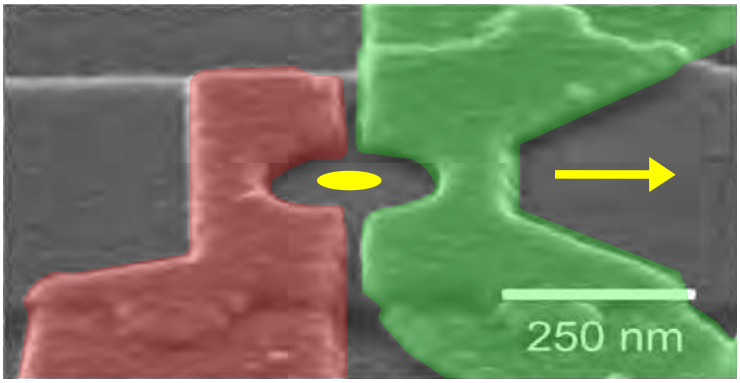

Figure 4.1: A schematic of the device for the pump energy experiment, with the entrance RF gate (red), exit gate (green), and the quantum dot and the direction of pumping (yellow). Source: [50]

In this thesis we experiment with using a split-gate as the exit gate, Figure 4.2. The proposed advantages are that the dot is defined by lateral depletion of the gates rather than depletion under the gates. By placing the gates further away

from the dot, the dot shape is less sensitive to changes in gate voltages. This is clear from a normal split-gate pinch-off where the pinch-off curve is steeper for gate voltages less negative than the definition gate voltage. The device in Figure 4.2 has a split-gate pump to the right of the middle gate and a normal NPL-style pump to the left of the middle gate. Initial comparisons between the 2-gate pump on the left to the split-gate pump on the right at 4.2 K suggest that the split-gate pump produced better plateaus than the 2-gate pump, but as the 2-gate pump is very sensitive to the pump geometry, it is possible that we were comparing a split-gate pump to a very non-optimised 2-gate pump. For example, the optimised 2-gate pump from NPL, which we used for part of the experiment in chapter 7, performed much better than the non-optimised 2-gate pump we fabricated. We will do further testing at lower temperatures to identify if the proposed advantages are realised. This design of pump is also used in a new experiment where we use the two leftmost gates as a pump and pump into the split-gate; this is discussed in the additional future work in chapter 9.

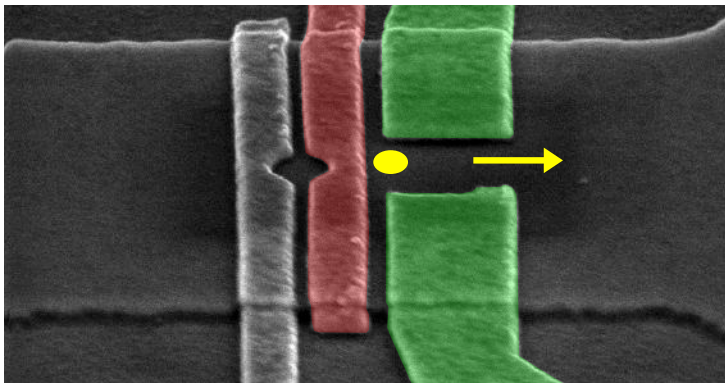

Figure 4.2: A false-colour SEM image of a quantum pump device in a split-gate configuration with the entrance RF gate (red), exit gates (green), and the quantum dot and the direction of pumping (yellow)

Because of the low yield with devices that have a narrow-etched channel, we made devices without a narrow etched channel. Figure 4.3 shows a device that does not have a narrow etch. While the devices conducted, they lead to large spurious currents, which we detail in chapter 6.

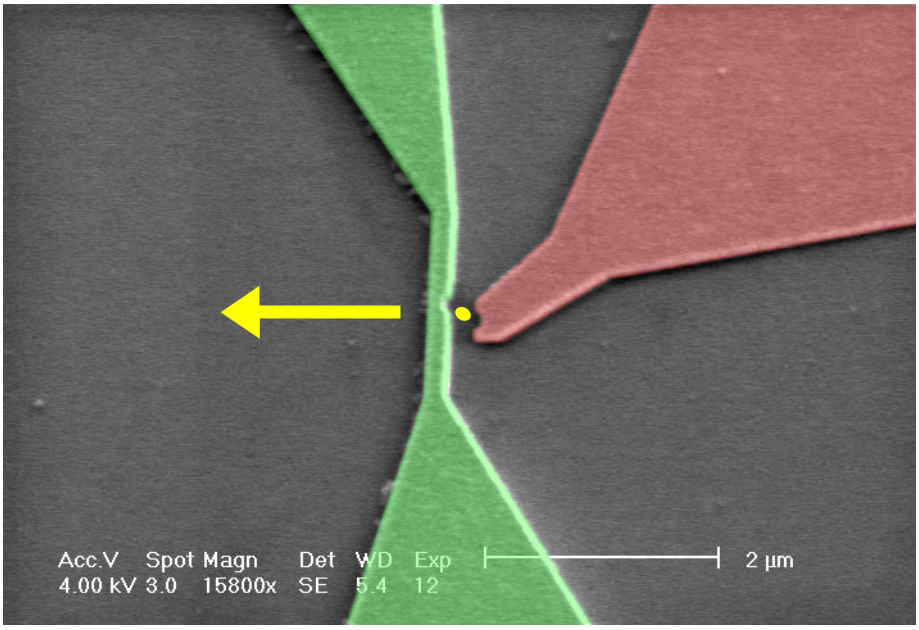

Figure 4.3: A false-colour SEM image of the quantum pump device with no narrow etch, with the entrance RF gate (red), exit gate (green), the dot (yellow), and the direction of pumping.

Finally, we fabricated a number of more intricate devices for interferometry experiments, also discussed in the additional future work in chapter 9.

4.3 Failure modes

Many devices were found to be non-conducting the first time they were measured after processing. Devices become non-conducting when there are not enough free carriers in the doped layer to form the 2DEG. The number of free carriers is reduced when either there are surface states (DX centres and dangling bonds) [51] that the carriers are confined to, or there is a floating charged region, such as a broken or blown-up gate. Figure 4.4 shows SEM images of some of these non-conducting devices, and highlights the failure modes that lead to rough surfaces and blown-up gates.

Rough surfaces most commonly occur because of poor quality shallow etches (blue circles). Figure 4.4a shows a device where surfactant prevented the etchant from

etching and left a thin bubbly film that could not be removed with RF ashing; this process is described in section 4.12. Figure 4.4b shows an inadvertently etched region. Figures 4.4c and 4.4d show an optically defined narrow etch; the poor resolution of the mask leads to a wavy edge. While the wavy edge could be a problem for conduction because of the increased number of surface states, it is certainly a problem in that the alignment marks for the EBL gates are poorly defined.

Blown-up gates most commonly occur when gates are introduced to a sudden static charge or voltage spikes, described in section 5.6. The mechanism by which gates blow up is not fully understood; but as they more frequently blow up in devices with small-feature sizes patterned close together, it is reasonable to assume that they blow up when the voltage across the gates is greater than the breakdown voltage of the dielectric. The breakdown voltage reduces exponentially with distance between the gates, and the large electric field creates a streamer discharge [52], which creates a region of local heating. Because the gates are so thin, the combination of local heating and sudden redistribution of charge is enough to physically destroy them, sometimes pulling up the GaAs/AlGaAs with them. Quantum pump devices are good examples of devices with small feature sizes patterned close together: gates run parallel for over 2 μm with a gap of only 100 nm. Both poor quality gates (red circles) and poor quality shallow etches (blue circles) increase the probability of gates blowing up. Poor quality gates with surface roughness have a gap that is even smaller than for smooth gates; many SEM images show gates that are possibly shorted. In addition to this, the electric field at a pointed feature of a rough edge is greater than that of a smooth edge. A poor quality etch with an undercut/deep etch profile makes the gates harder to climb without a discontinuity. The combined negative effects of the reduced gap between the gates, the increased local electric field for rough gates, and thin gates due to a poor shallow etch make quantum pumps extremely sensitive to poor quality gates and shallow etches.

Poor quality gates mostly occur when the thickness of the deposited metal is either too thick or too thin. If the gates are too thick, they can be shorted due to problems with lift off. If the gates are too thin, they may not climb the etch and become discontinuous. Figures 4.4c and 4.4e show gates that are too thick for the geometry, creating a short (red circle). Figures 4.4d and 4.4f show gates that

have blown up. Getting the gate thickness correct is one of the most important parts of making devices that conduct.

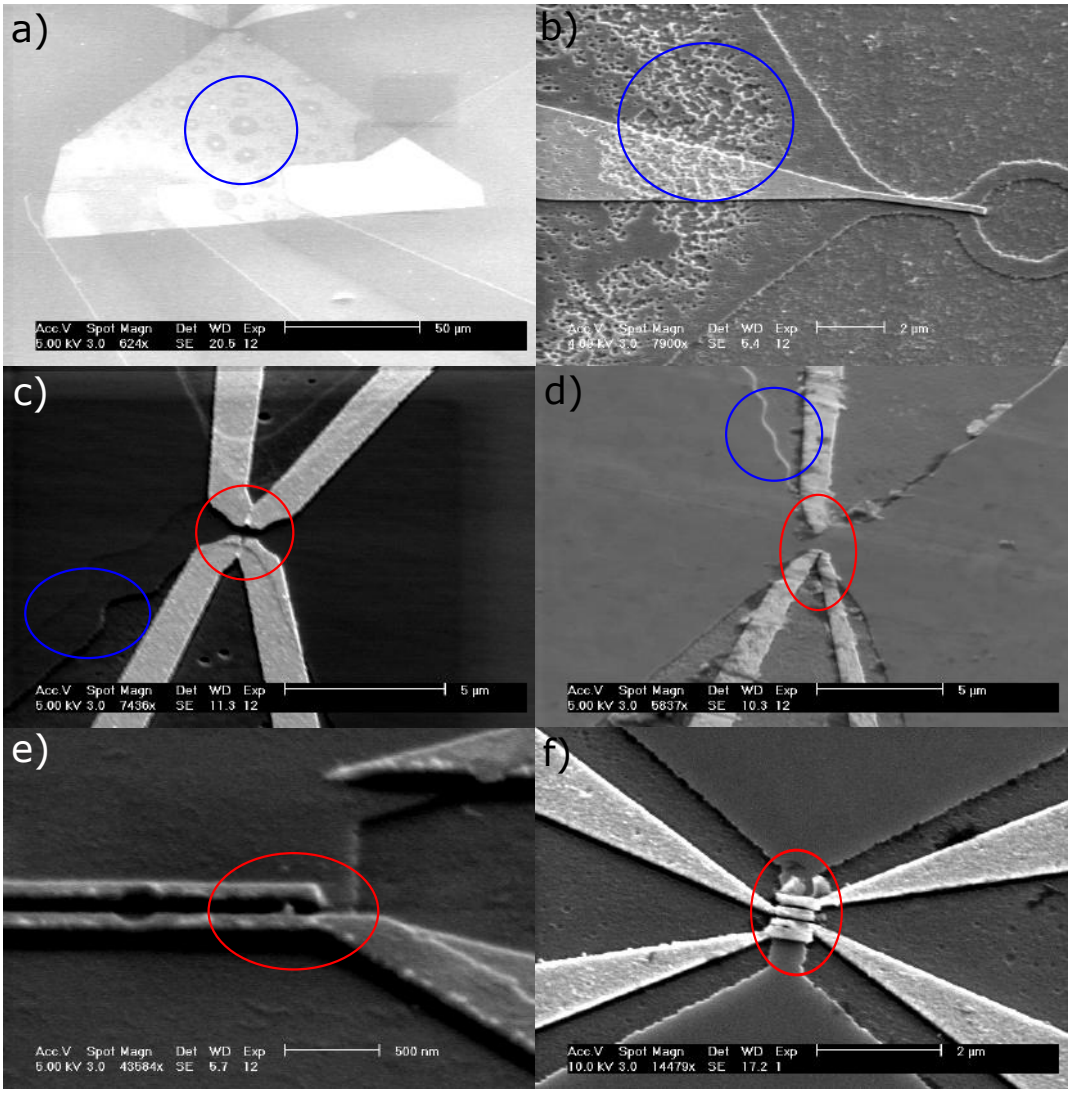

Figure 4.4: SEM images of the devices that are non-conducting and/or have blown up. Devices failed due to issues with the narrow etch (blue circles) and/or EBL gates (red circles). Descriptions of the failure modes of (a) through (f) are given in the text.

4.4 The cleanroom

Devices on the nanometer scale can be adversely affected or even completely destroyed by dust particles. Accordingly, all processing is done in a cleanroom where dust particles are kept to a minimum. In a cleanroom, a continuous airflow from the ceiling to floor pushes dust particles to the ground, and back to the ceiling through a filter. As a major potential source of dust is from workers in the cleanroom, all workers wear specialist cleanroom suits.

Metal gates on the nanometer scale are very sensitive to static charges. Once gates have been added, special care is needed to ensure that the devices do not encounter static charges during bonding and transport.

4.5 Wafer

We used standard GaAs/AlGaAs High Electron Mobility Transistor (HEMT) wafers grown in the Cavendish by Dr. Harvey Beere and Dr. Ian Farer using Molecular Beam Epitaxy (MBE), described below in section 4.5.1. Figure 4.5 shows the layer structure of a standard 40 nm HEMT. Layers of GaAs/AlGaAs are grown on the un-doped GaAs substrate. First, there is a 40 nm layer of un-doped AlGaAs to act as a spacer layer, which increases the carrier mobility in the 2DEG. Second, there is a 40 nm layer of doped AlGaAs that contains Si atoms to add carriers and modulation dope the wafer, creating the 2DEG. Finally, there is a 10 nm layer of un-doped GaAs, which simply acts as a protective capping layer. A typical wafer, V153, had a carrier density of 1.87×10^{15} m^{-2} and a mobility of 101 m^2/Vs in the dark at 1.5 K.

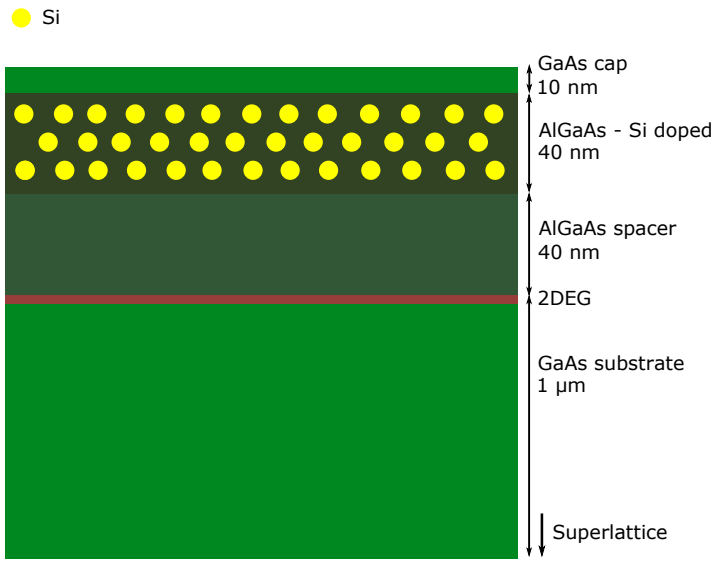

Figure 4.5: A diagram of the layer structure of the wafers used

4.5.1 Molecular Beam Epitaxy

To grow the wafer structure described above with a good carrier density and mobility, the interface between the layers needs to be very clean with as few defects as possible. In order to create a heterostructure without dislocations, only interfaces of layers with similar lattice constants can be grown. Respectively, GaAs and $Al_xGa_{1-x}As$ have lattice constants of 5.6533 A and 5.6533+0.0078x A [53]. They are similar enough to form a clean interface when $x < 0.33$. Figure 4.6a shows epitaxial growth at the GaAs/AlGaAs interface. To ensure the interface is uniform across the wafer, the wafer is grown slowly, one monolayer at a time. Figure 4.6b shows a diagram of the MBE chamber. The MBE chamber contains effusion cells, called Knudsen cells, which contain the individual elements that make up the wafer (Gs, As, Al, Si). In an ultra-high vacuum, the molecules from the Knudsen cells travel ballistically onto the substrate, and then rearrange themselves on the surface to form the next monolayer.

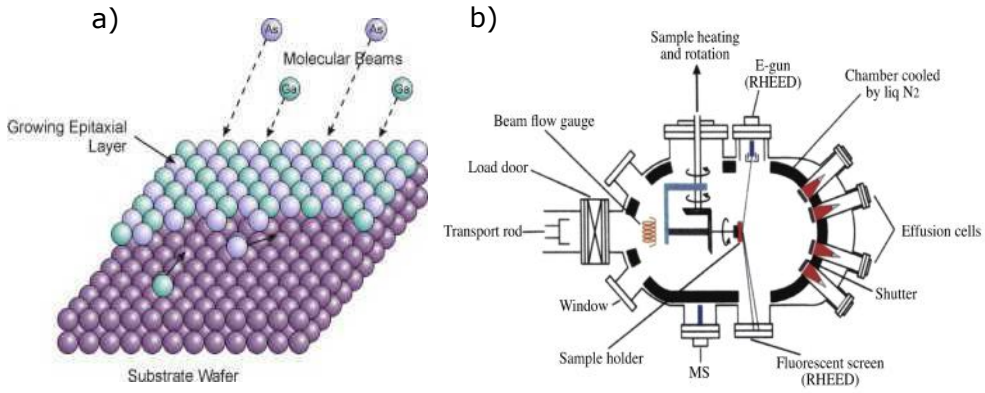

Figure 4.6: (a) A diagram showing epitaxial growth [Image taken from [54]] and (b) the MBE chamber [Image taken from [55]]

4.5.2 Failure mode considerations

In experiments where electrons are required to be ballistic, highly doped wafers are avoided because they do not have high mobility, and may parallel-conduct if the device is illuminated. However, as these characteristics are not important factors in quantum pump experiments, and high carrier concentration in the dark is important, we used highly doped wafers for the majority of devices. We have not seen any clear change in pump current accuracy when using lower doped wafers.

4.6 Mask

Processing requires from 3 to upward of 6 layers to be patterned, depending on whether oxides and/or top gates are added. The patterns could be made using either electron beam lithography (EBL) or optical lithography. Wherever possible, optical lithography is used because it allows for thicker gates, is much quicker, and is cheaper. Optical lithography requires a mask to pattern the relevant layers. The mask was used in 3 main optical processing steps: mesa, Ohmics, and gates.

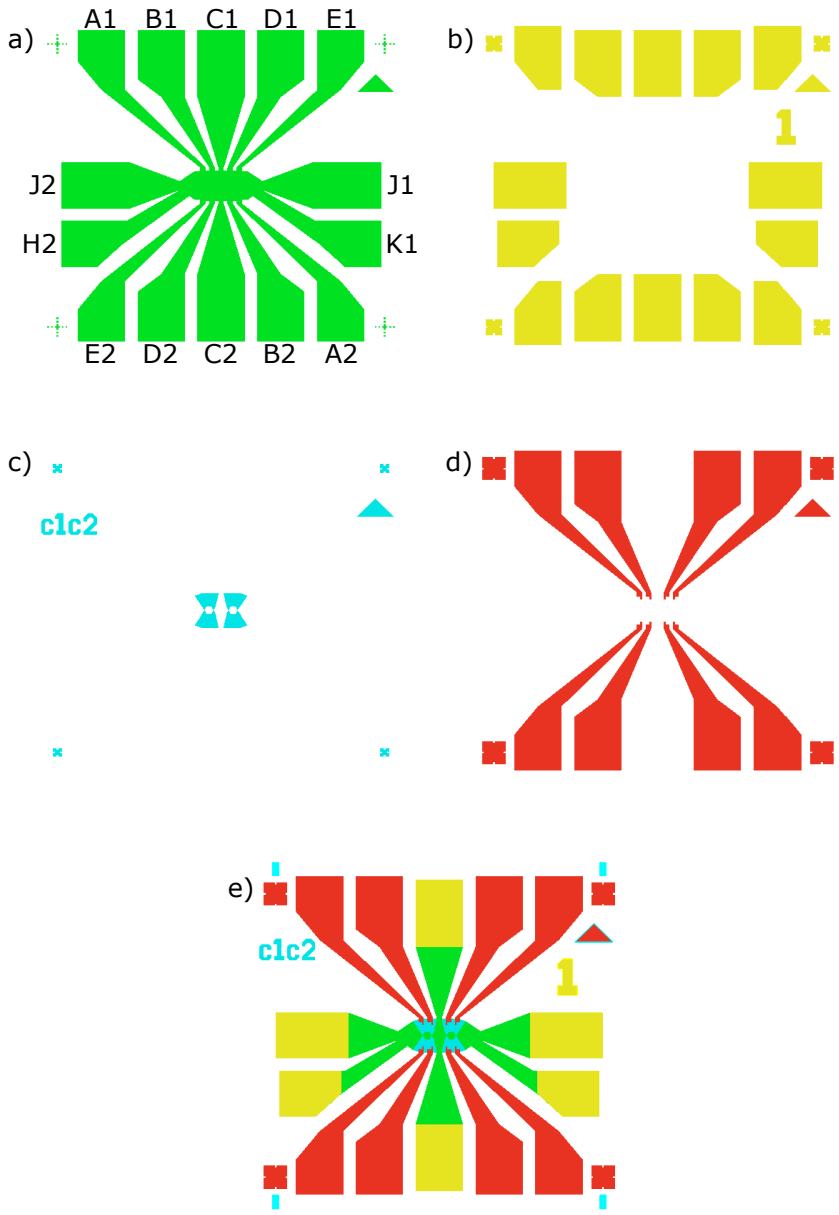

Figure 4.7: A schematic of HHH Mask, described below, showing the (a) mesa, (b) Ohmics, (c) narrow etch, (d) gates, and (e) the patterns overlaid.

Figure 4.7 shows some of the patterns of our newly designed mask, called the HHH Mask, which was adapted from Dr. Masaya Kataoka's NPL mask. Unlike a

normal Hall bar mask, the central region of the HHH Mask mesa (green) is large enough to accommodate many designs. Figure 4.7a shows the mesa. The large central region has 14 arms to which Ohmic contacts are made. The asymmetry of the mesa makes it easy to align, and the spaces on either side of the central region are available to ID the chip. Figure 4.7b shows the Ohmic pads. Combined with the mesa, this gives multiple combinations for 2 terminal and 4 terminal measurements. The Ohmic pads cover both the Ohmics and gates; this design gives more freedom as to which Ohmics, and which gates are used in the experiment. In addition, annealed Ohmics improve adhesion of the gates. The pads are numbered A1 $\rightarrow$ J2; the most often used combination was to measure using the Ohmics on C1,C2,J1,J2,K1,H2, and to use gates on the rest. To isolate the gate arms from the Ohmic arms, and to create a narrow channel for the pump, a secondary etch was done. Figure 4.7c shows the secondary etch channel. EBL is used for the region of gates with small feature sizes, but not for the entire gates. EBL gates are thinner than optical gates, and may be more difficult to bond to. Figure 4.7d shows the optical gates, which overlap the EBL gates to create one set of electrically continuous gates. Figure 4.7e shows the patterns overlaid for this mesa/secondary etch/gate combination. There are additional combinations for different experimental designs.

Because of the time and cost involved with doing an EBL stage, we experimented with optical lithography for the narrow etch, (Figure 4.7c). However, poor definition of the channel and alignment marks made it difficult to make well aligned devices, (Figure 4.4c); we have since had more success with EBL defined shallow etches.

4.6.1 Failure mode considerations

A possible reason for a non-conducting channel was the direct interaction of the gates with floating regions of 2DEG via the annealed pads, which might lead to gate leakage into the 2DEG. We experimented with the shallow etch depth to properly isolate the floating regions of 2DEG from the measured channel and did not find any gate leakage, so we kept the annealed Ohmics for the adhesion advantages.

4.7 Electron Beam Lithography

To produce lithographic features smaller than the diffraction limit of UV light, ($\approx$ 1.5 μm), a technique called electron-beam lithography (EBL) is used. EBL works by firing a focused beam of electrons at a polymer resist material such as poly-methyl-methacrylate (PMMA), and breaking up the polymer chains so they can be developed. The lithographic feature sizes of EBL is limited by the extent to which the beam reflects off the substrate and loses energy, transferring it to breaking down the PMMA, ($\approx$ 10 nm). An EBL machine is very similar to a SEM, except it can control the beam to raster user-defined patterns, rather than just the square viewing window of the SEM. Also, EBL machines have much more control of the electron-beam (ebeam) dosages. The majority of the fine-feature EBL for the devices in this thesis was done by Jon Griffiths at the Cavendish while additional EBL (protective cross-linking) was done by Dr. David English at the London Centre for Nanotechnology (LCN). EBL typically uses a much higher energy beam than SEM (30-50 keV vs. 5-10 keV). Electrons have a much smaller DeBroglie wavelength than the UV light used in the optical lithography, so the diffraction limit is smaller. The resolution of EBL is instead limited by the generation of low energy electrons, which have a larger effective interaction cross section. PMMA is exposed in regions where the electron comes to a halt and transfers its kinetic energy to breaking the polymer bonds. To create an undercut profile for gates, a bi-layer PMMA can be used. A PMMA with long polymers is layered on top of a PMMA with short polymers. The bottom layer is exposed more easily (with a lower dosage) than the top layer, creating the undercut.

4.8 Scribing and Cleaving

First, the wafer was scribed into the correct size of chip, which depended on the design of the optical mask and the number of devices required. Initially, the devices were made using a mask with a chip size of 2 mm $\times$ 2 mm and a periodicity of 2.2 mm, and later made using a new mask, HHH Mask described in section 4.6, with a periodicity of 2.4 mm. Wafers were most commonly scribed into 8 mm $\times$ 10.5 mm chips, with margins for edge-bead removal. The chips were

made with one edge parallel to the major flat, which was used to align the mesa.

A scriber, a machine with diamond tipped stylus, scores the wafer. Edges (roughly 1-4 mm) were scribed along the major or minor flat. The wafer was then transferred to a cleaving block, which has a step separating two planes. The wafer was placed such that the score overhangs the step, just parallel to it. The non-overhanging edge is secured with a glass slide while the overhanging edge is pushed gently with tweezers on the side with the score. The chip should break off cleanly, with the edge following one plane of the crystal lattice.

4.9 Cleaning

The devices were placed in acetone in an ultrasonic bath for 5 min, rinsed in isopropanol (IPA), and dried with N_2.

4.10 Optical mesa

For the reasons given in section 4.6, the mesa was first defined optically, then etched by wet etching, leaving regions of 2DEG where the channel was to be defined. As UV light exposes the resist, exposing and developing the mesa was done in a yellow room with UV light filters.

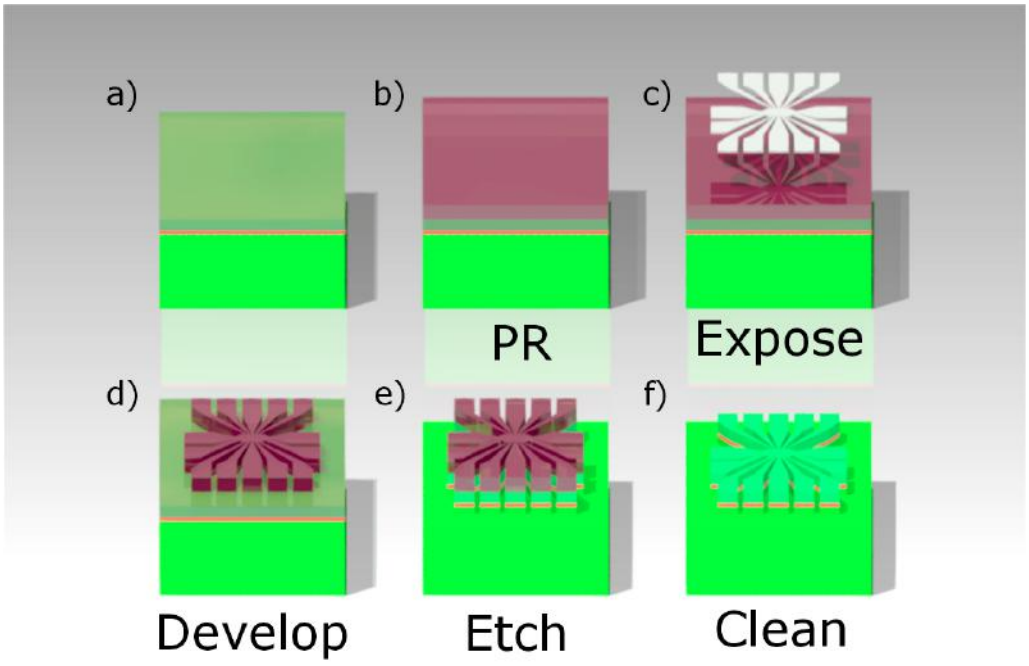

Figure 4.8: A diagram showing the steps to produce an etched mesa.

Figure 4.8 shows the procedure for creating the optically defined mesa. Figure 4.8a shows a diagram of the chip after cleaning. To ensure the chip was solvent-free, it was first pre-baked on a hotplate at 125°C for 5 minutes. Second, Shipley Microposit 1805 photoresist (PR) was spun onto the chip, (Figure 4.8b). The chip was then baked at 90°C for 2 minutes to harden the resist. Third, the devices were placed under a mask in an aligner and the mesa pattern was aligned such that the mesa channel was parallel to the major flat, and exposed with UV for 3.5 seconds, (Figure 4.8c). Fourth, the exposed resist was dissolved in MF-319 developer for 35 seconds, rinsed in DI water and dried with N_2, (Figure 4.8d). There should be no purple hue of photoresist left on the developed regions. To ensure the etch is consistent among devices, a hydrochloric acid (HCL) oxide removal stage was done prior to etch: the device was dipped in a dilute HCL:H_2O (1:5) mixture for 15 seconds and rinsed it in DI water. To etch the device, a mixture of sulphuric acid (H_2SO_4) and hydrogen peroxide (H_2O_2), which does not etch into the photoresist, was used. The H_2O_2 oxidises the surface of the device, and the H_2SO_4 removes the oxide. The etchant most frequently used was a H_2SO_4:H_2O_2:H_2O

(1:8:120), which etched at a rate of about 2 nm/s. The device was etched past the 2DEG, (Figure 4.8e), then rinsed in DI water and dried with N_2, (Figure 4.8f).

Before and after the etch, the devices were measured with a Dektak. The etch depth is given by the total depth after etching minus the depths of the photoresist. The etch depth should be $>$ 100nm for a standard 40nm HEMT.

4.11 Ohmics

To make an electrical connection to the 2DEG, we patterned and developed the Ohmics pattern from the HHH Mask, (Figure 4.7b), then evaporated and annealed the Ohmics.

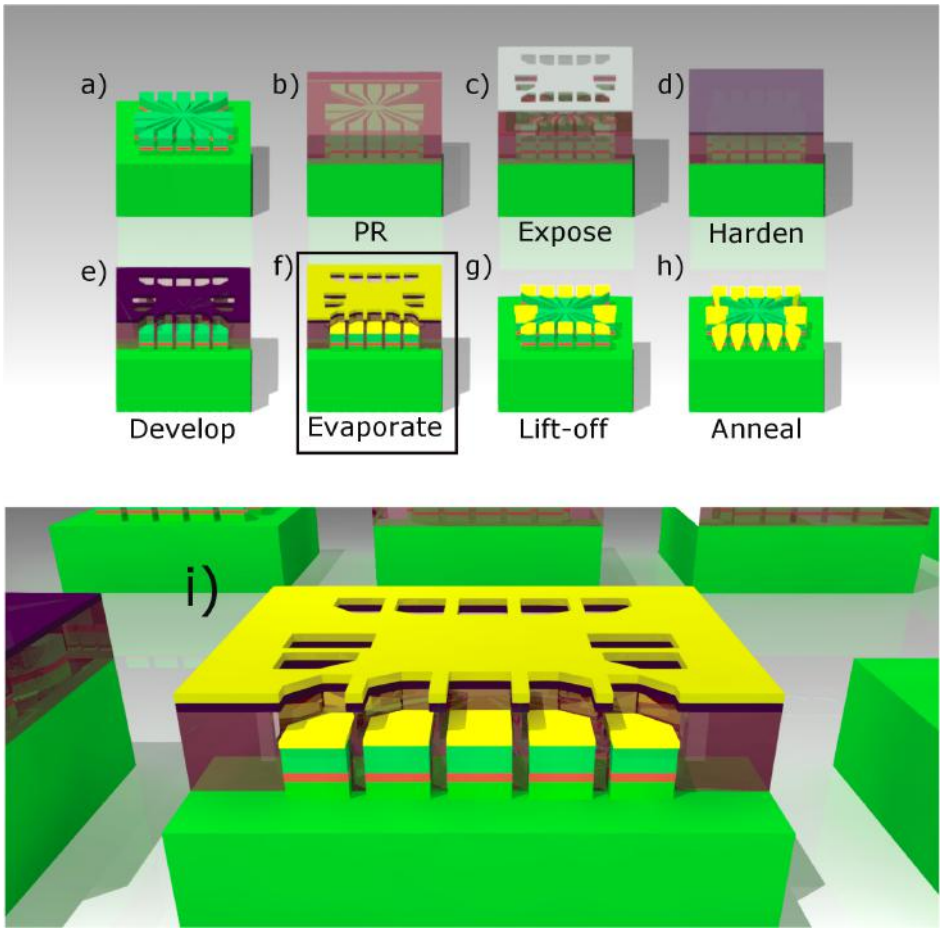

Figure 4.9: A diagram showing the steps to produce Ohmic contacts. Details of (a) through (h) are described in the text. (i) is a zoomed in diagram of (f) showing the undercut profile of the photoresist.

Figure 4.9 shows the procedure for creating Ohmic contacts. Figure 4.9a shows a diagram of the device with the mesa etched. It was first pre-baked at 125°C for 5 minutes. Second, Shipley Microposit 1813 was spun on it at 5500 rpm for 45 seconds, (Figure 4.9b). Third, it was baked at 90°C for 2 minutes. Fourth, it was placed in an aligner and the mesa was aligned to the Ohmics pattern using the alignment marks etched into the mesa, and exposed to UV light for 6.5 seconds, (Figure 4.9c). Before developing, the top of the photoresist was hardened so that when photoresist was developed it created an undercut profile, (Figure 4.9d). Hardening was done by placing the device in chlorobenzene for 1 minute then N_2 dried. It was then placed in MF-319 developer for 55 seconds, (Figure 4.9e). The developer takes longer to dissolve the hardened resist than the normal resist,

which creates the undercut profile necessary to ensure good lift-off. It was rinsed in DI water and N_2 dried. After the device was inspected under a microscope to ensure the PR was fully developed, an HCL oxide removal was done. This ensured that the evaporated metal made good contact and stuck. The oxide removal step was done as close as possible to the time the device was loaded in the evaporator.

The metal used was an AuGeNi alloy. The gold makes electrical contact, the germanium helps it diffuse, and the nickel smooths the gold diffusion and makes it stick. Figure 4.10 shows the evaporator; it consists of a tungsten boat that holds alloy slugs and a metal plate that holds the device, which faces the boat, all housed in a vacuum Bell jar. When a large current is passed through the boat, the alloy heats up and melts. As the boat is made of tungsten, which has a melting temperature twice that of AuGeNi, it does not melt. In a high vacuum (lower than $10^{-}6$ mbar for AuGeNi), the thermally evaporated AuGeNi does not scatter and gets deposited directly onto the device. The amount of deposited metal is measured using a crystal monitor. It works by resonating a quartz crystal at a known frequency and measuring the change in resonant frequency as metal is deposited onto it. The thickness of metal evaporated should be less than the undercut height, but sufficient for it to diffuse well into the 2DEG and be easy to bond to; usually this would be around 140 nm, (Figures 4.9f and 4.9i). Once the desired AuGeNi thickness is reached, a shutter that blocks the line-of-sight path from the boat to the device was closed. The AuGeNi was completely evaporated as the elements have different evaporation rates; this ensured the next user did not find any unwanted gold or germanium in the boat.

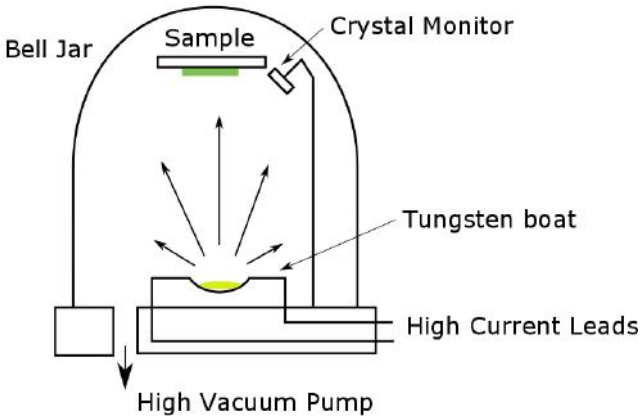

Figure 4.10: A diagram showing the evaporator.

After the evaporation, the device was placed in a sealed jar of acetone for an hour. As acetone evaporates quickly, the jar was sealed to prevent leaving the device with incomplete lift-off. If the metal is rippled, it indicates that the acetone has dissolved the photoresist under the metal and should be removed with a light squirt of acetone from a pipette, (Figure 4.9g). To put the metal Ohmics in electrical contact with the 2DEG, the AuGeNi pads were annealed using a rapid thermal annealer (RTA), which melts the AuGeNi at high temperature and allows it to diffuse into the device, (Figure 4.9f). A common annealing process is KEN01, which heats the device to 430°C for 80 seconds. The contacts were then tested on a probe station. It is a simple device that consists of two probes, which can be controlled with micro-manipulators, attached to a digital multimeter. For a standard 40 nm HEMT with a $> 1800\mu$m long and $> 80\mu$m wide channel, the resistance across a 2DEG at 300 K should be $R < 30$ kΩ in the light, $R < 50$ kΩ in the dark, and $R < 5$ kΩ in the dark at 77 K.

4.12 EBL mesa

The optically defined etch was 170 μm wide in the central region and 50 μm wide at its narrowest. To further etch the fine features of the mesa, to make it device-specific for the experiment being done, the device was patterned using EBL. For the majority of quantum pump experiments this meant patterning a narrow

channel with a width ranging from 700 nm to greater than 2 μm. The effective conduction width is smaller than the actual width due to sidewall depletion, where dangling bonds and DX scattering centres trap free electrons in the channel. The amount of depletion depends on the depth and roughness of the mesa etch. Such feature sizes are too small for optical lithography, so they are done with EBL.

To prepare the device for EBL, the device was RF-ashed for 40 seconds and HCL-dipped to de-scum and remove any oxide. Next, it was put in the oven for 20 minutes at 150°C to evaporate any solvents. Polymethyl-methacrylate (PMMA) 950K A4 Neat was spun on at 5500 rpm for 1 minute, baked for a further 10 minutes at 150°C to harden it, and submitted for EBL, the operation of which was described in section 4.7. Once the mesa was patterned, the device was developed in MIBK:IPA:MEK (5:15:1) fast-feature EBL developer for 8 seconds, rinsed in IPA, and dried with N_2.

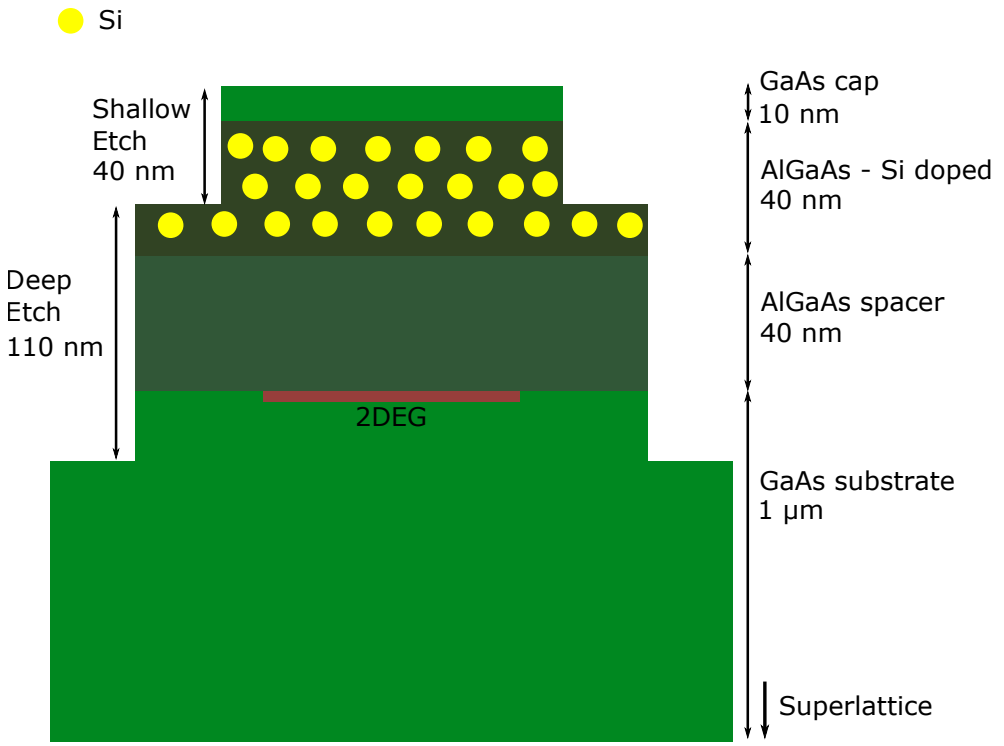

Figure 4.11: Diagram showing the relative depths of an optically patterned deep etch and an EBL patterned shallow etch.

The mesa etch is perhaps the most difficult stage of processing, as problems at

this stage seem to be the major reason why the yield has been low. Around the edge of the 2DEG electrons are trapped by DX scattering centres and dangling bonds. This is not a problem for wide channels, but it is for narrow channels. To address this problem we etched only partly into the dopant layer, (Figure 4.11). Because a shallow etch leaves some dopants to fulfil the surface states, more electrons remain in the channel, which helps the device conduct.

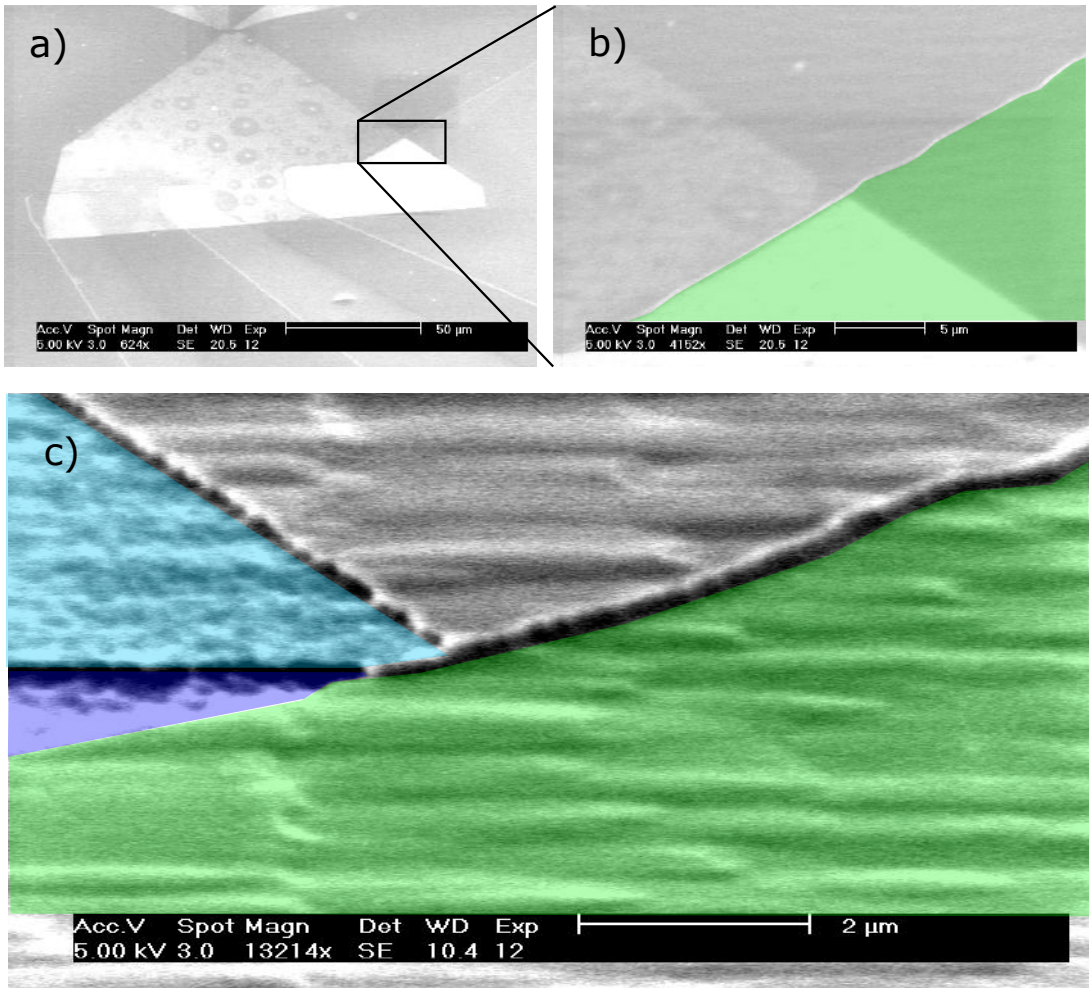

Figure 4.12: (a) An SEM image showing the deep and shallow using surfactant. (b) a zoomed-in false-colour image with the deep etch (green). (c) A shallow etch with no surfactant added (blue).

The devices were etched 20 nm into the doped AlGaAs layer, (30 nm including a 10 nm capping layer), (Figure 4.12c). In order to etch to the correct depth accurately, we scribed a row of devices for calibration. Directly before etching, the

calibrated chips were HCL-dipped to remove any oxide. To better calibrate the etch depth, and because the etch speed can have an affect on surface roughness, a slow etch solution was used: H_3PO_4:H_2O_2:H_2O (1:1:38), which has an etch rate of about 1 nm per second. Although the etch rate depends mainly on the percentage of H_2O_2 present and its distribution, heat and light can also effect the rate. Accordingly, the solution was left to stabilise for at least an hour before use and the device was etched in the shade. The procedure for etching is the same as for the optical etch, described in section 4.10, but with the slower etch solution. After etching, the device was placed in acetone for 2 minutes to remove the remaining PMMA, rinsed in IPA for 1 minute, and dried with N_2. The DekTak is only useful for measuring depths on the tens of nanometres scale, so the depth of the etch was checked using an atomic force microscope (AFM). Based on the measurements for the calibration devices, the etch times were adjusted accordingly.

After the shallow etch, the devices were checked on the probe station again to see if the shallow etch worked. The resistance of the narrow channel depends on the etch profile, wafer characteristics such as light and dark conduction, and the level of parallel conduction. However, we have found that invariably a working channel has a resistance of about 1.5× that of the wide channel. More importantly, there must be no conduction between the gates and the Ohmics to prevent gate leakage.

4.12.1 Failure mode considerations

The doping layer can be quite rough when it is etched into. To smooth the layer, both slower etching and adding a surfactant (Triton X) are often recommended [49]. However, after performing extensive comparative studies of different etch solutions we have found no evidence that either of these recommendations are effective. Indeed, we found that adding the surfactant was the major factor in our low yield. Rather than smoothing out the etch, the surfactant can form a thin film that shields the region to be etched from the etch solution. Worse, the thin film cannot be removed by RF-ashing or by dipping it in hydrofluoric acid (HF). Figure 4.12a shows a SEM image of a device that was etched using a solution with surfactant added. The etch solution did not etch the GaAs; instead

the surfactant formed a thin protective layer (light grey). Figure 4.12b shows a zoomed-in false-colour image; there is a stark contrast between the optical etch (green) and the thin film left by the surfactant. Figure 4.12c shows a false-colour SEM image of a shallow etch without surfactant (blue). The shallow etch was successful and the difference between the etch depths is clear. Figure 4.12c also shows that the surface of the shallow etch (blue) was much rougher than the surface of the deep etch (green), which we think is wafer dependent and linked to poor conduction through the channel.

The shallow etch is supposed to be smoothed by a dilute etch solution. Also, the dilute etch solution is supposed to allow for a better calibration of the etch rate [49]. We have not found evidence for either to be true. We have seen rough shallow etches and smooth shallow etches using both dilute and concentrated etch solutions, and attribute the roughness to inhomogeneity of the Al in the AlGaAs layer, because Al etches faster then GaAs. It is possible that a diluted etch gives a better etch calibration, but smaller concentrations of acid and peroxide make the etch solution more sensitive to small differences in the concentrations. There is a minimum amount of peroxide required to etch the device. It is possible that using a larger quantity of dilute etch solution would work, but we have not yet tested this. Finally, we think that edge roughness is a result of water sticking to the surface and shielding the device from the etch solution. This is not a problem for large etched regions because the movement of the device in the etch solution can dislodge any beaded water. When comparing shallow etches in GaAs to shallow etches in InGaAs, we note that the etch in InGaAs is always sharp. We think this is due to our not doing an HCL-dip prior to etching the device, which leaves a water residue on the device; accordingly, we recommend N_2 drying the device between HCL dipping and etching.

4.13 EBL gates

Two separate gate processing steps were required to form the gates: one, for grosser features, was patterned optically; the other, for fine features, was patterned using EBL. The minimum size that can be achieved with optical lithography is determined by the optical diffraction limit; for small features < 2 μm,

EBL must be used. Often, the EBL gates stage is done after the optical gates stage as there are fewer things to go wrong after processing, however there are advantages in doing the EBL gates first. Because optical gates are susceptible to lillypadding, described in section 4.14, and are much thicker than EBL gates, it is easier to form an electrically continuous gate if the EBL gate is deposited first.

The procedure to prepare the device for EBL gates is similar to the procedure to prepare the device for the EBL etch, except a bilayer PMMA was used to create an undercut profile, which assists in lift-off. The device was first RF-ashed for 40 seconds and HCL-dipped to de-scum and remove any oxide. Next, it was pre-baked in the oven for 20 minutes at 150°C to evaporate any solvents. PMMA 100K A6 Neat was spun on at 8000 rpm for 1 minute, and the device was baked on a 180°C hotplate for 3 minutes. The second layer of PMMA 950K A11:MIBK (1:5) is less viscous than the 100K A6 neat, so spins thinner, but requires a higher ebeam dosage to pattern, thus creating the undercut profile.

The solvent in the second layer PMMA will dissolve the first layer PMMA. Therefore, the device must be spun within a couple of seconds of pipetting the second layer PMMA. Finally, the device was oven-baked for a further 10 minutes at 150°C to harden the PMMA, and submitted to EBL. Once the gates were patterned, the device was developed in MIBK:IPA:MEK (5:15:1) fast-feature EBL developer for 8 seconds, rinsed in IPA, and dried with N_2.

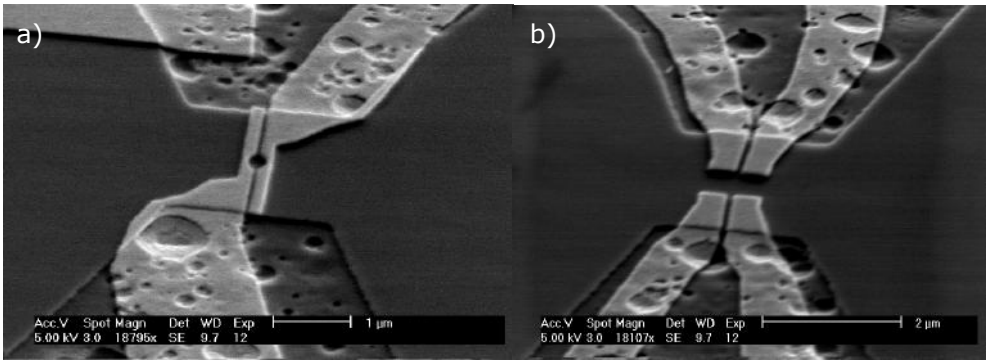

Figure 4.13: SEM image of a device with good EBL-gates

After developing the EBL gates, there are very small delicate regions of PMMA that may be compromised if left exposed; accordingly, the devices were developed

as close as possible to the time they were loaded into the evaporator. The gates evaporation is similar to Ohmics evaporation except it is a two-layer Ti/Au evaporation. To form a sticking layer between the gold and the GaAs, a thin layer of Ti (5-15 nm) was first evaporated, because the adhesion of Ti is much better than that of Au. Evaporating titanium requires a much higher vacuum (10^{-7} mbar) than gold (10^{-5} mbar). Following this, a thin layer of gold (20-40 nm) was evaporated, depending on the etch depth. Devices were left overnight in a sealed bottle of acetone; this is necessary for small feature sizes, as the acetone takes more time to dissolve the PMMA in the areas between the pump gates. Figures 4.13a and 4.13b shows an SEM images of gates with a correct amount of Ti/Au deposited, enough to climb the shallow etch but not too much that they short. After evaporating EBL gates, the device is very sensitive to static; accordingly, great care was taken in handling the device.

4.13.1 Failure mode considerations

Noting the possibility that the gates interacted directly with the dopants, we deposited a thin oxide layer by atomic layer deposition between the etch region and the EBL gates to isolate them. However, this did not appear to improve conduction. Another possible failure mode was the thin regions of gates due to surface roughness. Figure 4.13 shows craters in the shallow etched region that could lead to this.

4.14 Optical gates

Optical gates extend the EBL gates to the bonding pads. Processing optical gates is identical to processing Ohmics, described in section 4.11, with the exception that the gate pattern of the mask was exposed instead of the Ohmic pattern. We then evaporated Ti/Au (20 nm/100 nm) onto the device using the evaporation process described in section 4.13.

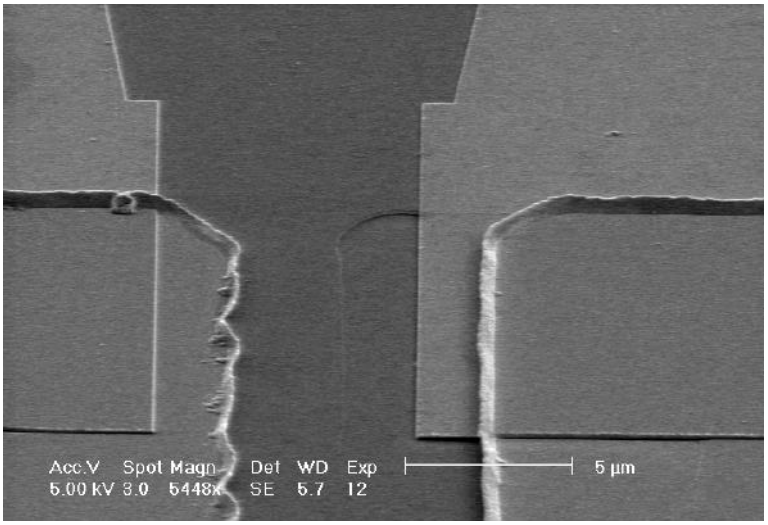

Figure 4.14: SEM image showing lillypadding of the optical gates, highlighted by the red oval.

Figure 4.14 shows the optical gate lillypadding (red oval), which is caused by the undercut profile of the photoresist. There are alternative steps to avoid this, such as lift-off resist (LOR). But layering the optical gates after the EBL gates works just as well. Further, even without lillypadding, the gold deposited for the EBL gates is about a third of the thickness of the gold deposited for the optical gates, making layering easier to ensure electrical contact.

4.15 Protecting the device

In section 5.6 we note a number of measurement failure modes and the necessary precautionary steps to avoid them. However, often devices blow up even after we had taken the necessary precautions. Accordingly, we experimented with protecting the devices by covering them in either SiOx or cross-linked PMMA. The reasoning is that while a spark may occur through the GaAs, the locally heated gated may be kept in place by the oxide layer. We tested the effectiveness of the protection of these devices by sequentially ignoring the precautionary steps and found them much harder to blow up. Figure 4.15a shows a device with 'good' gates. Figure 4.15b shows the same device covered in a layer of SiOx; the gates have the appearance of being melted but this appearance is just an artifact of

the SEM imaging the dielectric. In order to electrically contact the gates and Ohmics, we patterned pads on the device and dipped it in a buffered HF solution to etch the Oxide.

The above process protected the device well from static charges, shorting plugs, and building voltage spikes in the LCN Teslatron cryostat. However, we had already eliminated grounding loops from the system and outlined preventative loading steps, described in section 5.6. While it protected the device under those circumstances, it did not protect the device from grounding issues in the Cavendish MX40 cryostat. As an alternative to protecting it with SiOx, more recently we experimented with cross-linked PMMA over the delicate regions. The advantage of this method is that we can avoid the HF dip. Figure 4.16a shows an optical image of cross-linked PMMA over the gates and Figure 4.16b shows the corresponding SEM image of a similar device. The cross-linked region in Figure 4.16b is dark because it has no free electrons to excite and emit. It does not appear to have any adverse affects on the conduction through the channel, though it has yet to be tested in unfavourable conditions.

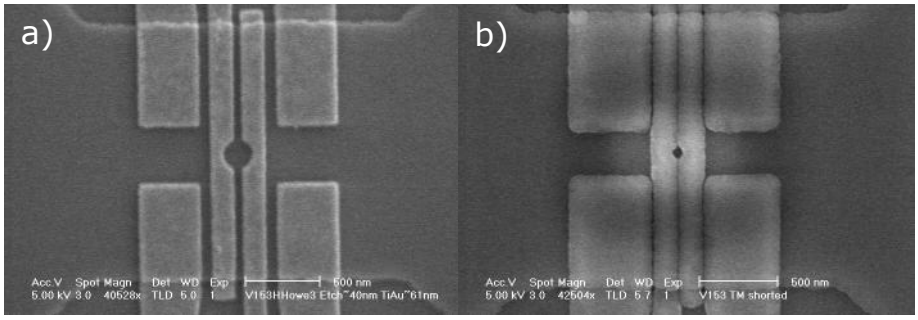

Figure 4.15: (a) SEM image of the device without oxide and (b) with oxide (b).

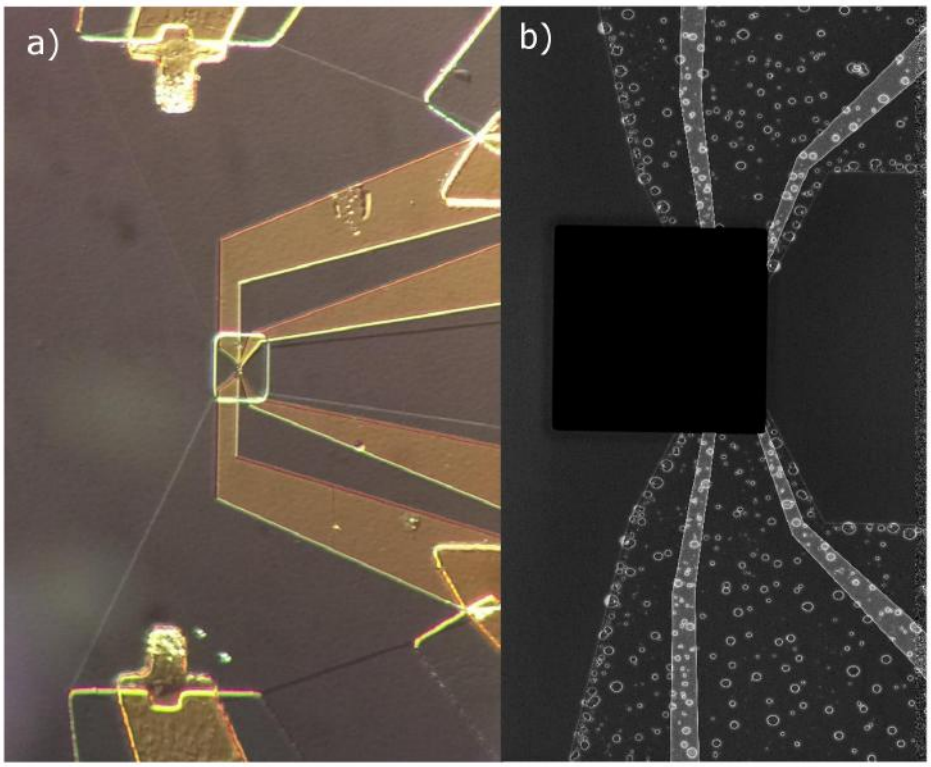

Figure 4.16: (a) Optical image of cross-linked PMMA and (b) SEM image of a similar device with a smaller square of cross-linked PMMA.

4.16 Packaging

Once the devices were completed, a layer of PR was spun on to protect them. Figure 4.17 shows devices housed in non-magnetic Leadless Chip Carriers (LCCs). Before the completed devices were housed, the pads on the back of the LCCs were bonded together; this gave them a common ground that prevented voltage spikes from the bonding machine to the gates. The chip was scribed and cleaved into individual devices as required, which were cleaned in acetone and IPA. LCCs were prepared with a ball of GE varnish and completed devices were mounted using toothpicks to hold them in position while the GE varnish hardened. Finally, they were bonded using either a ball bonder or wedge bonder.

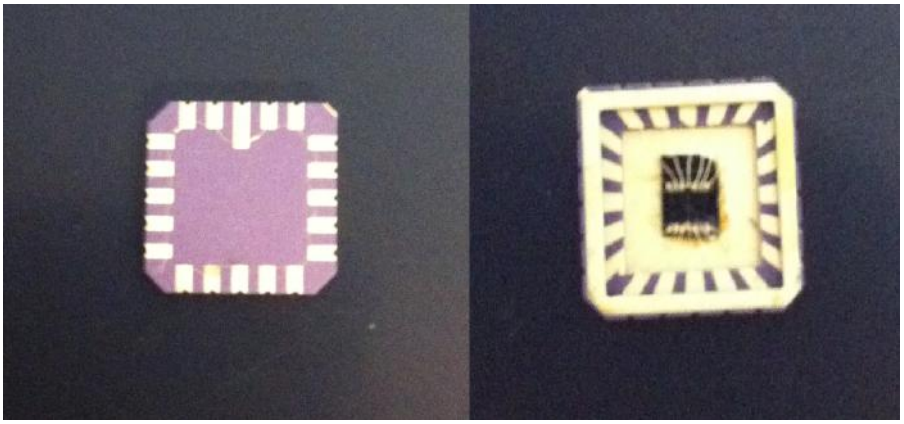

Figure 4.17: Image of an LCC showing the shorted pad before bonding the device (left) and the device bonded in the LCC (right)

The ball bonder is potentially very dangerous for the device as the ball is created by a spark that fires between a metal 'hammer' and the gold wire. In order to bond safely, the bonder was set to manual spark so it did not automatically spark near the device. To prepare for every bond, we removed the device, manually sparked the wire, creating the ball, left the hammer and wire to discharge for 30 seconds, touched them with grounded tweezers, returned the device to the bonder, reset the set point, and finally made the next bond. Alternatively, we used a wedge bonder.

For storage and transport, devices housed in LCCs were kept in static-free boxes, and the rest were coated with protective photoresist and kept in gel packs.

4.17 Summary

In this chapter we have set out steps to address many newly identified problems leading to device failure during processing. Chief among these are the quality of the narrow-etched channel, and quality of the EBL-defined gates.

Many of the new device failures are due to over-complicating the procedure in an attempt to make a better quality narrow-etched channel. For example, using surfactant created a thin film that prevented the etchant from etching the channel.

Changing the etchant to a more diluted etch solution did not smooth the shallow etch more than the standard mesa etch. The roughness is more wafer dependent than etchant dependent. We expect that N_2 drying the device between the HCL dip and the etch should prevent water beading and affecting the etch profile. Using an optically defined narrow etched leads to wavy edge and more crucially makes EBL gate alignment difficult. Finally, dispensing with the narrow channel leads to rectified current, detailed in chapter 6.

Most failures not due to a poor etch have been due to poor gates, which are either discontinuous, shorted, or rough. Using an insulating layer between the channel and the gates did not improve yield. The only thing that improved yield was getting the EBL gate thickness correct: thick enough to climb the shallow etch smoothly, yet thin enough that the gates do not become shorted. However, due to the small feature size, even gates that have been successful are prone to blowing up due to static charge and voltage spikes, the mechanism and prevention of which is detailed in section 5.6. Protecting the devices with a dielectric has helped make them more robust to these static charges and voltage spikes.

Chapter 5

Measurement setup

5.1 Introduction

All experiments on semiconductor heterostructures with a 2DEG require low temperatures to ensure that the electrons are confined in the 2DEG quantum well and not thermally excited over the barriers. Particular experiments, such as Coulomb blockade measurements, require even lower temperatures to suppress thermal broadening effects above 300 mK. It is probable that the thermal broadening effects that limit the accuracy of Coulomb blockade measurements also limit high accuracy pump measurements.

After fabrication, the first stage of testing our devices is performed in either a 4.2 K Helium 4 dewar, described in section 5.3.1, or a 2.4 K Helium pulse tube dry system to ensure that the 2DEG channel was conducting and that the gates pinched off at low temperature. If the tests were successful, we measured the devices on a number of different cryostats in the LCN and the Cavendish Laboratory, that ranged from 8 mK to 14 K, described in section 5.3.2, then in a Helium 4 dewar at 4.2 K for the remainder of the experiments presented in chapters 6 and 7.

In this chapter we first describe the sample holder we designed that provides electrical contact between the devices and the measurement setup. We then describe the cryostats and discuss why our measurements were more successful

in some cryostats than in others. We then discuss the instrument set up and finally we discuss the various failure modes that we reason were responsible for the majority of devices failures.

5.2 Sample holder

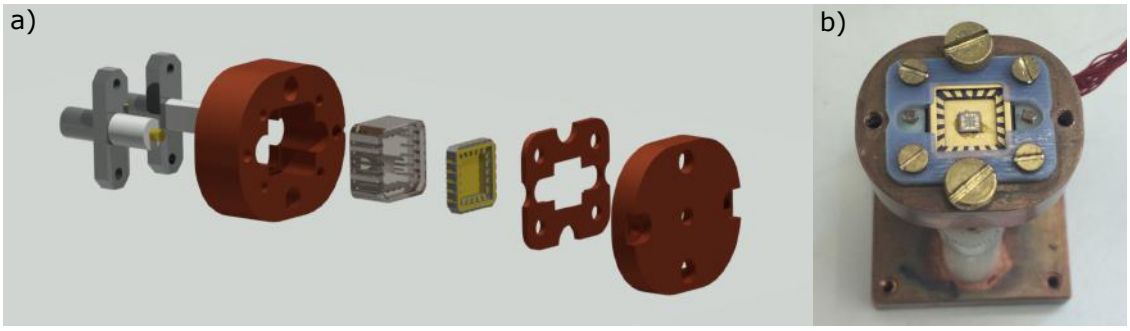

Figure 5.1: (a) A diagram showing an exploded view of the sample holder components and (b) a photo of it assembled.

A RF sample holder is more challenging to design than a DC sample holder. Unlike a DC sample holder, the RF holder must be impedance-matched to avoid power loss through reflections and standing waves in the RF lines. The RF lines in the probe were semi-rigid coaxial cables with a characteristic impedance of 50 Ω, (the square root of the ratio of the inductance to capacitance, per unit length). When neither the gold wire used to bond the RF lines to the device nor the gates on the device are impedance-matched, RF power is lost due to reflections at the wire interfaces. To minimise the loss, we made the bond wires as short as possible to make them transparent to the RF signal. Standing waves occur at multiples of the RF wavelength, which for a 1 GHz signal is $\approx$ 30 cm, our bond wires were $\approx$ 0.5 cm, the minimum distance possible for a sample holder that incorporates an LCC, therefore there should be no standing waves in the bond wires.

Our sample holder incorporates the better features of two sample holders: one designed by Dr Samuel Wright [42], the other by the National Physical Laboratory (NPL). Wright's sample holders take LCCs, but are poorly impedance-matched, due to it having an off-the-shelf DC LCC socket. In addition, the designated

RF pin of the LCC cannot be changed, which limits experimental versatility. NPL's sample holders are very versatile because devices are bonded to a custom PCB board. They are better impedance matched that Wright's because the coaxial lines are bonded directly to the device. However, because they do not take LCCs, devices cannot be easily swapped in and out of them. Both Wright's and NPL's sample holders were too large to fit into the sample space of an Oxford Instruments Triton dilution fridge, which is limited by the magnet bore. Our hybrid sample holder, which fits in the available sample space, is the smallest RF sample holder of its kind - 24 mm at its widest - to house an LCC and bond directly to the RF coaxial lines. To achieve this small size, our sample holder uses pogo pins to make a customised LCC socket and straight coaxial terminations that flank the socket. Because the sample holder uses pogo pins, it is extremely versatile and can be used in place of a normal DC LCC socket as well as for RF measurements.

Figure 5.1a shows the design of the sample holder in an exploded view. From left to right the components are the SMA connectors, casing, insert, LCC, clamp, and lid. The SMA connectors are a straight-through flange-mount connectors that fit flush to the insert. The casing is made from oxygen-free copper, which, although it has lower electrical conductivity than regular copper, is less likely to oxidise and degas. The insert is made from HySol, a cryogenic-specific material with good insulating and thermal expansion properties. It has holes to house the pogo pins, which are spring-loaded and create a pressure contact with the LCC, and a recess to fit the LCC in one orientation only. The clamp has a mirrored recess to the insert to further ensure the LCC has the correct orientation. It has holes for four mounting screws and a cutout for both the device and two coaxial terminations. Finally, the lid is recessed to house the clamp. It has holes for two mounting screws. The casing, clamp, and lid have two 3 mm holes to mount the sample holder to the probe. All connectors and gold plating are non-magnetic (nickel-free) to prevent magnetic hysteresis at low magnetic fields. Figure 5.1b shows the assembled sample holder with a prototype 3D printed clamp. The RF bond is from the coaxial termination, over the LCC, to the device.

The production of this sample holder has been one of the key factors in improving the pump devices, and is starting to be used by other groups requiring RF sample holders.

5.3 Cryostats

5.3.1 He4 dewar

We follow the common practice of doing all testing in a dipping station prior to lower temperature measurements. The biggest advantage of a dipping station is the quick turnaround time; samples can be cooled to 4.2 K in 30 min and warmed back to room temperature in 15 min if they are found to be not working. Figure 5.2a shows a typical helium dewar. Figure 5.2b shows our RF dipping probe. We designed the head of the RF dipping probe to accommodate our sample holder; it has a recess for the mating D-subminiature connectors, (Figure 5.2c), and a sheath to contain the sample holder and wiring, (Figure 5.2d). We also designed the breakout box with shorting switches on all RF and DC lines; these switches are vital as plugging and unplugging shorting plugs often blew up our devices. As the measurement setup is the same for all systems it is described separately in section 5.4.

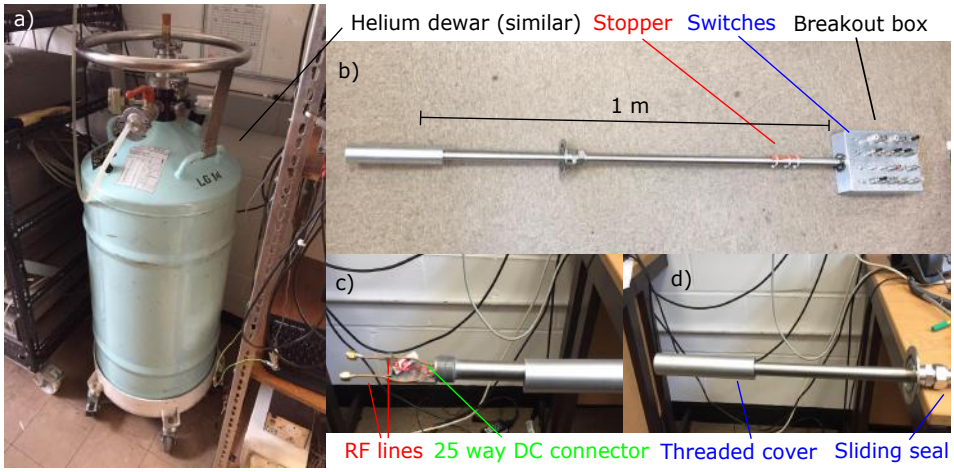

Figure 5.2: (a) Photograph of the helium dewar. (b) The dewar probe. (c) The sample end of the probe open showing the RF lines and the 25 way DC connector. (d) The probe closed with the threaded cover.

To ensure that there was sufficient helium to immerse the sample, and to provide a measurement of how far to lower the sample to ensure immersion without excessive helium boil-off, the helium level was measured using a dipstick. The dipstick is made of a thin hollow tube that is open at one end and has a membrane

fixed to the other. As the open end is lowered into the dewar, the membrane vibrates because of the thermoacoustic effect, where a temperature gradient creates a standing wave in the tube.

5.3.2 He4 dry system

To reach temperatures below 4.2 K, we used cryostats with a multistage pulse tube refrigerator (PTR). Figure 5.3a shows a schematic of a 2 stage PTR. The PTR consists of a piston to compress the gas, a regenerator to store the heat, a pulse tube to form the thermal and pressure gradient between the cold end and the room temperature end, a small valve, and a room temperature reservoir of the working gas (Helium 4). PTR is an isentropic process that cools the cold end by an enthalpy transfer from the regenerator to the reservoir [56]. One difference between the schematic and most PTRs is instead of compressing the helium using a piston, which would introduce large mechanical vibrations, the helium is compressed in an external compressor and throttled into the PTR by a pulsating throttle valve. Figure 5.3b shows a picture of the Oxford Instruments Teslatron cryostat in the LCN and the location of the PTR on the cryostat. The PTR brings cold plates in the cryostat to $T < 4.2$ K, which is cold enough to liquefy helium. In addition to the PTR, the Teslatron cryostat has a separate He4 cooling circuit that works on evaporative cooling to bring the operating temperature down to 1.6 K. The cryostat has an 8 T magnet and can be set to any temperature up to 300 K by small heaters near the sample (with the magnet off). Figure 5.3c shows the sample end of the probe on which the sample holder described above attaches.

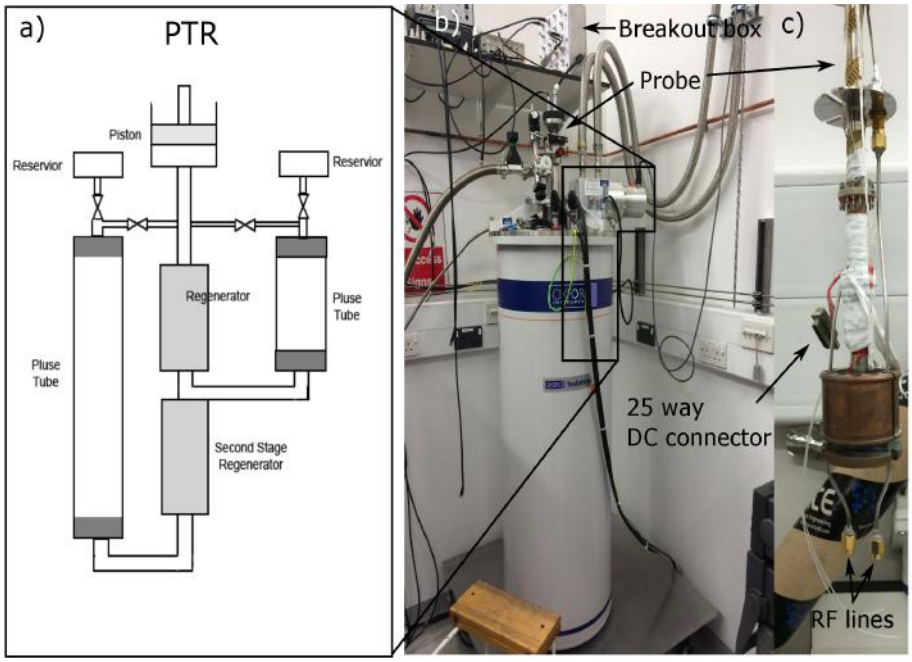

Figure 5.3: (a) A schematic of the pulse tube refrigerator [image taken from [56]]. (b) Oxford Instruments Teslatron He4 system with the 1.5 K probe inserted. (c) The sample end of the probe.

In addition to the Teslatron, we used a small Oxford Instruments 2.6 K cryostat to initially test our devices, in a similar way to the He4 dewar. Figure 5.4a shows an older generation of the sample holder mounted on a cold finger base plate. Figure 5.4b shows the PTR mounted above sample space and the breakout box used.

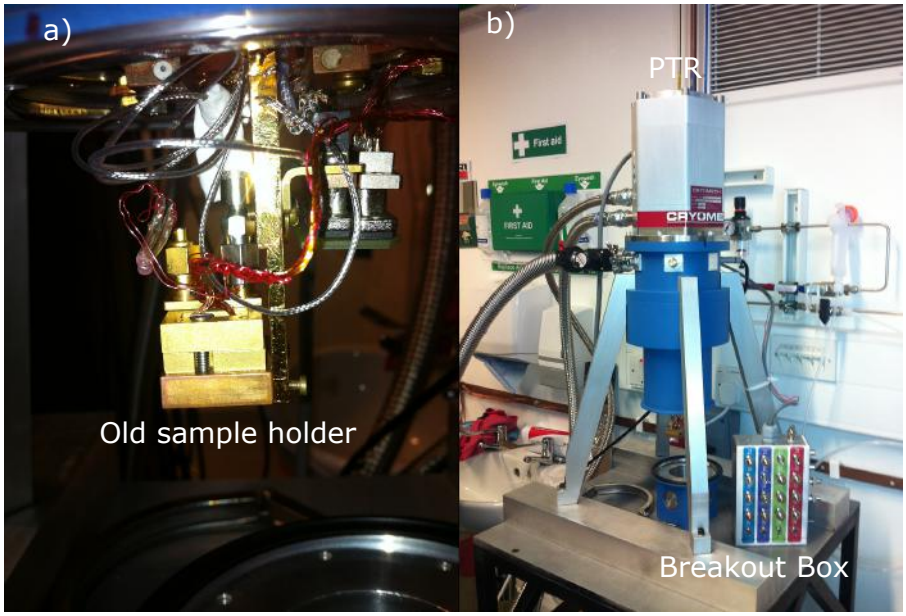

Figure 5.4: Oxford Instruments Optistat He4 system showing (a) a close up of the sample holder mounted in the system and (b) the pulse tube and break-out box.

We limit the results presented in this thesis to experiments performed on the Teslatron cryostat and the He4 dewar described above. We have performed experiments at lower temperatures using a Helium 3 insert (260 mK) and a dilution fridge (8 mK), but due to experimental difficulties with the grounding of the RF lines much of this work is incomplete; it is presented as future work.

5.4 Instruments and measurement circuit

In all our measurements, we used the same electronic rack and software. The rack comprised a Keithley 2636a source-measure unit (SMU), a National Instruments 9269 cDAQ digital to analogue converter (DAC), and a Hewlett Packard HP8657B RF source. These instruments were controlled through Modulab, a LabVIEW software first developed at Physikalisch-Technische Bundesanstalt (PTB). It allows measurement sweeps to be performed as nested loops, which is ideal for taking pump map data: additional loops allow a parameter to be incrementally stepped while an I-V curve is swept, e.g. to see how a pump map varies with

RF amplitude or frequency. Figure 5.5 shows a schematic of the circuit diagram used in the bulk of our measurements. The Ohmic lines (blue) are connected to a breakout box via the DC lines in the sample holder and then to the live and ground of a SMU. The DC gates (green) are connected to the breakout box via the DC lines in the sample holder and then to a DAC. The RF gates (red) are connected to the breakout box via the semi-rigid coaxial line and then to the RF source. The yellow dot and arrow indicate the location of the quantum dot and the direction of pumping.

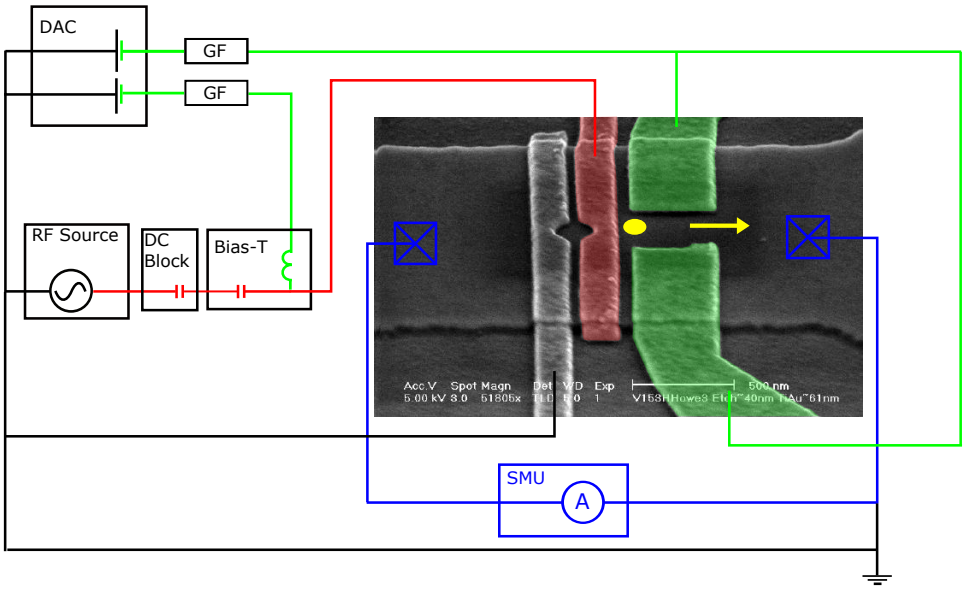

Figure 5.5: Schematic of measurement setup.

In addition to the three active components, we used a number of passive components: a Bias-T to add the DC and RF signals, gate filters (GF) to protect the devices, and an inner/outer DC block to prevent ground loops. A Bias-T is a junction that comprises a capacitor and an inductor. A gate filter is a simple RC low-pass filter circuit that protects the device against voltage spikes by attenuating high frequency signals. Gate filters store energy in a capacitor and slowly dissipate it through a resistor. The limit of frequencies that are not heavily attenuated is given by the inverse of the time constant, $f_{\max} = 1/(2\pi RC)$. The DC block used comprises an inner and outer capacitor to isolate the RF ground from the measurement ground. This prevents a ground loop between the measurement ground (SMU) and the RF-source, described in section 5.5.

5.5 Ground loops

When two instruments are connected to ground at different potentials, currents are driven around a ground loop. Figure 5.6 shows the measurement circuit with and without ground loops. The ideal measurement setup has the measurement circuit isolated from the cryostat circuit except for a common ground potential. Realistically, the ground that the measurement circuit is plugged into will go through many other instruments in the building before reaching the earthing rod, which is a physical rod that is dug into the ground and represents a clean earth. Changes in voltages through these additional pieces of equipment can create voltage spikes through the measurement circuit. At best they are filtered out and may only slightly affect the measured signal, at worst they can blow up a device. Even without spikes, the voltages added when adding instruments in series can offset the measurements, e.g. a 3 mV difference between the cryostat ground and the PC ground. When a clean earth is installed, the earthing rod needs to be placed far enough away from other earthing rods so they are not inductively coupled. A clean earth that runs parallel to a dirty earth can be worse than a dirty earth.

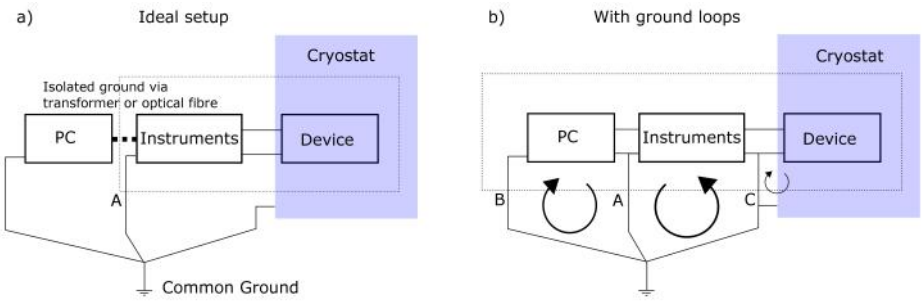

Figure 5.6: (a) Ideal grounding setup and (b) a circuit with ground loops.

To eliminate the ground loop between the PC and the DAC we isolate the grounds using an isolating transformer, and to eliminate the ground loop between the PC and the RF-source we isolate the grounds using an inner/outer DC block on the RF line. Figure 5.7 shows an Ohmic device with and without the DC block. The addition of the DC block centres the zero-bias offset current to zero.

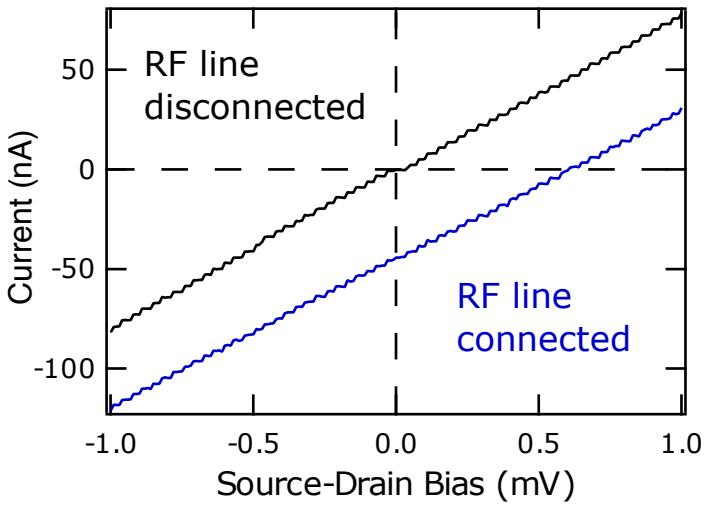

Figure 5.7: Plot of current vs. source-drain bias showing a channel with a normal Ohmic response (black) and with an additional offset due to a ground loop through the RF source (blue).

5.6 Sample loading and failure modes

Assuming devices were still conducting after processing, there are several loading and measuring stages during which the devices may fail. In this section we describe the stages, some device failures, and our steps to prevent those failures. Some of the preventative steps we describe are taken in other experiments with electrostatic-sensitive devices and taken in NPL; but more steps are described here to help identify points of failure.

The majority of devices failed to conduct when they were first connected to the probe; they could have been destroyed from the end of processing to mounting on the probe, mainly due to static charge buildup. To prevent this, we wore a grounding bracelet when loading the device into a sample holder, handled the LCC only at the corners, and sequentially re-grounded the device through to the SMU measurement ground. We grounded the sample holder while loading the LCC, connected the sample holder ground to the probe ground before connecting the DC lines to the sample holder, connected the probe ground to the SMU

ground, and grounded the Bayonet NeillConcelman (BNC) cables connected to the SMU before connecting any of them to the probe. Prior to our protecting the devices with an oxide layer, described in section 4.15, often these steps were insufficient to ensure they remained conducting by this stage.

We use the SMU to test if the channel is Ohmic by sweeping the source-drain bias voltage from -1 mV to 1 mV and recording a liner current response, hereafter called Ohmic testing. We never use a handheld digital multimeter (DMM) to do Ohmic testing, as we cannot set compliance limits on the current. The resistance depends mostly on the wafer and the width and quality of the narrow channel; but the resistance for conducting device with a 2 μm wide channel should be approximately 200 kΩ. When a device conducted at room temperature in the light, we repeated Ohmic testing in the dark. The increase in resistance in the dark depends on the wafer; but it should be approximately 1.2$\times$ the resistance in the light. In non-conducting devices, the device can still conduct in the light with a resistance of approximately 200 kΩ, due to photoelectric current, but will increase to $>$ 5 MΩ in the dark.

When a device conducted in the dark, we removed the sample holder from the probe, ensuring that the grounds were disconnected sequentially, and bonded the RF lines. After bonding, we remounted the sample holder following the precautions described above and tested the Ohmics again. Initially, many devices stopped conducting after we bonded the RF lines in older sample holders, but fewer stopped conducting after we used our sample holder described in section 5.2. We mounted the sample holder on a grounded sample holder stage to bond the RF lines and bonded from the RF line to the device to prevent static discharges from the bonder. If a device still conducted in the dark with the RF lines bonded, we connected the DC gates and RF lines, then cooled the device with a 1 mV source-drain bias to monitor the conduction throughout cooling. Figure 5.8 shows the current during cooling for a good sample. At lower temperatures, the 2DEG becomes more conductive, while the Ohmics become less conductive. It is common for the current to increase initially but then fall slightly as the resistance is dominated by the Ohmics.

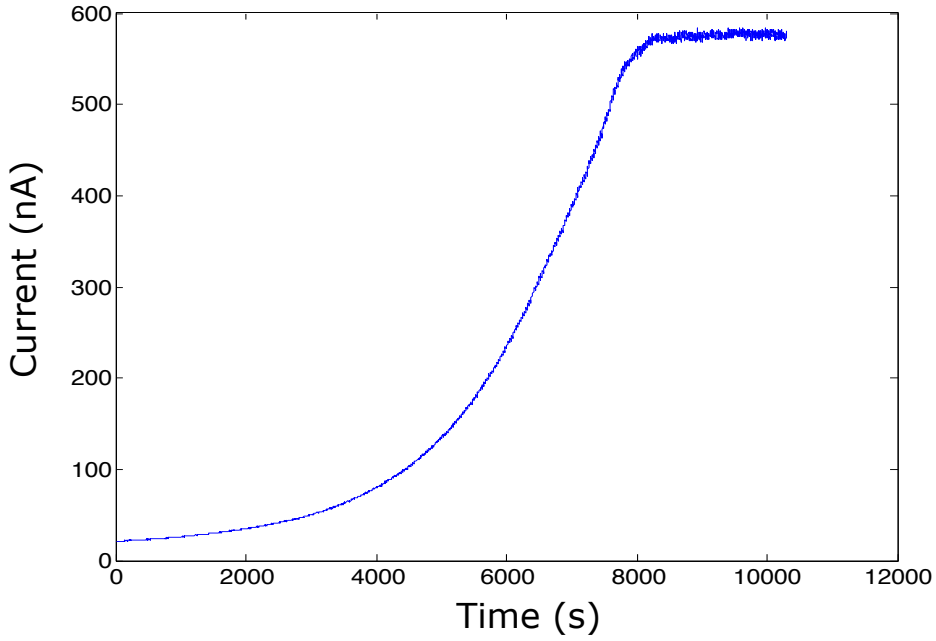

Figure 5.8: Plot of current while cooling showing the increased conduction while the 2DEG is formed.

Often the device would stop conducting during cooling: this was either a gradual decrease or a sudden drop in current.

The gradual decrease occurs when the channel is actually non-conducting and all the current measured at room temperature is due to bulk parallel conduction. This parallel conduction is caused by a combination of infrared photo-conduction and thermal excitation of electrons out of the 2DEG, which are both reduced when the device is cooled. The sudden drop is due to a voltage spike destroying the device. If the instrument ground is shared with a common building ground, voltage spikes that occur on any part of the shared ground can destroy the device. To protect the device against these spikes, we used low pass filters on all the gate lines, and later on the Ohmic lines as well. However, because filters could not be used on the RF lines, using filters on the gates and Ohmics was often insufficient to protect a device.

Chapter 6

Rectified current

6.1 Introduction

Sections 4.3 and 5.6 describe the problems with channel conduction through narrow etched wires. As narrow-etch wires do not provide quantum confinement in gate-defined quantum pumps, we experimented with devices with no narrow-etched channel in an attempt to improve yield. While this solved the problems of channel conduction, it introduced an unforeseen problem that prevented us from observing quantised pumped current. We used the same measurement setup as described in section 5.4. When we put a source-drain voltage bias across the device and applied a negative voltage to a gate to pinch off the 2DEG channel below it, the current through the channel became negative, as highlighted by the red circle in Figure 6.1. We have seen this effect in many devices, from narrow-etch wire pumps, where the effect is small, to non-etch channel pump devices and standard top-gated Hall bars, where the effect is much larger. The origin of this current appears to be AC driven. We noticed that, in addition to a DC voltage sweep, applying an additional AC voltage increased the amount of negative current. On the assumption that this is an AC effect that generates a DC current, the current is called rectified, I_R. Discussions with colleagues working in the SAW group at the Cavendish laboratory have revealed that this is a common issue, although it is rarely reported in the literature. There are two reports of this type of rectified current in non-pump devices that discuss its impact, but do not

provide an explanation of its origin [57–59]. Additionally, there is one paper that explicitly refers to its effect on pump devices [60], in which the authors explain it as due to a parasitic coupling between an RF gate and the 2DEG. They provide the argument that I_R is generated by asymmetric pick-up of the 2DEG on the source and drain. They conclude that I_R is 1 part in 10^{12} of a pump current of 100 pA, but they use a lock-in measurement setup that is different from the DC measurement setup used to measure pumped current. However, when we measure I_R using the same DC setup that we use to measure pumped current, in our devices with no narrow-etch channel, I_R is much larger than the intentionally pumped current, and swamps any single electron features. The understanding provided by these above papers is not sufficient to fully account for the rectified current that we observe in a device with no etched channel. In order to observe quantised pump current in these devices, we need to first understand the origins of I_R, the extent to which it dominates quantised pump current, and explore methods to suppress it. Accordingly, we develop a model to explain the effect, described in section 6.2, and investigate the effects of changing the controllable parameters: amplitude, frequency, and series resistance in later sections.

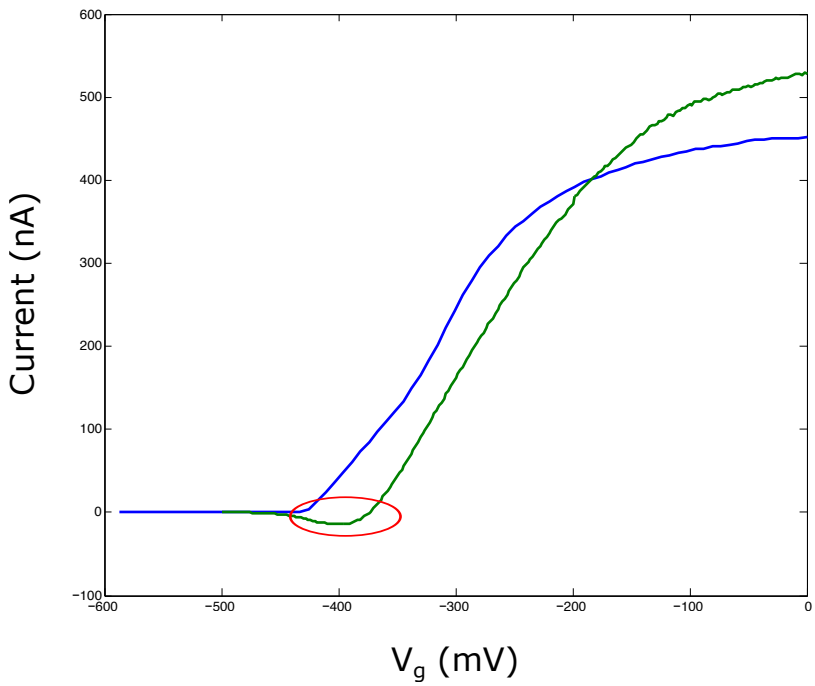

Figure 6.1: A plot of current vs. gate voltage showing a normal pinch off curve (blue) and a pinch off curve with rectified current (green).

Although the circuit has many gates, to observe rectified current we need only one to oscillate (red). This oscillation can be intentionally added with an RF source, or unintentionally added by radio pickup. As we hope to expand the integration of pumps into a wide variety of more complicated devices beyond those with single etched channels, it is important to understand these effects in a simple device.

In this chapter, we model a process we believe to be responsible for generating I_R, simulate it, and compare it with measured I_R over a range of controllable parameters: amplitude, frequency, and series resistance. By examining how the simulated and measured I_R compare for the different parameters, we identify which can be utilised to reduce I_R. We also consider how different circuit elements can impact I_R.

6.2 Model of rectified current

Our model of the process that generates rectified current is based on a net charge transfer through an electrometer during the positive and negative parts of an AC cycle. The model uses a changing channel conductance to explain I_R, similar to the process in the NPL paper [60], but the description of the mechanism is based on a different circuit and does not require an arbitrary out-of-phase coupling of the gate to the 2DEG. In this section, we describe the stages of the process and make assumptions about the physical mechanisms involved.

6.2.1 Simplified circuit

We first illustrate the process using a simplified circuit (Figure 6.2) and identify the minimum requirements needed to generate I_R. Unlike the full circuit, discussed in section 6.2.2, the simplified circuit does not map well to the real device. However, because it is a reducible circuit, it leads to a more intuitive derivation of the pumped current.

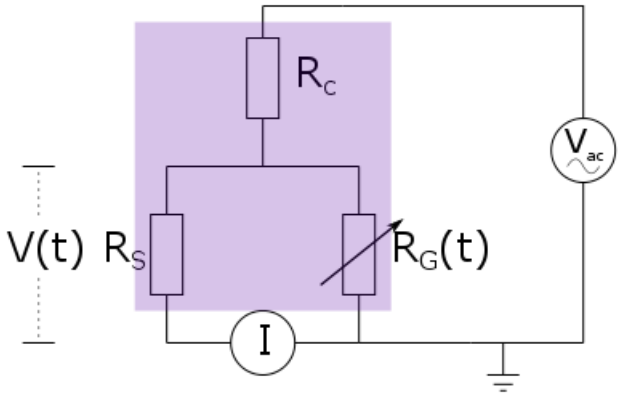

Figure 6.2: The simplest circuit diagram used to demonstrate rectified current.

Figure 6.2 shows the circuit of a device that can generate I_R. In the shaded region, circuit elements are intrinsic to the device and not part of the measurement setup. Respectively, R_S and R_C are the source and gate resistances, and R_G is the variable drain resistance. Current is driven throughout the circuit by an applied AC voltage to the gate

$$V_{ac}(t) = V_{ac}\sin(2\pi f t). \tag{6.1}$$

During the first half of the cycle, when the gate voltage is positive, electrons are pulled up through both R_S and R_G. During the second half, when the gate voltage is negative, R_G changes, and different numbers of electrons push down through R_S and R_G. The ratio of R_S to R_G determines how much current flows through R_S in each part of the cycle. The rectified current, I_R, is the net charge transferred through the electrometer in one AC cycle divided by the time of one AC cycle, given by

$$I_R = f \int_0^{1/f} I(t)\,\mathrm{dt} \tag{6.2}$$

where $I(t)$ is the instantaneous current through the electrometer and f is the AC voltage frequency. From Ohm's law

$$I(t) = \frac{V(t)}{R_S} \tag{6.3}$$

where $V(t)$ is the voltage across the resistor in series with the electrometer, R_S. From the circuit in Figure 6.2, we find a relationship between $V(t)$ and the applied voltage $V_{ac}(t)$

$$V(t) = \frac{R_{S+G}(t)}{R_{S+G}(t) + R_C} V_{ac}(t). \tag{6.4}$$

where $R_{S+G}(t)$ is the total resistance of R_S and $R_G(t)$ in parallel

$$R_{S+G}(t) = \frac{R_S R_G(t)}{R_S + R_G(t)}. \tag{6.5}$$

Substituting equations (6.1), (6.3), (6.4), and (6.5) into (6.2) gives

$$I_R = \frac{f V_{ac}}{R_S} \int_0^{1/f} \left(1 + \frac{R_C(R_S + R_G(t))}{R_S R_G}\right)^{-1} \sin(2\pi f t)\, \mathrm{dt}. \tag{6.6}$$

There will be a non-zero rectified current as long as $\left(1 + \frac{R_C(R_S+R_G(t))}{R_S R_G}\right)^{-1}$ is asymmetric about $t = 1/2f$.

Figure 6.3 shows the steps required to calculate I_R from a conductance plot at a chosen gate voltage, V_{g0}. Figure 6.3a shows a conductance plot of V_G with no AC signal applied. Figure 6.3b shows the conductance at $V_g = V_{g0} + V_{ac}(t)$ over one cycle. Figure 6.3c shows the instantaneous current over the cycle, calculated from the integrand of equation 6.6 and later from equation 6.10. Finally, Figure 6.3d shows I_R, which is the integral of the instantaneous current over one cycle times f, plotted for each value of V_{g0}.

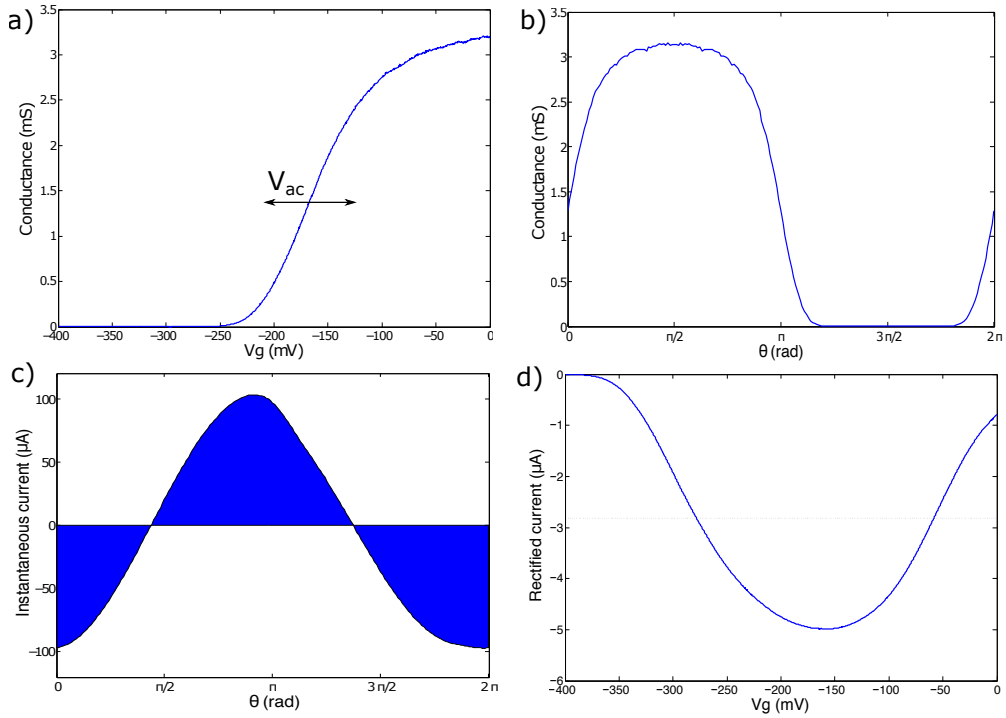

Figure 6.3: (a) Conductance vs. gate voltage. (b) Conductance throughout the AC cycle based on values from (a) with $V_{g0} = -170\text{mV}$ and $V_{ac} = 80\text{mV}$. (c) Instantaneous current throughout the AC cycle based on conductance values from (b). (d) Total modelled rectified current as a function of gate voltage.

This model is sufficient to show roughly the correct level of rectified current as a function of gate voltage, given the choice of R_C; but it does not have the correct frequency response, and it does not describe the device well. In the real device the gate is not leaky; instead the gate forms a capacitor with the 2DEG. To make the model more realistic we introduce a new circuit that includes the capacitor formed between the gate and the 2DEG.

6.2.2 Full circuit

Figure 6.4 shows the circuit with the capacitor included. In the circuit diagram, a capacitor, with capacitive reactance $X_C = i/(2\pi fC)$, replaces the resistor R_C in Figure 6.2. The change in $R_G(t)$ is due to the field effect. When the gate voltage

is positive, electrons are pulled up to charge the capacitor through both R_S and R_D. However, when the gate voltage is negative, an additional process occurs. The channel becomes more pinched-off under the gate, (R_G becomes larger). This splits the capacitor into a pair of parallel capacitors, one from the gate to the source and the other from the gate to the drain. As the capacitors are formed by a symmetric bar gate, we assume that they have equal capacitance.

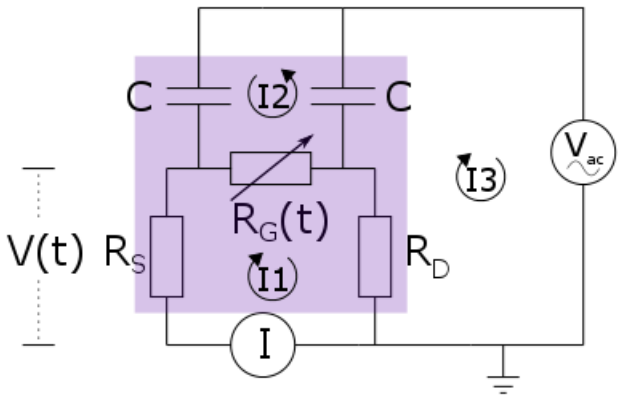

Figure 6.4: The circuit used to model rectified current in this work.

This is a non-reducible circuit. Accordingly, we use Kirchoff's current loop method to solve for I_1. The equations are given by:

$$-I_1 R_D + I_2 X_C + I_3(R_D + X_C) = V_{ac}(t) \tag{6.7}$$

$$I_1(R_S + R_D + R_G(t)) + I_2 R_G(t) - I_3 R_D = 0 \tag{6.8}$$

$$I_1 R_G(t) + I_2(R_G(t) + 2X_C) + I_3 X_C = 0 \tag{6.9}$$

Solving for I_1

$$I_1(t) = \left(\frac{2X_C R_D + X_C R_G(t) - R_D R_G(t)}{X_C^2(R_D + R_S + R_G(t)) + X_C(R_D R_G(t) + 2R_D R_S + R_S R_G(t)) + R_D R_S R_G(t)} \right) V_{ac}(t). \tag{6.10}$$

Because the reactive capacitance causes the current to lag behind the voltage, it introduces a phase shift to $V_{ac}(t)$. The easiest way to solve this is to let $V_{ac}(t) = V_{ac}e^{i(2\pi ft)}$ and take the imaginary part of $I_1(t)$.

$$I_R = fV_{ac}\int_0^{1/f} \mathrm{Im}\left[\left(\frac{2X_C R_D + X_C R_G(t) - R_D R_G(t)}{X_C^2(R_D + R_S + R_G(t)) + X_C(R_D R_G(t) + 2R_D R_S + R_S R_G(t)) + R_D R_S R_G(t)}\right)e^{i(2\pi ft)}\right]\mathrm{dt}. \tag{6.11}$$

In order to test this model and see if we can make predictions about the behaviour of I_R, we explore the parameters of V_{ac}, f, R_S, and R_D and compare simulations to experimentally measured values.

6.3 Device

To study the effect of changing these parameters on rectified current, we produced a set of devices that included the elements required to observe rectified current, whilst remaining as simple as possible to facilitate analysis of the data. These devices are as close as possible to the circuit diagram in Figure 6.4. As the circuit has no gate filters, the device would have no protection from voltage spikes and would be prone to blowing up. To address this we used a gated bar device with no narrow-etched channel. We used a V81 GaAs/AlGaAs HEMT with a wide-etched channel and 3 finger gates, (Figure 6.5). The optically defined mesa etch is shown in green and the optically defined gates are shown in red. We used only the middle gate, and took all measurements in a helium dewar at 4.2 K.

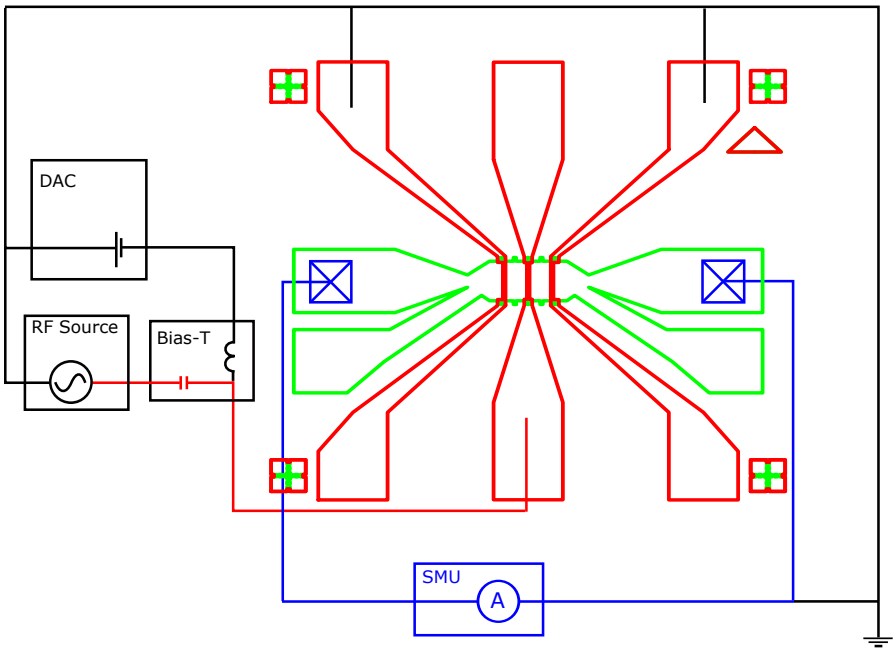

Figure 6.5: Schematic of the measurement setup with the rectified current device. The mesa is outlined in green and gates in red. Only the middle gate is used.

We first measured R_G by taking pinch-off curves of the central gate at source-drain biases of -1 mV, 0, and 1 mV (Figure 6.6). Theoretically, at 0 bias, no current is generated. However, we observed approximately $-0.6\,\mu$A, so we inferred that there was already a rectified current present, probably due to a parasitic radio pick up. As the rectified current is the same for all source-drain biases, we correct for it by subtracting the 0 bias pinch-off curve from the 1 mV bias pinch-off curve. This corrected pinch-off is checked by comparing it to two other corrected currents: subtracting the -1 mV pinch-off from the 0 bias pinch-off, and subtracting the -1 mV pinch-off from the 1 mV pinch-off and dividing by 2. All three pinch-off curves agree well, (blue line in Figure 6.6). To get R_G as a function of V_g the corrected current is divided by the source-drain voltage, 1 mV.

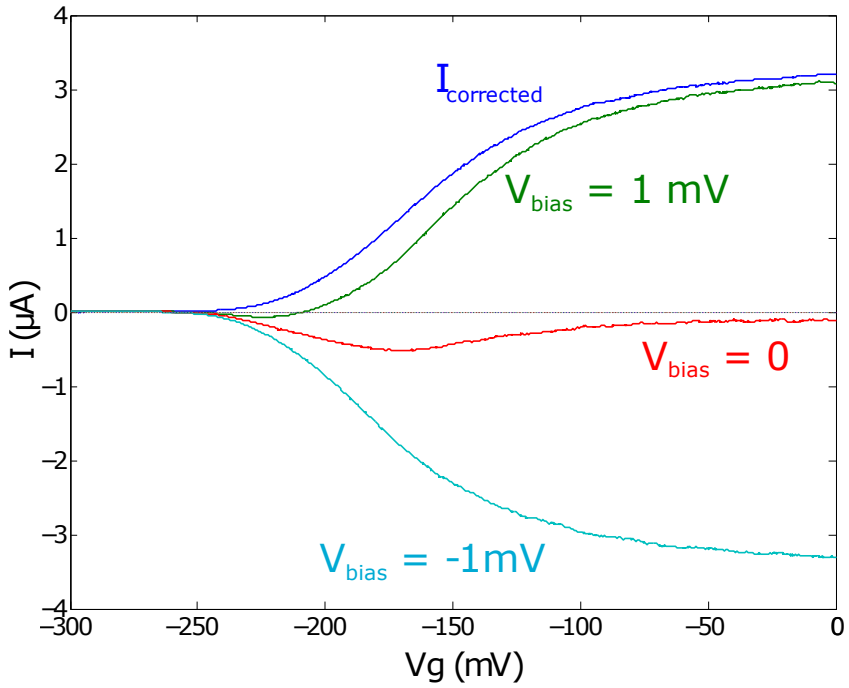

Figure 6.6: Pinch-off curves of the central gate with a source drain bias of -1 mV (light blue), 0 (red), 1 mV (green), and a corrected pinch-off curve (dark blue).

6.4 Amplitude dependence

We measured I_R against gate voltage for RF amplitudes between 20 mV and 200 mV, and compared it to a simulation of I_R from the model. We chose a frequency of 0.1 GHz as it is a common frequency in pump operation, and took measurements at 0 source-drain voltage bias. Figure 6.7a shows the measured data for RF amplitudes between 20 mV (blue line) and 200 mV (red line) in steps of 20 mV. The yellow circles highlight the pinch-off voltages of I_R, and the red oval highlights some irregularities seen at higher RF amplitude. Figure 6.7b shows the simulated I_R from the model. The measured data (Figure 6.7a) and the model (Figure 6.7b) share three features:

1. I_R increases linearly with amplitude.

   This is expected from equation (6.11), as $I_R \propto V_{ac}$.

2. The pinch-off shifts by the amount the amplitude changes.

The rectified current pinch-off is the gate voltage at which the channel stops conducting, (yellow circles in Figure 6.7a). This is modelled as the pinch-off when no AC is applied, (pinch-off gate voltage from Figure 6.6), plus a shift that is given by V_{ac}. This is because V_{ac} determines the variation in $R_G(t)$. For small V_{ac}, the contributions to $R_G(t)$ from the positive and negative parts of the AC cycle are similar, but for large V_{ac}, the contributions are not. $R_G(t)$ is made up of contributions from a pinched-off or open-channel resistance from the positive and negative part of the cycle, which alters the line shape. If $R_G(t)$ is constant, then from equation (6.11), $I_R = 0$. The rectified current pinch-off voltage will occur when V_g is negative enough such that $R_G(t) \to \infty$ for all V_g between $V_g - V_{ac}$ and $V_g + V_{ac}$. For an increase in V_{ac} of 20 mV (RMS), the rectified current pinch-off shifts by $20\sqrt{2}$ mV. The modelled current (Figure 6.7b) used $R_S = R_D = 500\ \Omega$, and $C = 1.2$ pF.

3. The line shape does not change significantly for small amplitudes ($V_{ac} <$ 180 mV).

   The shape of the rectified current vs. voltage plots are similar until $V_{ac} \approx$ 180 mV, at which point a second peak develops, (red oval in Figure 6.7a). These may be due to measurement errors at higher amplitudes and are thus not included as part of the model.

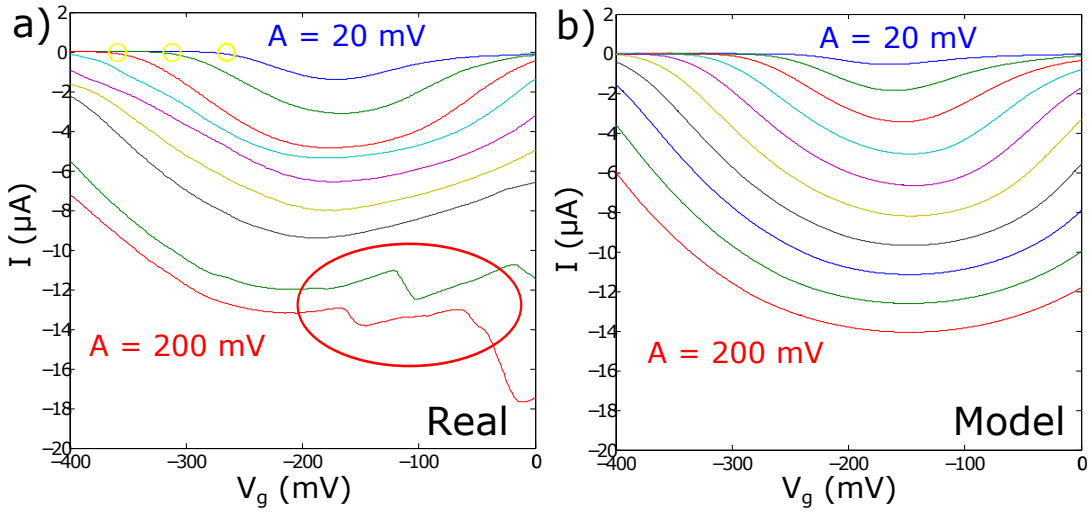

Figure 6.7: (a) Rectified current vs. Amplitude in steps of 20 mV. (b) Simulated data using equation (6.11).

In section 6.5, we demonstrate that I_R depends heavily on frequency. However, the linearity between I_R and V_{ac} remains independent of frequency, (Figure 6.10b).

6.4.1 Importance to pump current

Under certain conditions I_R will swamp quantised current, I_P; by identifying and addressing those conditions, we can attempt to suppress I_R, thus allowing I_P to be measured. We compare the effect that changing amplitude has on I_R and I_P. The pinch-off gate voltage of I_R and I_P shift differently as amplitude increases. The I_R pinch-off gate voltage is pushed out to more negative values indefinitely. In contrast, with respect to I_P, the pinch-off gate voltage gets pushed out to more negative values until no dot is formed, and further increasing amplitude does not change that pinch-off. Accordingly, increasing amplitude increases I_R vastly more than it does I_P. Therefore, the optimal amplitude to observe quantised pumped current is the amplitude at which the pumped current stops increasing.

6.5 Frequency dependence

Figure 6.8 shows the frequency dependence of the absolute magnitude of the rectified current (blue) from $f = 0 \rightarrow 4$ GHz, with V_{G0} and A held constant, ($V_{G0} = -150$ mV and $A = 100$ mV). The absolute magnitude is used because I_R rapidly switches in polarity in the experimental data as the frequency is swept. These polarity switches may be caused by interference effects between the applied AC voltage and radio pickup, or by changes in the differential capacitance throughout the cycle. As such, they are exogenous to the model. While we cannot model the rapid oscillations, we can model the envelope of the frequency response over a large frequency range. $|I_R|$ appears to increase until 0.5 GHz then decrease to zero according to some power law. This decrease in $|I_R|$ is unlikely to be attributed to attenuation in the RF lines, as the attenuation changes by only -5 dBm (from about 63 mV to 29 mV for the 70.7 mV RF signal used) over the entire frequency range. Figure 6.9 shows the linear attenuation of the probe plotted vs. frequency. From section 6.4, $|I_R|$ decreases roughly linearly with RF amplitude, which suggests that the decrease in $|I_R|$ with frequency is not due to the probe attenuation. Instead, we attribute the decrease in $|I_R|$ to the frequency dependence of the capacitive reactance of the gate.

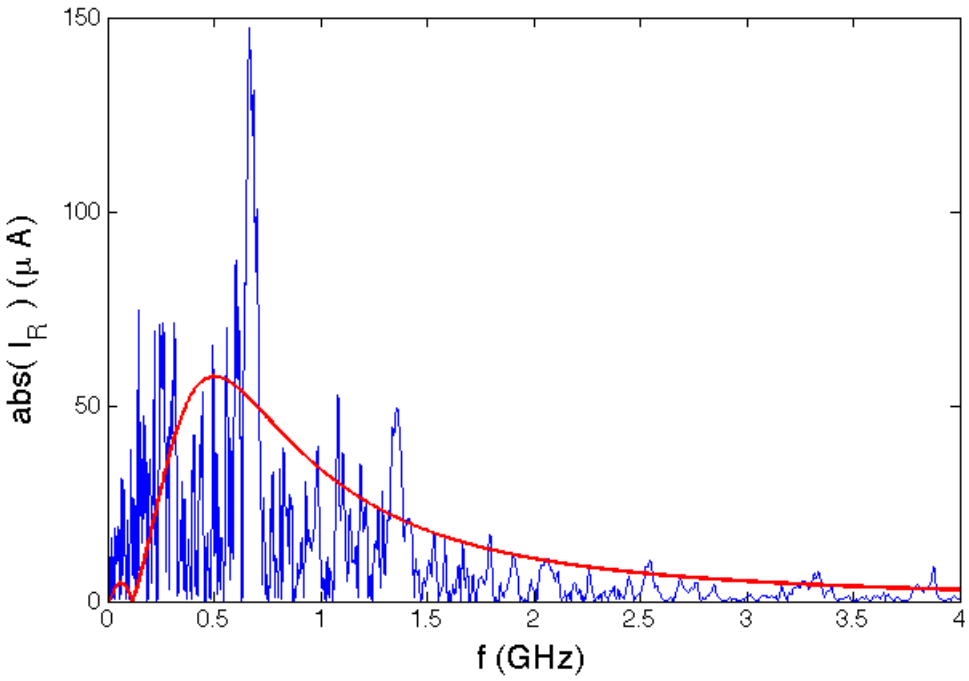

Figure 6.8: Absolute value of the rectified current vs. frequency of the measured current (blue) and the simulated current (red).

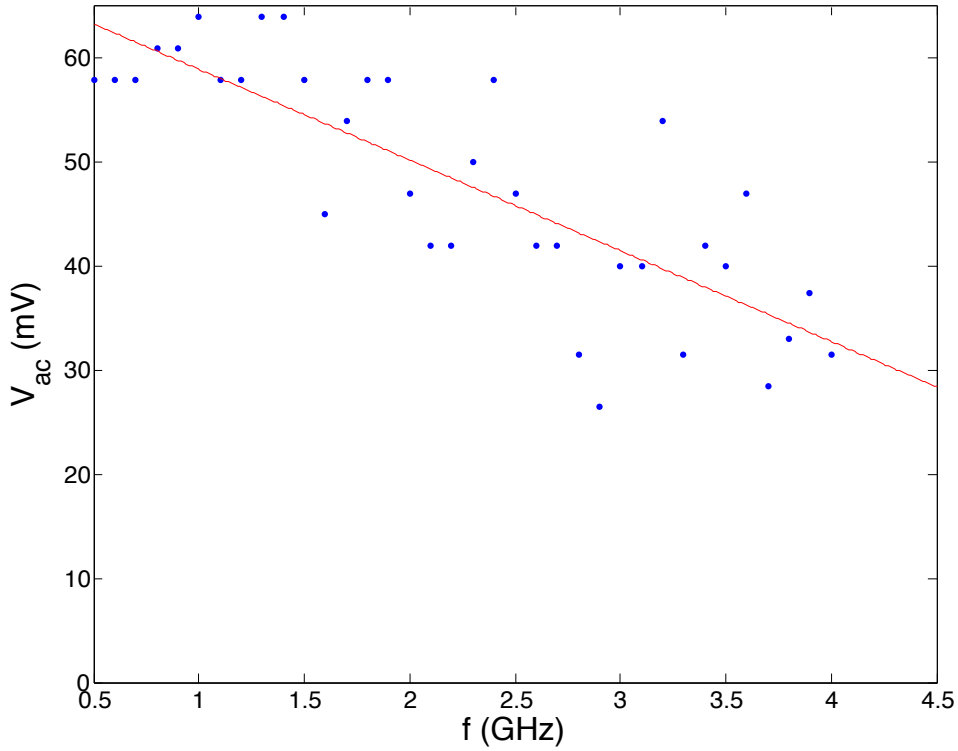

Figure 6.9: Plot of the RF line attenuation vs. frequency for a 70.7 mV input signal.

At lower frequencies the capacitive reactance term, X_C^2, dominates, making I_R small. As the frequency is increased, X_C is reduced and becomes similar to the resistance terms, making I_R increase. When the frequency becomes very large, X_C is further reduced to approach 0, at which point $I_R = 0$.

Substituting $X_C \to 0$ into equation 6.11 gives

$$I_R = fV_{ac} \int_0^{1/f} \left(\frac{-R_D R_G(t)}{R_D R_S R_G(t)} \right) \sin(2\pi f t)\ \mathrm{dt} = 0. \tag{6.12}$$

If the source and drain resistances are known, the capacitance of the gate/2DEG can be approximated. We estimated the I_R using an RF amplitude of 100 mV, a source and drain resistance of 700 Ω, and $C = 1.2$ pF.

6.5.1 Importance to pump current

To investigate if rectified current will swamp any quantised pumped current, we measured I_R in the far pinch off regime, where we expect to see pump current, against frequency. Figure 6.10a shows a colourmap of I_R vs. gate voltage and frequency. Respectively, Figures 6.10c and 6.10d are I_R vs. frequency cross-sections of the colourmap at $V_G = -300$ mV and $V_G = -150$ mV. As the gate is swept from -150 mV to -300 mV, I_R drops from several μA to several nA. However, even at such a low value, it still swamps the pA I_P. While it might be possible to detect pumped current at specific frequencies, it would not be possible to do frequency dependent measurements as the rectified current will not be suppressed for certain frequencies. It might be possible to suppress rectified current by pumping at very high frequencies, but this would be at the expense of pump accuracy, which decreases as the frequency is increased. Accordingly, such pumping is not a serious candidate towards accurately measuring and observing pumped current.

The frequency dependence, while containing seemingly random polarity switches, is very reproducible. Figure 6.10b shows a high resolution frequency sweep at $V_G = -150$ mV. The 40 mV sweep (blue) is very similar to Figure 6.10d, despite the difference in how the data was taken. Figure 6.10b was a single sweep in frequency, while Figure 6.10d comprised I_R at $V_G = -150$ mV for many sweeps in V_G. In addition, the 20 mV sweep (green) is similar to the 40 mV sweep (blue) but with half the rectified current, which is expected on the basis of the reasoning in section 6.4.

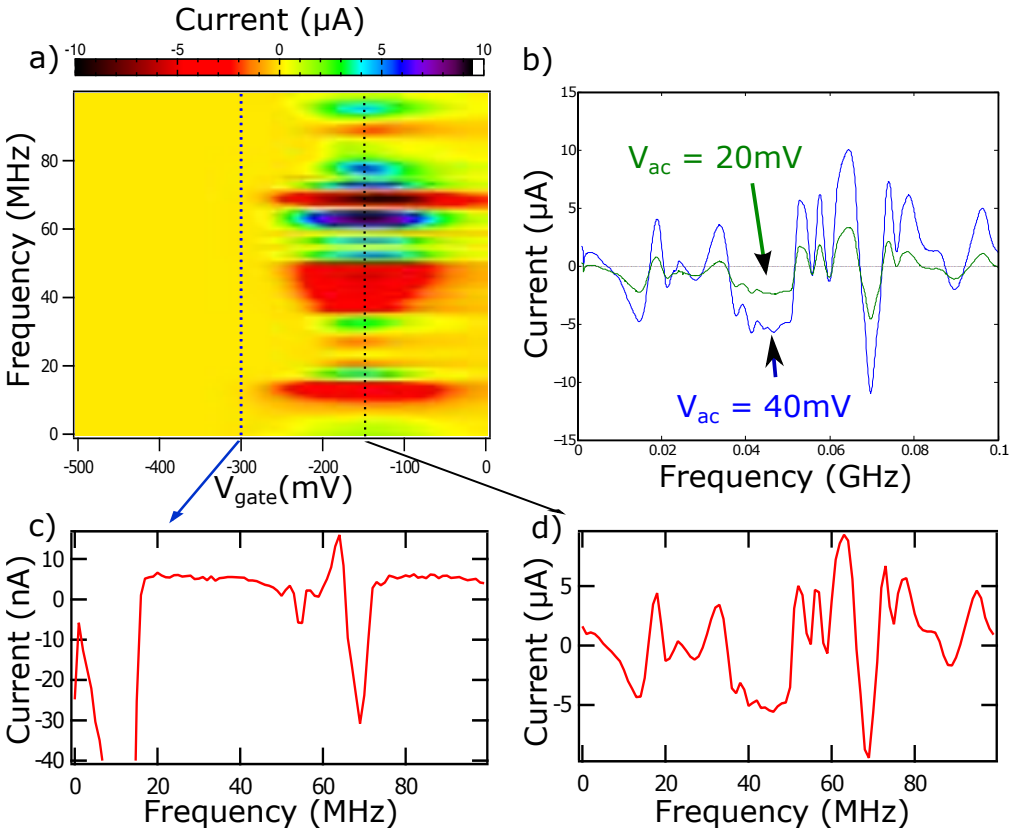

Figure 6.10: (a) Rectified current as a colourmap vs. frequency and gate voltage. Respectively, (c) and (d) are cross sections of the map at a voltage in the pinch off regime and at a voltage that gives the highest current. (b) A high resolution plot of (d) at different amplitudes.

6.6 Resistance dependence

To investigate the resistance dependence of I_R we added variable resistors in series with the source and drain to our measurement setup, which allowed us to vary R_S and R_D, (Figure 6.11).

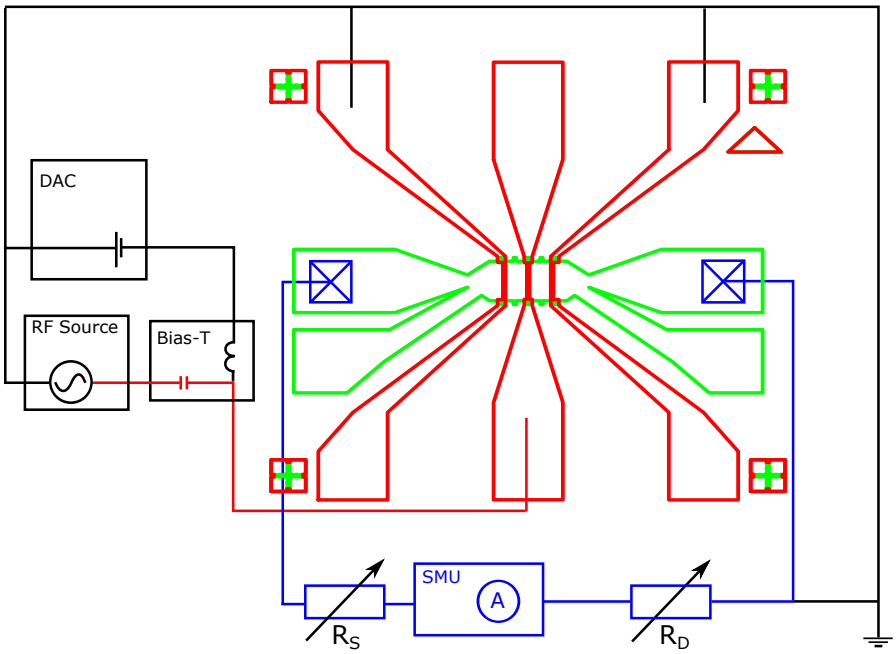

Figure 6.11: A schematic of the circuit sowing the locations of R_S and R_D on the Ohmic lines.

We measured I_R as a function of R_S and R_D, with $V_{G0} = -140$ mV, $V_{ac} = 80$ mV, and $f = 0.1$ GHz. We stepped the resistances between 0 and 20 kΩ in steps of 1 kΩ. Figure 6.12a shows I_R decreases when R_S and R_D are increased. Figure 6.12b shows the simulated data from the model. Figures 6.12a and 6.12b are plotted on different I_R scales to show that, for small resistances less than a few kΩ, I_R increases to different values; both increase according to a similar power law. The resistance dependence of the simulation would fit the measured data if multiplied by a factor of 3. For large resistances, the simulation matches the measured data well, without the need for a spurious multiplying factor. The measured data shows R_S and R_D affect current equally, while the simulation shows current affected more by R_S. However, the general dependence of I_R on R_S and R_D in the simulation is similar to that found in the measured data; this helps us understand the mechanism by which I_R can be suppressed.

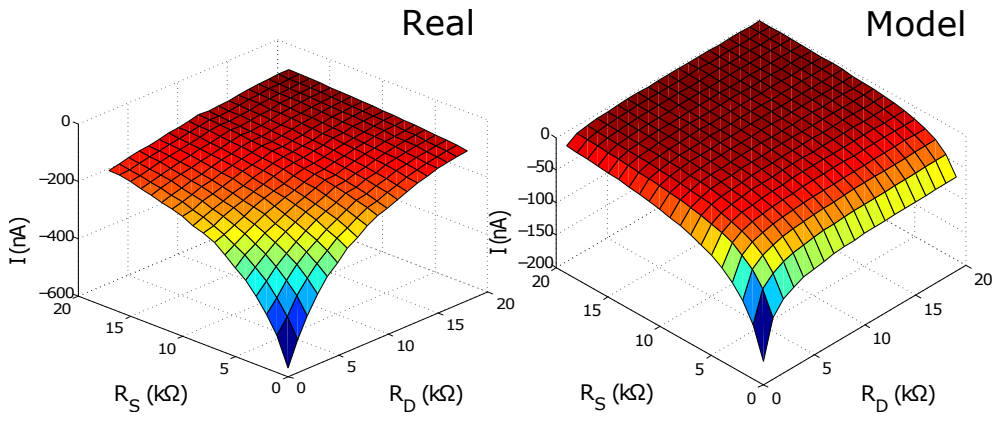

Figure 6.12: 3D plots of the resistance dependence of measured rectified current (a) and modelled values (b).

6.6.1 Importance for pumped current

Varying the resistance values, R_S and R_D in the circuit diagram, does not impact pumped current. Pumped current is independent of any resistors put in series with the source and drain, and rectified current is heavily suppressed by such resistors. This makes adding series resistors a promising candidate to suppress rectified current, while leaving quantised pump current unchanged. When 20 kΩ resistors are used, I_R is suppressed by 2 orders of magnitude, which may be sufficient to reveal pump current. We have identified, based on the model, what factors can be used to suppress I_R and the extent to which they may be adequately used. However, adding series resistance alone was not sufficient to reveal I_P. Adding filters to the circuit is required to reveal I_P, after which adding additional series resistance further helps to reveal I_P, as predicted by the model.

6.7 Exogenous factors

While the model we have developed captures the main internal factors that impact I_R, external factors may also impact I_R. To test possible factors for revealing pump current, we used the device and measurement setup described in section

5.4, which can generate pump current. Measurements in this section were done on a 1.5 K Teslatron cryostat in the LCN.

6.7.1 Ohmic filters

One external factor that may help suppress I_R is the addition of a low-pass filter on the Ohmic line, which was suggested by Dr. James Nicholls. Filters are not generally used on Ohmic lines as they can alter signal of an AC measurement. However, they should not affect DC measurements, which we perform on electron pump experiments. Figure 6.13 shows a pump map of a narrow-etched channel device that still exhibits a large rectified current. Adding a low-pass filter (Figure 6.13b) suppressed the current sufficiently to reveal two pump plateaus, and complementing the filter by increasing the source resistance (Figure 6.13d) revealed an additional third plateau. Interestingly, increasing the drain resistance (Figure 6.13c) added a lot of noise to the signal. Figure 6.14 shows line scans of Figure 6.13 at $V_{\text{entrance}} = -700\,\text{mV}$ and more clearly shows the large suppression of I_R when the filter is added. We conclude that I_R is suppressed more with a low-pass filter than with a resistor in series. We attribute this to a capacitor being able to store charge better than a resistor can dissipate it.

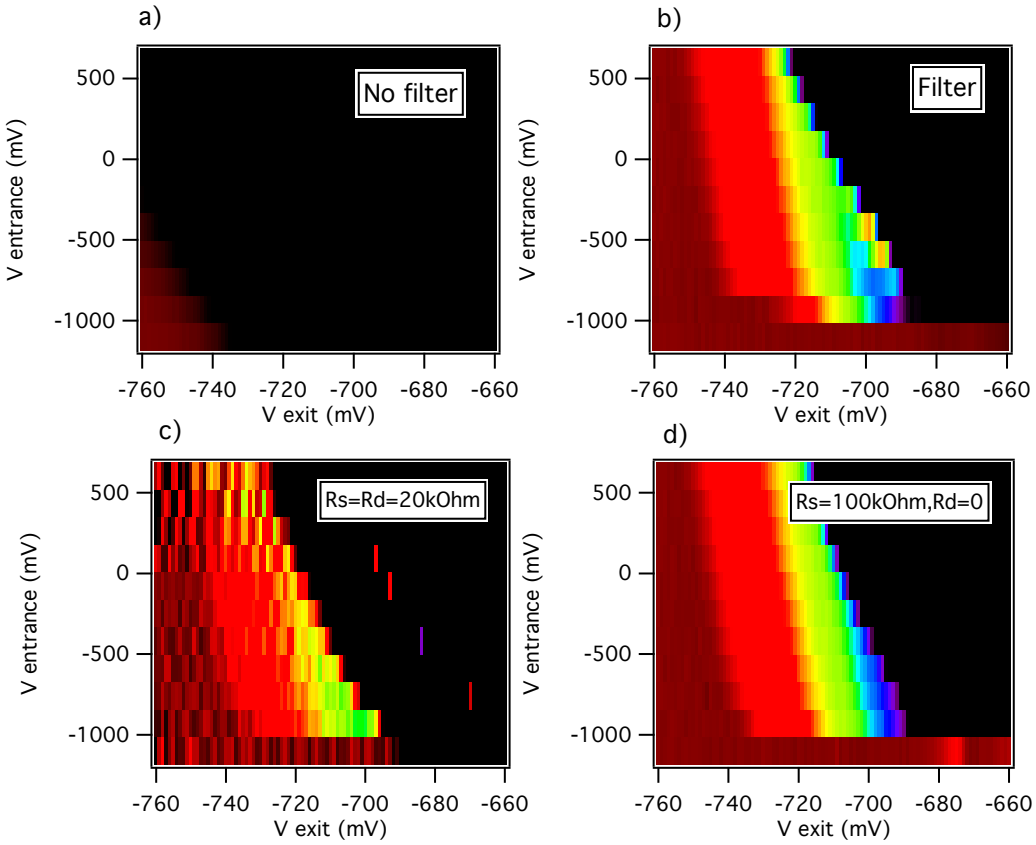

Figure 6.13: (a) Colourmap of $I_P + I_R$ vs. entrance and exit gate voltage with no Ohmic filter, (b) with an Ohmic filter, which revealed 2 quantised pump plateaus. (c) $I_P + I_R$ with an Ohmic filter and increased R_S and R_D, which made the signal noisy. (d) $I_P + I_R$ with an Ohmic filter and increased R_S only, which revealed a third plateau.

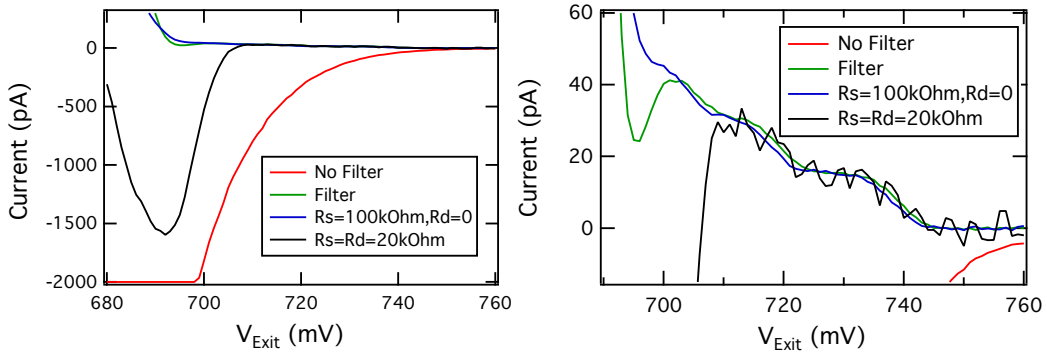

Figure 6.14: Line scans of Figure 6.13 showing the suppression of I_R to reveal I_P when an Ohmic filter is added and R_S is increased.

6.7.2 Magnetic field dependence

Devices with multiple gates show more complicated rectified current line-shapes than the single peak for the device with a single gate. Figure 6.15 shows I_R of a split gate pump in a magnetic field of $B = 0$ T (pink) to $B = 1.5$ T (black) in steps of 0.25 T. The I_R of the split gate pump shows two peaks, which are suppressed when B is increased. We measured the suppression of one of the peaks for both positive and negative B and found the suppression to be the same. This differs from I_P, which improves for one polarity of B and degrades for the other. This makes magnetic fields, which are already used to increase I_P accuracy, a promising candidate for revealing I_P in devices where I_R is significant.

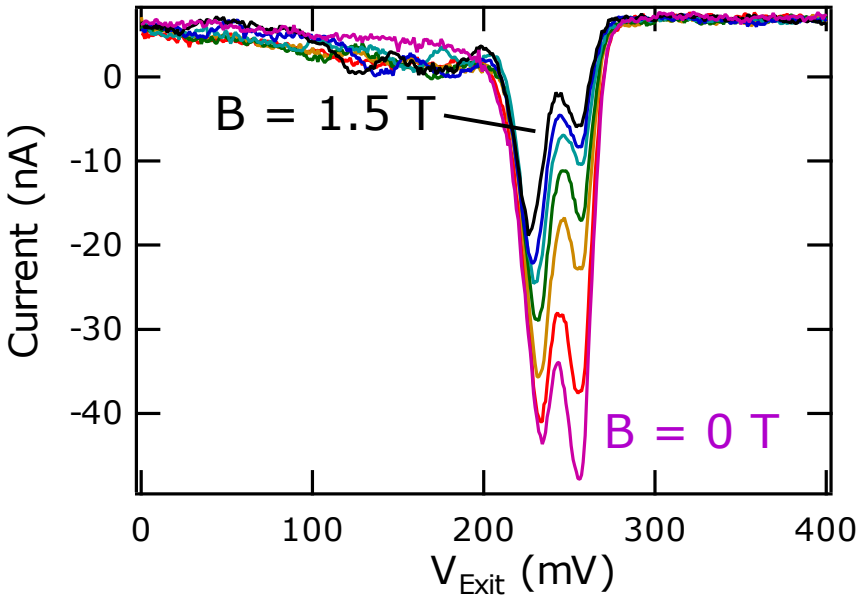

Figure 6.15: Plots of I_R vs. V_{Exit} in a magnetic field of $B = 0$ T (pink) to $B = 1.5$ T (black).

6.8 Summary

We developed a model for rectified current based on the asymmetry of the instantaneous current flowing through the electrometer during different halves of

the AC cycle. Using the model we generated simulations of rectified current and its dependence on amplitude, frequency, and resistance. When we use realistic capacitance and resistance values, the simulated data shows a dependency that closely matches the measured data. When amplitude is increased, I_R and the pinch-off gate voltage increase, with similar line shapes. At higher amplitudes, more features appear in the measured data, but they are likely due to the measurement setup. The model explains the initial increase and subsequent decrease of I_R with increased frequency. Again, the simulation changes similarly to the envelope of the measured data when frequency is increased. However, there are many sharp changes in the polarity of the measured current that are not explained by the model. Finally, the model explains the reduction in I_R with increased series resistance. There are some notable differences between the measured data and the simulation: with respect to R_S and R_D, the measured data is much more symmetric than the simulated data. However, in the context of small amplitudes, wide frequency spectra, and high resistances, the model explains the measured data well and provides useful insight into the origin of the rectified current and solutions to suppressing it.

We investigated which of the parameters could be used to suppress rectified current, if external factors could achieve the same effect, and what contributes to the rectified current being suppressed in narrow-etched channel devices. The narrow-etch channel isolates the RF gate from the 2DEG except in the channel. This changes many physical parameters in our model: $R_G(t)$, R_S, R_D, and C. In a narrow-etch device, $R_G(t)$ is less symmetric, and R_S and R_D are greater. These factors likely contribute to the suppression of I_R in a narrow-etch device. Of the parameters investigated that could allow us to relax the processing step of the narrow-etch channel, only series resistance can be used as a means of suppressing I_R without affecting pump current, but it is unlikely to do so sufficiently to reveal pump plateaus. However, adding a low-pass Ohmic line filter had a greater effect than changing any of the above parameters, the inclusion of which revealed pump plateaus in a device where rectified current otherwise dominated, shown in section 6.7.1. Finally, we note that applying a perpendicular magnetic field to a pump suppressed I_R. We look to expand the model to accommodate this as part of our future work.

6.9 Future work

While we have investigated rectified current for 3 parameters, further study is needed to form a model that will be more directly applicable to pump devices, rather than single gate devices, by doing the following:

1. Investigate further our magnetic field dependent measurements on the single gate devices.

2. Investigate further the effects of having an additional gate in close proximity to the oscillating gate.

   The I_R dependence on R_S and R_D is symmetric for a single gate device, but not for a multi-gated device. In a device with a pump, increasing R_S suppresses I_R, but increasing R_D increases I_R and makes the signal much more noisy.

3. Investigate the source of the sharp polarity changes in frequency.

   If we can make a measurement setup where there is no rectified current when no AC signal is applied to the gate (no radio pick-up), we can investigate applying arbitrary waveforms to the gate to simulate the interference effects of radio pick up and the applied RF signal.

4. Introduce other electrical components.

   While an Ohmic filter suppresses I_R, the same may be true for gate filters, which are usually used to protect the device from spikes. Previous experiments used SMUs with a remote preamp and rectified current was not detected, though it was not attributed to the preamp. If BNC cables act as antenna for radio pick-up or generate AC current through the tribo-electric effect, where mechanical building vibrations bend the BNC cables creating friction between the outer and inner sheaths of the cable. A remote preamp mounted near the breakout box should help in suppressing I_R.

5. Investigate further the effects of changing capacitance.

   The model presented only includes a simulation using a constant capacitance, but in a real device the capacitance changes throughout the AC

cycle, because the field effect changes the effective distance between the gates and the active region of 2DEG. We experimented with modifying our model to include a changing capacitance, and found that the behaviour of rectified current changed drastically but unpredictably, especially if the differential capacitance is not constant, making capacitance a likely candidate for explaining the differences between the real and measured currents.

Chapter 7

Model

7.1 Introduction

In section 1.3 we gave a basic description of the pumping mechanism and pump map. In section 2.11, we described the universal decay cascade model (UDC), developed by Kashcheyevs [61], which, while mathematically rigorous, uses a holistic approach to explaining error mechanisms, and is too complicated to carry the pertinent physical variables through to the final equation used to fit the data. This results in a model that mathematically describes the data well, but makes it hard to find physical meaning in its equations. Also, while the UDC model was developed with the intention of explaining the pump plateaus, it does not explain the differences in current in different parts of the pump map. In this chapter we explore the effects of changing RF amplitude, temperature, and RF frequency on the plateaus at different parts of the pump map, with a view to better understanding the pumping mechanisms, and develop a model from first principles to explain them. As a consequence of this new approach to understanding the pump maps as well as the plateaus, we are able to suggest the best regions of the pump map to look in order to find the flattest plateaus. This is highly important for ongoing investigations to realise the current standard using quantum pump, as mentioned in section 1.2.

This chapter has 5 main sections: First, as there are no standard definitions in

the literature, we introduce our nomenclature. Second, we present the data showing the amplitude, temperature, and frequency dependence of the pump maps. Third, we develop a simple theoretical model for the pump plateaus based on time dependent tunnelling rates of individual electrons in and out of the dot. Our model makes critical simplifying assumptions that allow the control parameters (amplitude, temperature, and frequency) to be carried through to the final equation. Fourth, we use our model to explain the observed effects in sections 7.3, 7.4, and 7.5. Finally, we identify future work aimed at improving our model and extending the pump map data.

7.2 Navigating the pump map

Although many papers have described pump maps with various nomenclatures, in order to discuss the effects of temperature, frequency, and amplitude on pump current efficiently, we consider it is appropriate to develop a new nomenclature for the various lines and nodes in the pump map.

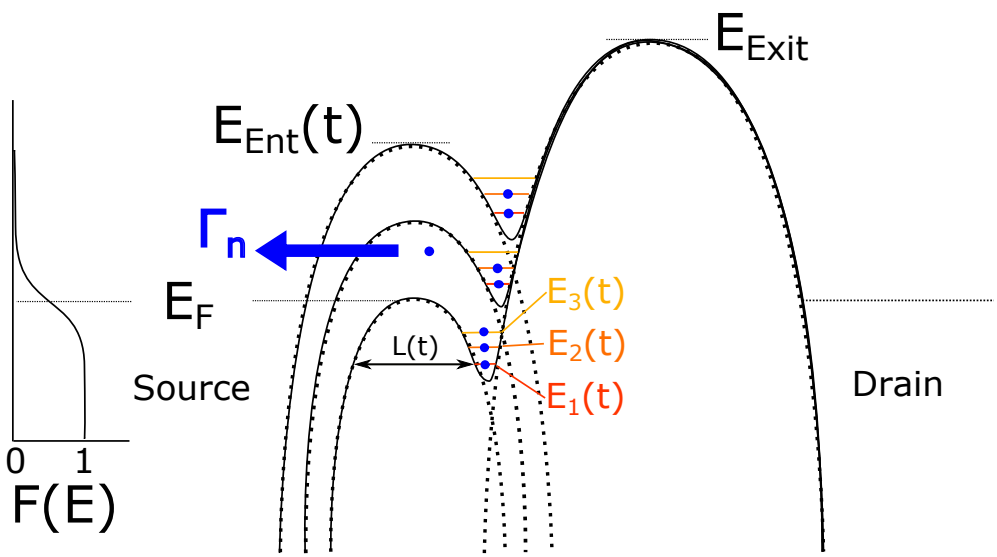

Figure 7.1: A schematic of the pump dot during the pumping cycle. The dotted black lines represent the potentials of the individual gates while the solid black lines represent the potential due to both gates.

Figure 7.1 is a schematic of the pump operation with the relevant energy levels

labelled.

- $E_{\mathrm{Ent}}(\mathrm{t})$ is the energy of the entrance barrier.
- E_{Exit} is the energy of the exit barrier.
- E_{F} is the Fermi energy.
- $E_{\mathrm{n}}(\mathrm{t})$ are the available energy levels in the dot.
- $\Gamma_{\mathrm{n}}(\mathrm{t})$ is the back-tunnelling rate.
- $L_{\mathrm{n}}(\mathrm{t})$ is the width of the entrance barrier and the tunnelling distance for electrons to back-tunnel into the source.

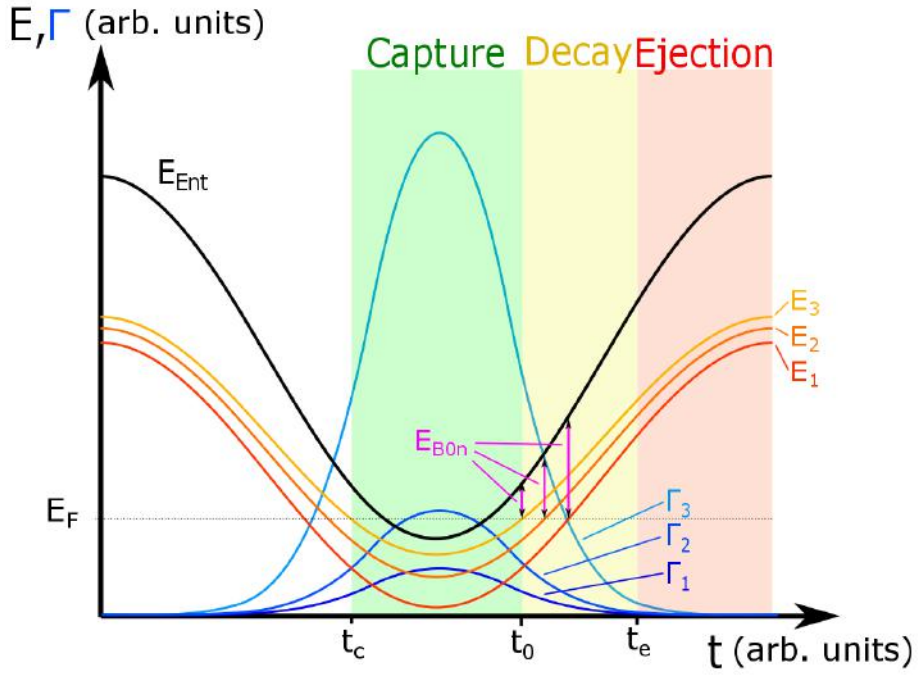

Figure 7.2: A diagram showing the energy levels in a three-level dot (red, orange, and yellow lines), the energy level of the entrance barrier (black line), and the back-tunnelling rates of the electrons in the dot (dark blue, blue, and light blue lines) throughout the pump cycle, which is split into three phases: the capture phase (green), the decay phase (yellow) and the ejection phase (red).

Figure 7.2 shows how $E_{\mathrm{Ent}}(\mathrm{t})$, $E_{\mathrm{n}}(\mathrm{t})$, and $\Gamma_{\mathrm{n}}(\mathrm{t})$ change with time throughout the pump cycle. The back-tunnelling barrier height is the difference in energy between $E_{\mathrm{Ent}}(\mathrm{t})$ and $E_{\mathrm{n}}(\mathrm{t})$. We define E_{B0n} as the back-tunnelling barrier height when the energy level in the dot is equal to the Fermi level,

$$E_{\mathrm{B0n}} = E_{\mathrm{Ent}}(\mathrm{t}_0) - E_{\mathrm{n}}(\mathrm{t}_0) \tag{7.1}$$

Using the nomenclature from Figures 7.1 and 7.2, we describe the pumping operation. The pumping cycle is split into three phases: the capture phase, the decay phase, and the ejection phase, which begin to occur respectively at t_c, t_0, and t_e.

- Capture phase - At the start of a pump cycle, an empty dot is lowered towards the Fermi level, E_F. When E_{n} crosses E_F, at t_c, the dot becomes coupled to the source so electrons can tunnel into it. When the dot starts to rise, electrons are less likely to tunnel into it.

- Decay phase - When the dot rises past the Fermi level, $E_{\mathrm{n}} > E_F$ after time t_0, captured electrons have a higher probability of back-tunnelling into the source. But as the dot rises further, back-tunnelling becomes suppressed.

  The capture and decay phases are considered independent only at T = 0 K. The amount the phases overlap is determined by the thermal broadening of the electrons in the source.

- Ejection phase - Once the probability of back-tunnelling becomes very small, all remaining electrons in the dot are pushed up to E_{Exit} and can tunnel into the drain, contributing to current.

  The decay and ejection phases are considered independent for all temperatures. When E_{Exit} is large compared with $E_{\mathrm{Ent}}(t_{\mathrm{e}})$, tunnelling into the drain is greatly suppressed, so electrons will not be pumped over the barrier when there is still a significant probability that an electron in the dot will back-tunnel into the source. The UDC model and the model in section 7.6 assume pumping in the perfect ejection regime, (i.e. all electrons remaining in the dot at t_e contribute to current), and are based on the back-tunnelling rates of electrons for $t_0 < t < t_e$ only.

Because we have only one measured value, the current, reconciling the potential error mechanisms in each of the three phases becomes challenging. The ejection phase has been studied extensively, notably by the NPL [46]. However, the capture and decay phases have not been studied extensively, and accordingly are not well understood. The UDC model discusses error mechanisms in the decay phase (Figure 7.1), but it is difficult to relate the equations used in the model to the RF amplitude, temperature, and frequency dependence of the pump current, as they are not directly included in the final fitting equation, ($I = ef \sum_n \exp(-e^{-\alpha(V-V_0)+\delta_n}$) from section 2.11). To overcome these limitations, we develop a model that specifically includes these physical parameters in the final fitting equation.

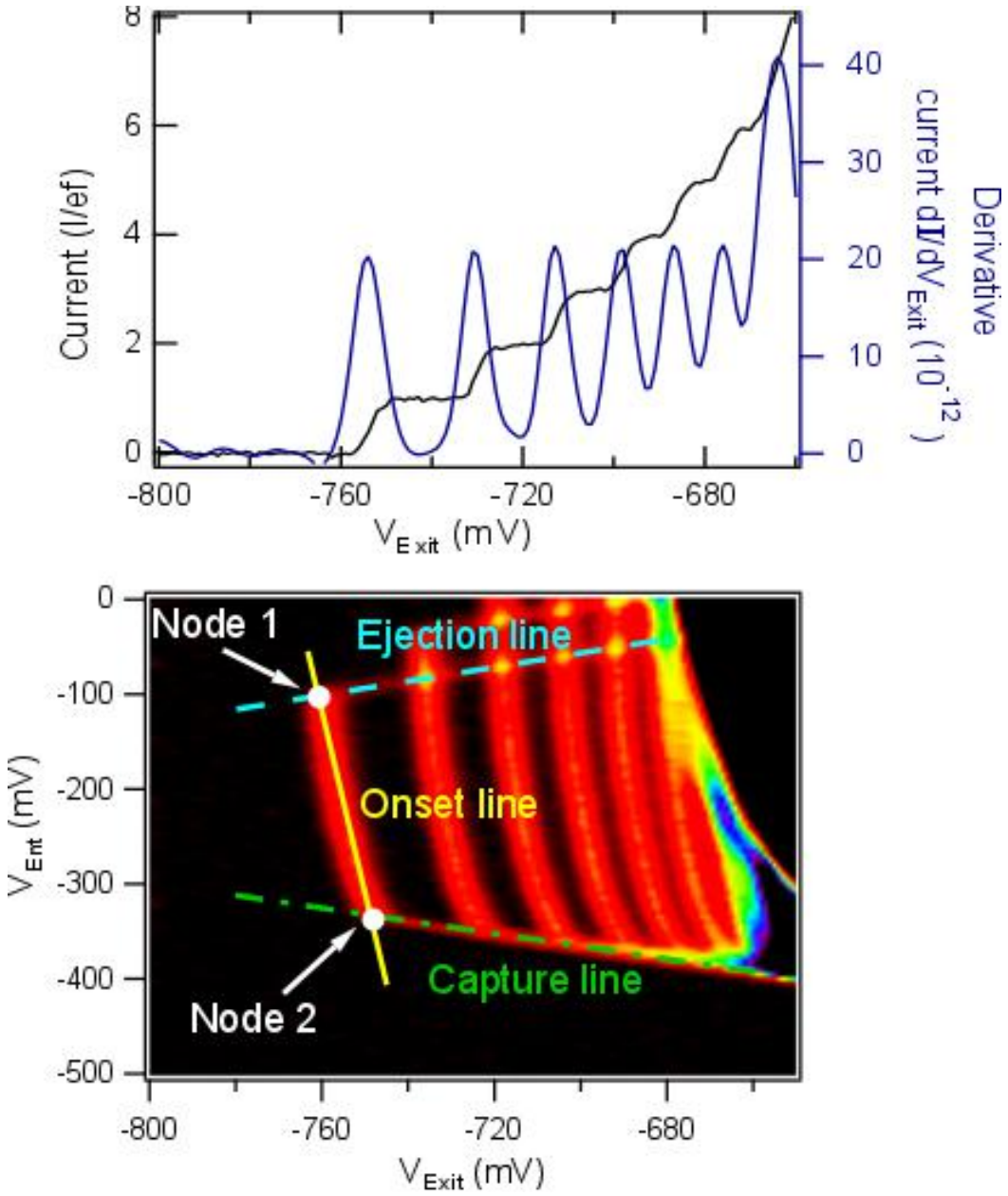

Figure 7.3: Below: A typical derivative pump map, taken at T = 4.2 K and f = 100 MHz, showing the lines and nodes that will be discussed in this chapter The black regions are plateaus and the orange/yellow regions join the plateaus. Above: A line scan of the pump map at V_{Exit} = 200 mV showing the plateaus (black), and the derivative plot (blue).

Figure 7.3 shows a representative pump map. It is a 2D colourmap that displays the differential current as a function of entrance and exit gate voltage. The pump

map can be split into different regions: some where the pumped current is zero and one where the pumped current is quantised and positive, which is bound by the capture, ejection, and the ideal plateau lines. We refer to these lines collectively as the pump map lines.

- The capture line shows a transition, in V_{Ent}, from not pumping electrons to pumping at least one electron. Below the capture line, V_{Ent} is so negative that the dot never dips below the Fermi level during the pump cycle, so electrons are never collected in it.

- The ejection line shows a transition, in V_{Ent}, from pumping n electrons to $\text{n} - 1$ electrons.

  Above the ejection line, V_{Ent} is not negative enough for the dot to be raised above E_{Exit}, so not all of the electrons are able to tunnel into the drain. Only the first ejection line is shown in Figure 7.3 and is discussed in the model, but for completeness there are additional ejection lines that show the transition from pumping $\text{n} - 1$ to $\text{n} - 2$ electrons etc. The spacing of the ejection lines in E_{Ent} gives a measure of the energy spacing in the dot during the ejection phase.

- The pump onset line shows the transition, in V_{Exit}, from not pumping electrons to pumping one electron. The formation of the pump onset line is not well understood. The UDC model and our model present competing reasons:

  - UDC model - To the left of the pump onset line, V_{Exit} is so negative that the back-tunnelling rates are so high that at t_d there are no electrons left in the dot. At t_0, the difference in the back-tunnelling rates between the electrons in the dot is small so they all back-tunnel out in quick succession. This is described in section 2.11.
  - Our model - To the left of the pump onset line, V_{Exit} is so negative that a dot is never formed below the Fermi level. This is discussed in detail in section 7.6.

The differential current is used to better identify the intersections of the capture, ejection, and pump onset lines. Respectively, we label the intersections of the

ejection and pump onset lines, and capture and pump onset lines, as nodes 1 and 2. The nodes are used to measure the positions and slopes of the lines. We present the shifts in these nodes and pump map lines as a function of amplitude, temperature, and frequency.

7.3 Amplitude

We measured the amplitude dependence of pump current using an NPL pump in a liquid helium dewar at 4.2 K. Figure 7.4 shows pump maps at a frequency of 100 MHz for RF peak-to-peak amplitudes at the RF source from 75 mV to 200 mV in 25 mV steps. There is a second pump map at less negative V_{Exit} and V_{Ent}, which is probably due to a small secondary dot forming between the gates. As it does not affect the first and second plateaus of the main pump map, we neglect it in our analysis.

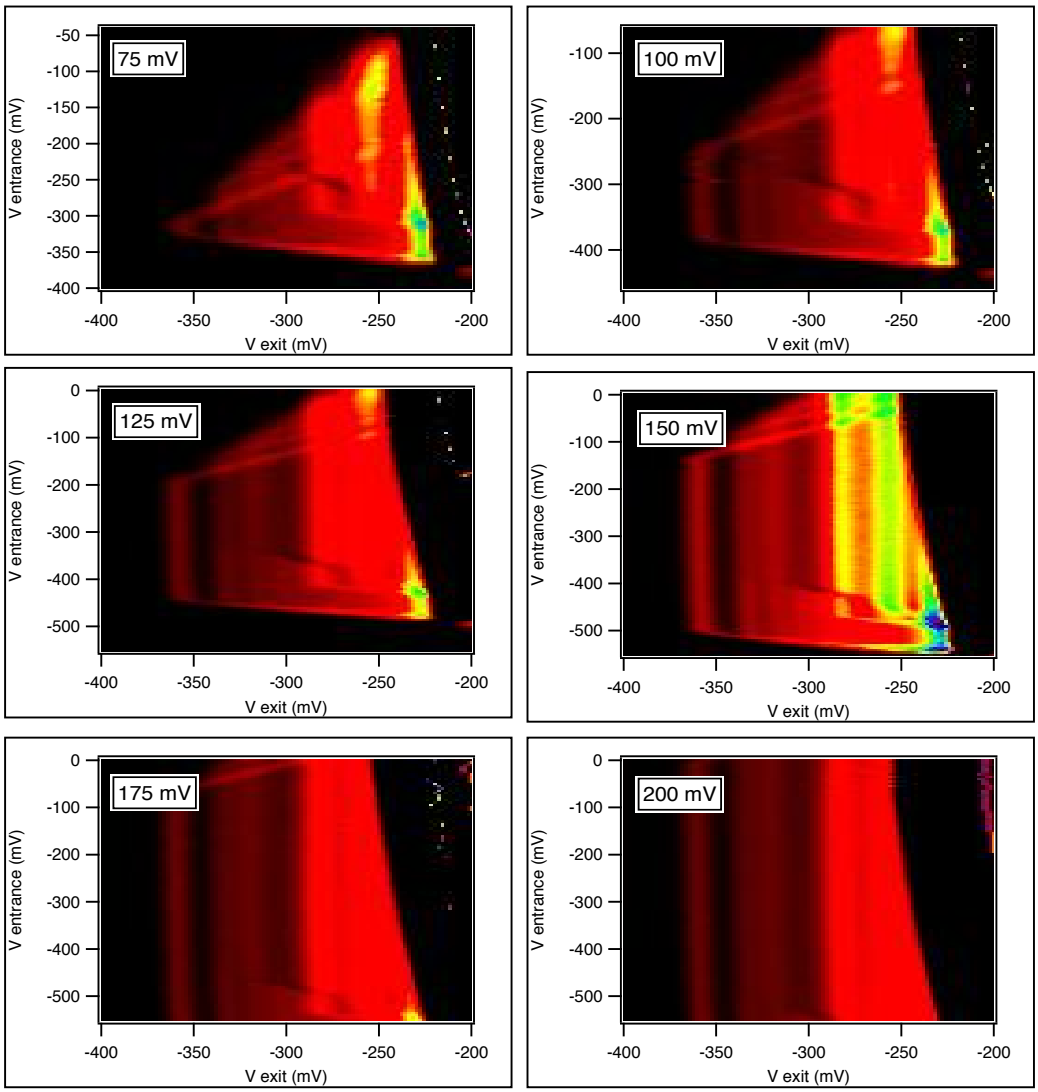

Figure 7.4: Pump maps at different amplitudes. The RF peak-to-peak amplitude is given in the insets. T = 4.2 K, f = 100 MHz

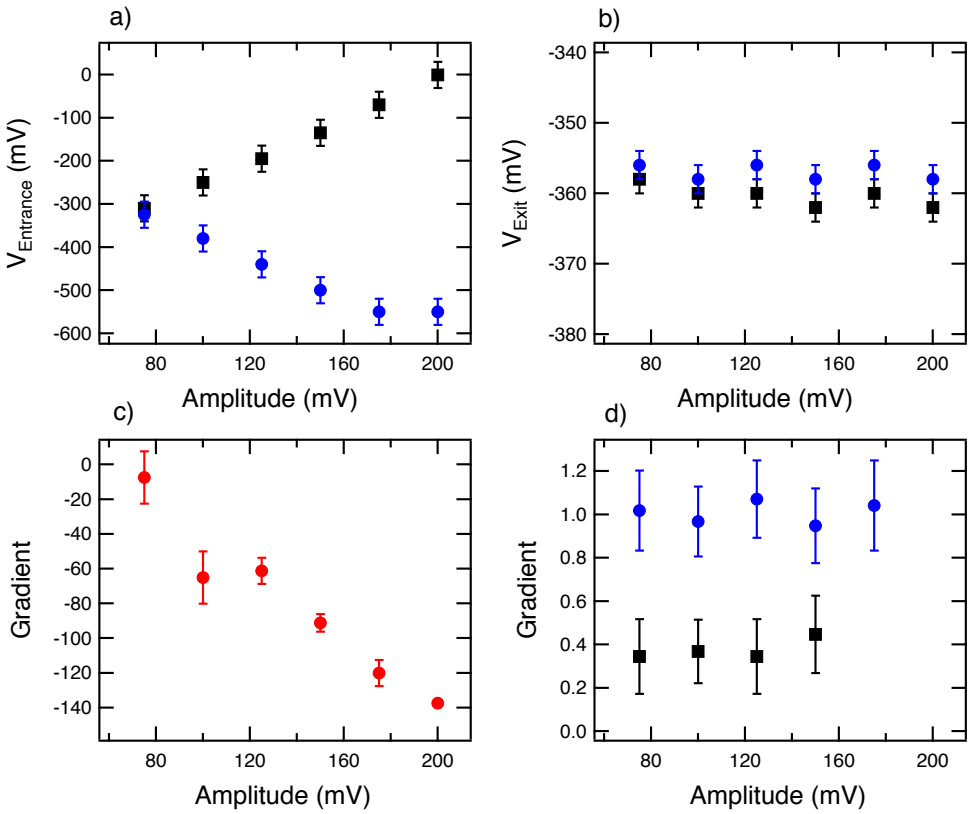

Figure 7.5: The values of (a) V_{Ent} and (b) V_{Exit} for nodes 1 (black square) and 2 (blue circles) on the pump maps as a function of amplitude. (c) The gradient of the onset line vs. amplitude. (d) The gradient of the ejection line (blue circles) and the modulus of the gradient of the capture line (black squares) vs. amplitude.

Using Figure 7.3 as a reference for identifying the capture, ejection, and pump onset lines, as well as nodes 1 and 2. We measured how pump map lines and nodes shifted when RF peak-to-peak amplitude was increased. Figure 7.5 shows the position of nodes 1 and 2, and the slopes of the capture, ejection, and pump onset lines.

- The capture line shifts to more negative V_{Ent} indefinitely.

  Figure 7.5a shows the capture line (blue circles) shift linearly from $V_{\mathrm{Ent}} \approx -300\,\mathrm{mV}$ at RF amplitude $A = 75\,\mathrm{mV}$ to $V_{\mathrm{Ent}} < -550\,\mathrm{mV}$ at RF amplitude $A = 200\,\mathrm{mV}$.

- The ejection line shifts to less negative V_{Ent} indefinitely.

Figure 7.5a shows the ejection line (black squares) shift linearly from $V_{\text{Ent}} \approx -300$ mV at RF amplitude $A = 75$ mV to $V_{\text{Ent}} \approx 0$ mV at RF amplitude $A = 200$ mV.

- The pump onset line remains fixed in V_{Exit}.

  Figure 7.5b shows the onset line (the end of which are given by the blue circles and black squares) fixed at $V_{\text{Exit}} \approx -358$ mV for RF amplitudes $A = 75 \rightarrow 200$ mV.

- The pump onset line becomes more vertical.

  Figure 7.5c shows the gradient of the onset line increases from -8 to -140 as RF amplitude is increased from $A = 75 \rightarrow 200$ mV.

In addition to the 4 main effects that impact our model, we note one lesser effect: Figure 7.5d shows the magnitude of the gradient of the capture and ejection lines, which do not change with RF amplitude.

In section 7.8 we present a model that explains the shifts in the pump map lines and fit it to the line scans. We took low resolution line scans to quickly generate pump maps to measure the shifts in the pump map lines. In order to generate better fits, we took high resolution line scans at fixed V_{Ent} to fit an equation to, (Figure 7.6a). Accordingly, we repeated these measurements, on a different thermal cycle, with higher resolution line scans at V_{Ent} = -300 mV, (Figure 7.6b). The pinch-off changes between the two scans from $V_{\text{Ent}} \approx -363$mV to $V_{\text{Ent}} \approx -405$ mV; we attribute this to charging effects between the thermal cycles.

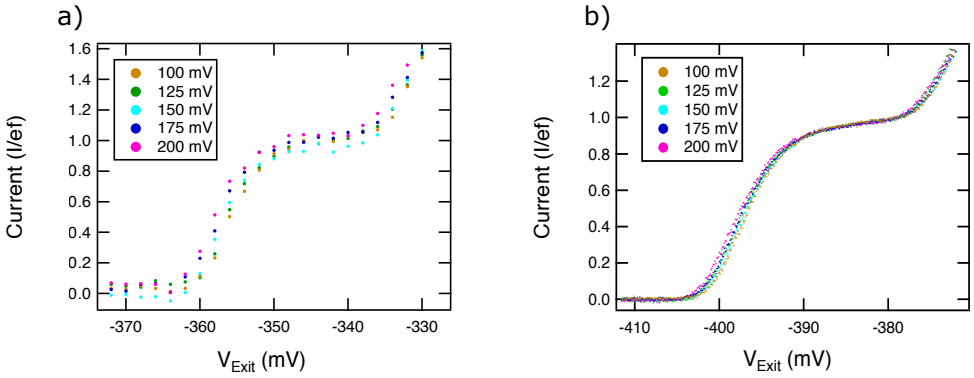

Figure 7.6: (a) A plot of current vs. exit gate voltage at V_{Ent} = -300 mV taken at T = 4.2 K. (b) A high resolution sweep taken after a thermal cycle.

7.4 Temperature

We measured the temperature dependence of pumped current using a split gate pump on a Teslatron cryostat at T = 1.6 K to 14 K. Figure 7.7 shows pump maps at f = 100 MHz and peak-to-peak RF amplitude at the RF source of 252 mV.

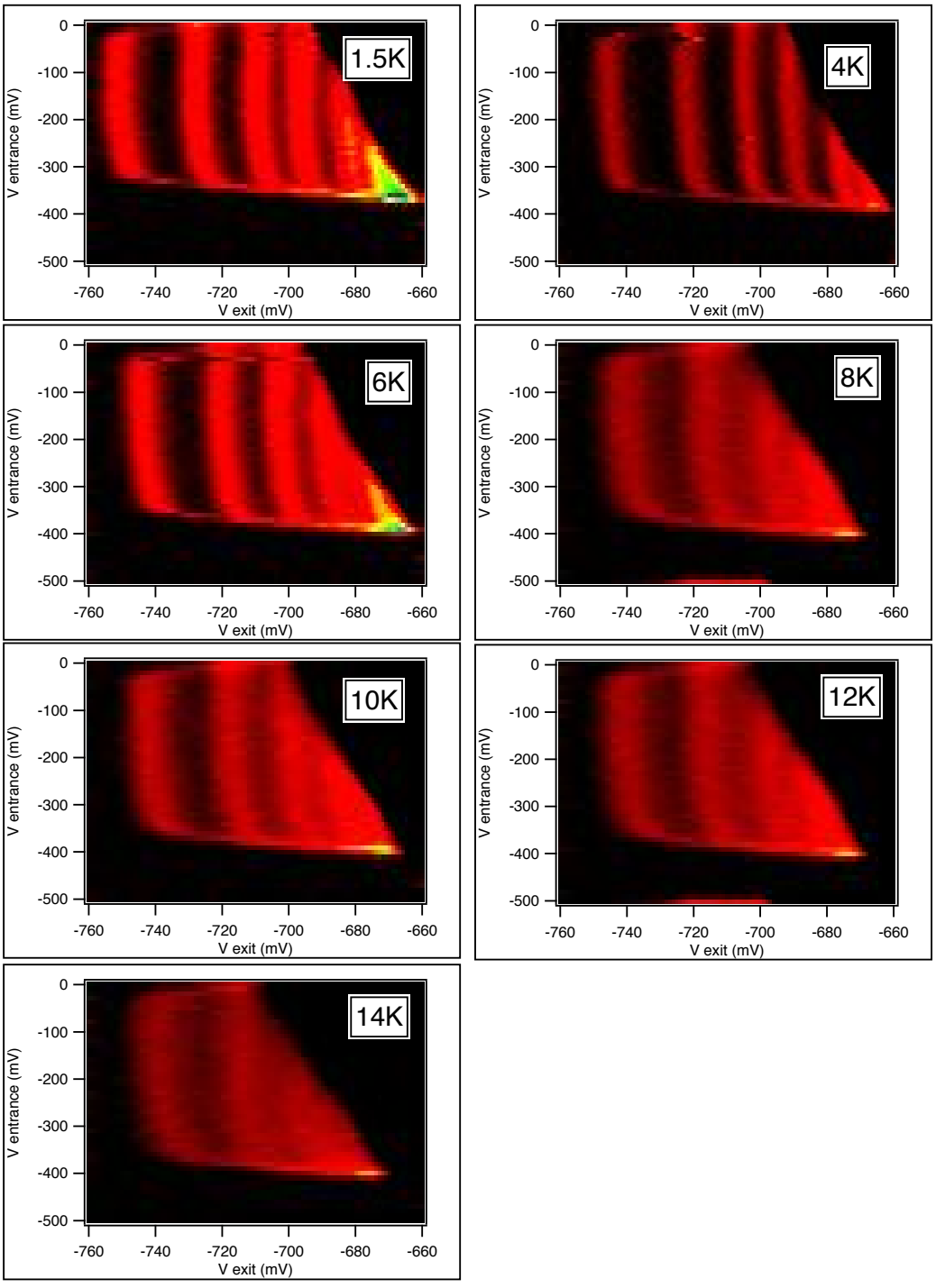

Figure 7.7: Pump maps at different temperatures, given in the inserts. Peak-to-peak RF amplitude = 252 mV, f = 100 MHz.

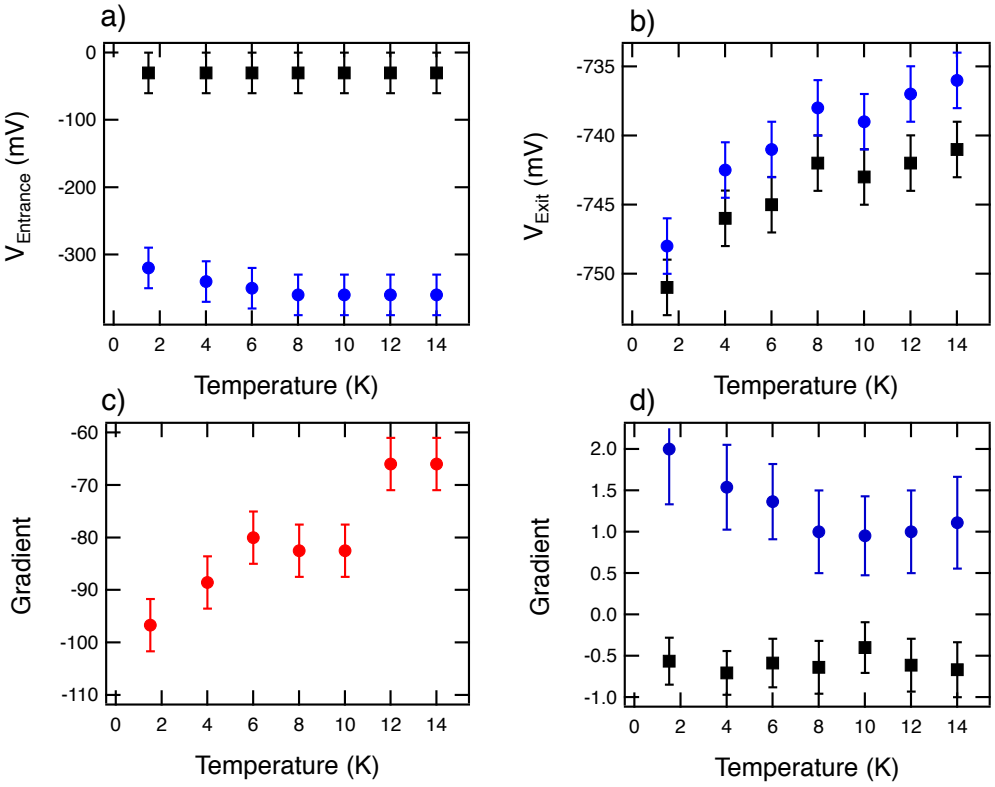

Figure 7.8: The values of (a) V_{Ent} and (b) V_{Exit} for nodes 1 (black squares) and 2 (blue circles) on the pump maps vs. temperature. (c) The gradient of the pump onset line vs. temperature. (d) The gradient of the ejection line (blue circles) and the capture line (black squares) vs. temperature.

Figure 7.8 shows the positions of nodes 1 and 2, and the slopes of the capture, ejection, and onset lines, in V_{Ent} and V_{Exit}, plotted against temperature. Figures 7.9a,b show high resolution sweeps taken at V_{Ent} = -300 mV and Figures 7.9c,d show line scans of current vs. V_{Ent} taken at V_{Exit} = -735 mV. The number of data points is equal to the number of line scans in V_{Ent} to form the colourmap. Normally, current is not shown as a function of V_{Ent} as it does not show the usual plateaus, but it does show other interesting features described below. When temperature is increased we observe 4 main effects:

- The onset line remains fixed in V_{Exit}.

  In Figure 7.8b, the onset line appears to move to less negative V_{Exit}. This apparent movement is caused by a discrepancy between the definition of

the onset line and the line joining nodes 1 and 2. The onset line is the line formed by the pinch-off in V_{Exit}. The pump map shows dI/dV_{Exit}, so the line joining nodes 1 and 2 is formed by the peaks of the V_{Exit} derivative curves. For pump plateaus with a slow rising current, such measurements give the illusion that the line is shifted to less negative V_{Exit}, when the real pinch-off values remain the same. It is clear from the high resolution sweeps in Figure 7.9b that deviations from the ideal pump current are increased, but the pinch-off voltage converges on V_{Exit} = -747 mV for all temperatures.

- The ejection line remains fixed in V_{Ent}.

  Figure 7.8a shows that node 1 remains fixed in V_{Ent}. In Figure 7.8d, the gradient of the ejection line appears to decrease until T = 8 K, but again this is due to our measuring the locations of the derivative peaks and not the pinch-off values.

- The capture line shifts to more negative V_{Ent}.

  Figure 7.8a shows that node 2 shifts in V_{Ent} from -320 mV $\rightarrow$ -360 mV, until T = 8 K, where it saturates. The shift is real and not an artefact of a derivative plot. Figures 7.9c,d show line scans of the pump maps at fixed V_{Exit}. The need to explain the difference in the way the onset and capture lines shift with increased temperature strongly motivated the capture model described in section 7.8.

- The reduction in current near the ejection line is smaller than the reduction near the capture line.

  In Figure 7.9c, the current drops as the entrance gate voltage is made more negative. The slope of the dashed red line, at T = 14 K, is greater than the slope of the dashed grey line, at T = 4 K. The sweep at T = 1.6 K was taken at a different thermal cycle.

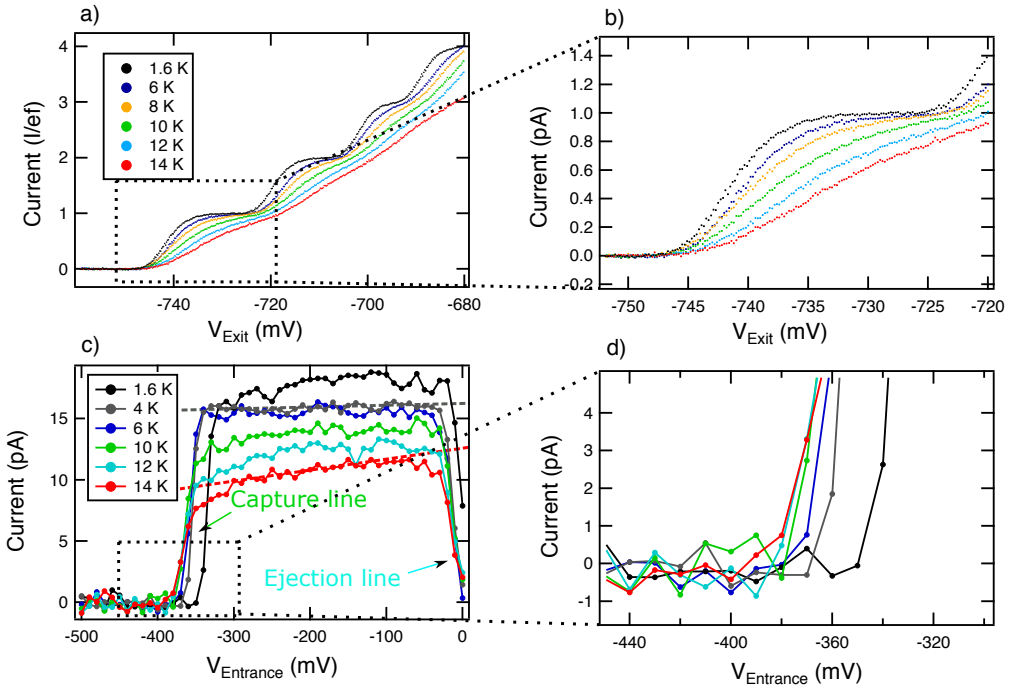

Figure 7.9: (a) Pump current at $V_{\mathrm{Ent}} = -300\,\mathrm{mV}$. (b) Zoomed in on the first plateau formation. (c) Pump current taken as a vertical slice through Figure 7.7 at $V_{\mathrm{Exit}} = -735\,\mathrm{mV}$. (d) Zoomed in on the capture line region.

7.5 Frequency

We measured the frequency dependence of pumped current using a split-gate pump at T = 1.6 K. Figure 7.10 shows pump maps of the split-gate pump over a range of frequencies from 0.1 GHz to 0.8 GHz in 0.1 GHz steps.

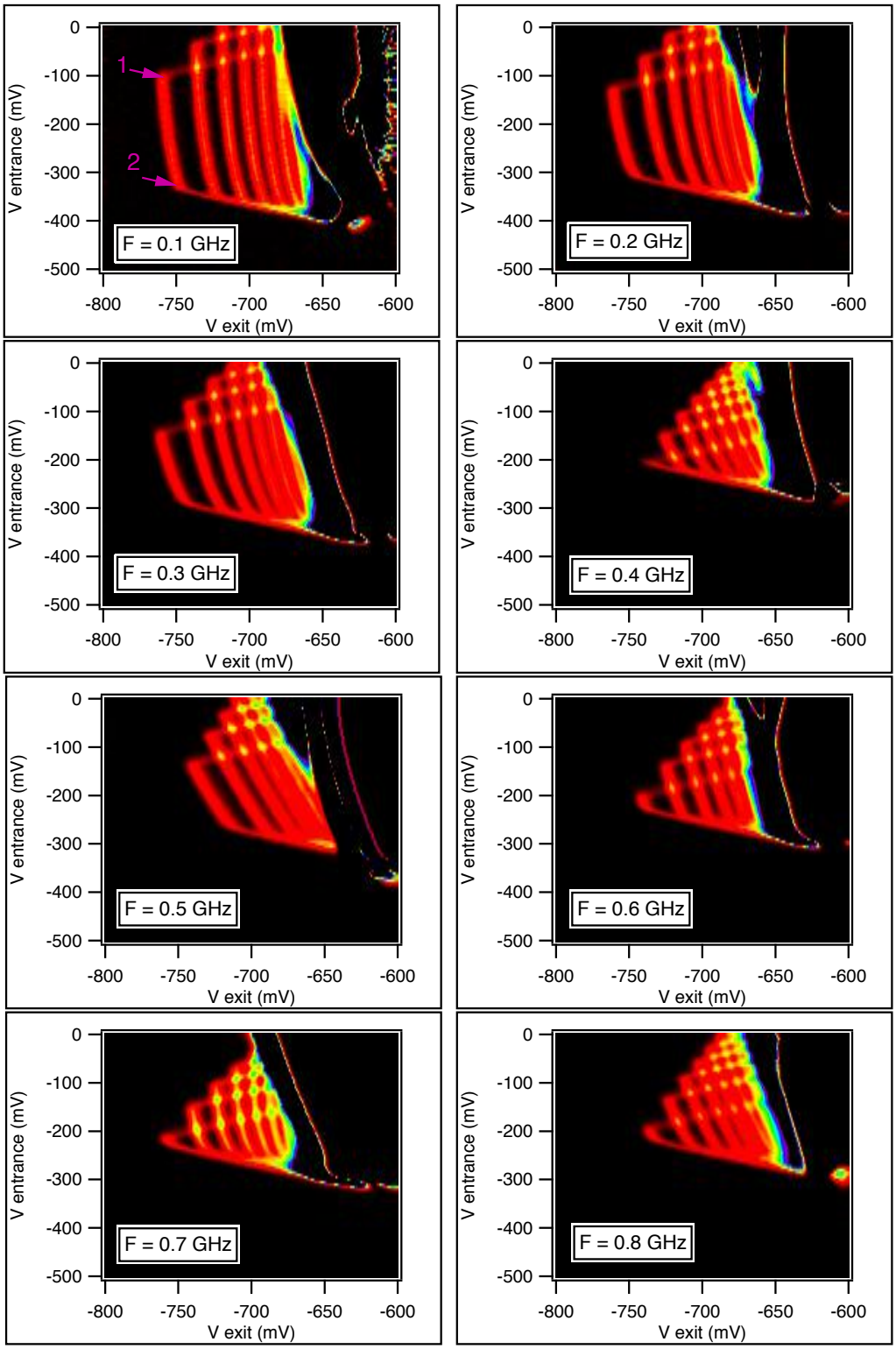

Figure 7.10: Pump maps of the split-gate style device at a temperature of 1.5 K for frequencies ranging from 0.1 GHz to 0.8 GHz. A magnetic field of 4 T was applied perpendicular to the 2DEG and the amplitude set to 225 mV.

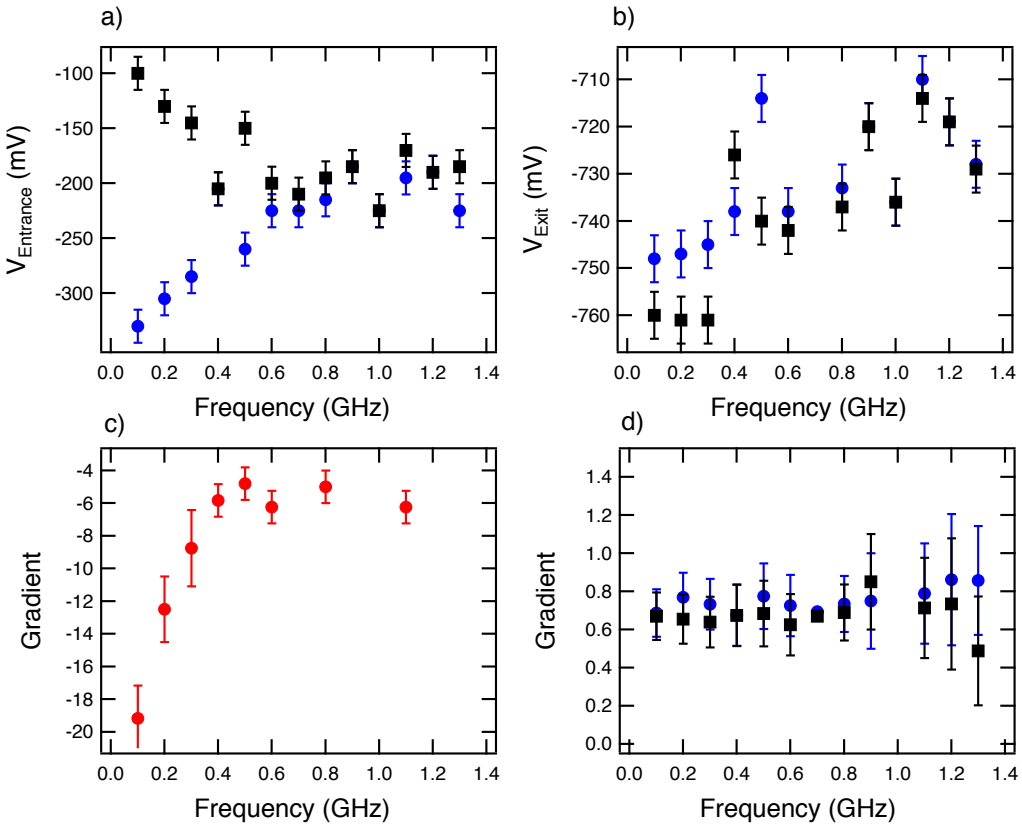

Figure 7.11: The values of (a) V_{Ent} and (b) V_{Exit} for nodes 1 (black square) and 2 (blue circles) vs. frequency. (c) The gradient of the pump onset line vs. frequency. (d) The gradient of the ejection line (blue circles) and the modulus of the gradient of the capture line (black squares) vs. frequency.

At frequencies above 1.0 GHz the pump maps deteriorate, but this may be attributed to attenuation in the RF lines in the probe. The probe was fitted with UT-85-SS RF lines, which made it difficult to form a proper impedance matched connection when adding SMA connectors to them. It is probable that poor soldering of these lines resulted in large attenuation above 1.0 GHz. However, we expect the frequency response of the lines to be similar to that of the probe used in Chapter 6, Figure 6.9.

Figure 7.11 shows the position of nodes 1 and 2, and the slopes of the capture, ejection, and pump onset lines. When frequency is increased we observe 3 main effects:

- The capture line shifts to less negative V_{Ent}.

  Figure 7.11a shows the capture line (blue circles) shift from $V_{\text{Ent}} \approx -340\text{mV}$ at $f = 0.1\text{GHz}$ to $V_{\text{Ent}} \approx -220\text{mV}$ at $f = 0.6\text{GHz}$, past which V_{Ent} saturates at ≈ -220 mV.

- The ejection line shifts to more negative V_{Ent}.

  Figure 7.11a shows the ejection line (black squares) shift from $V_{\text{Ent}} \approx -100$ mV at $f = 0.1$ GHz to $V_{\text{Ent}} \approx -220$ mV at $f = 0.6$ GHz, past which V_{Ent} saturates at ≈ -220 mV.

- The slope of onset line becomes less vertical.

  Figure 7.11c shows that the onset line becomes less vertical as frequency is increased from $f = 0.1 \rightarrow 0.5$ GHz, past which the slope saturates.

In addition to the 4 main effects we note 2 lesser effects: the onset line shifts to less negative exit gate voltages in a random way, probably because of the experimental limitations, (Figure 7.11b), and the magnitude of slope of the capture and ejection lines remain constant with frequency, (Figure 7.11d). Figure 7.12 shows a high resolution line scan of the colourmap that the model is fitted to in section 7.11.

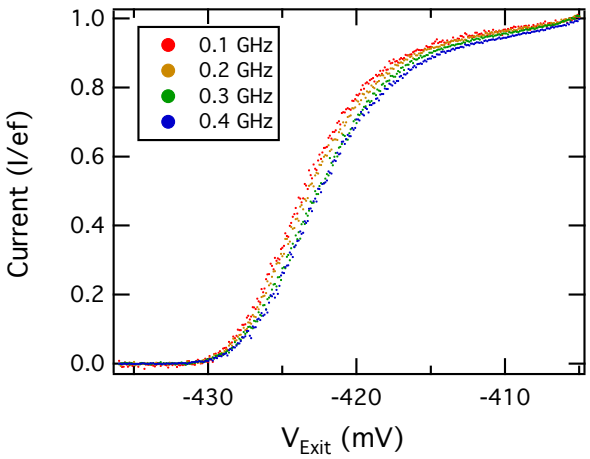

Figure 7.12: A plot of current vs. exit gate voltage at V_{Ent} = -200 mV.

7.6 Our model

In this section we present a model that we developed to explain the deviation from the ideal pump plateau line, and the observed shifts of the pump map lines, at different amplitudes. We derive an equation for the pumped current based on back-tunnelling probabilities in the decay phase and on capture probabilities in the capture phase. To make the derivation more straightforward, we make some simple assumptions about the back-tunnelling process. The advantage of making such assumptions is the ability to predict how changes in the RF amplitude affect the pump current errors. We extend our model to include temperature and frequency effects to produce a more complete description of the pump current in section 7.8.

7.6.1 Assumptions

In the following, we consider the decay phase of the pump cycle at T = 0 K. This section lists, and argues for the validity of, our assumptions on which we base our model.

- As the entrance barrier rises, back-tunnelling is suppressed because the barrier gets bigger.

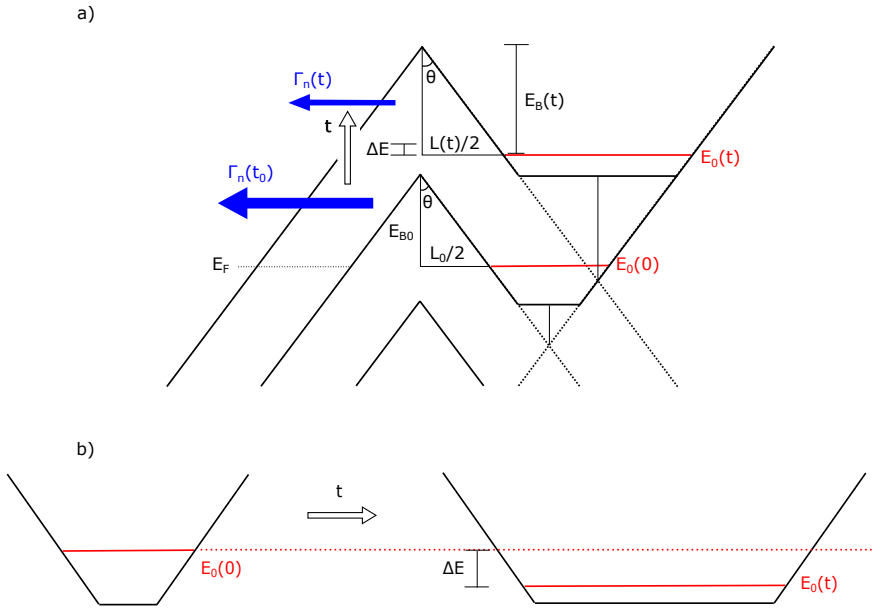

Figure 7.13: A geometrical explanation for the increase in barrier width and height while rising.

Assuming that, over the range that back-tunnelling occurs, the potential slopes of the exit and entrance barriers are roughly linear and symmetric, the increase in barrier height and width can be shown using a simple geometrical argument. Figure 7.13a shows an energy schematic of the entrance barrier as a triangular potential. The lower triangular potential shows the barrier at t_0, when the energy level in the dot it level with the Fermi energy. At t_0, the barrier height is E_{B0} and the barrier width is L_0. Because the total potential due to both gates is a superposition of the two, the base of the dot will also rise at the same rate as the entrance gate potential. While the dot height remains the same, the dot width increases with time, Figure 7.13b. This pushes the ground state down relative to the bottom of the dot, effectively increasing the entrance barrier height. $\Delta E(t)$ is the decrease in energy level relative to the bottom of the dot as the dot gets wider. From this, we get an expression for the barrier height and width at time t.

$$E_B(t) = E_{B0} + \Delta E(t) \tag{7.2}$$

$$L(t) = \frac{L_0}{E_{B0}} E_B(t) \tag{7.3}$$

The perfectly triangular barrier is an idealised case used to show the linear increase in barrier height and width by making use of the symmetry between the potentials of the entrance and exit gates. The same linear increase applies to any shaped potential barrier, given that both the width increases linearly with height and the entrance and exit gate potentials have symmetrical slopes at the base of the dot. It is reasonable to assume that the dot shape is parabolic because the dot is formed from two overlapping parabolic potentials, as drawn in Figure 7.1.

- As the entrance barrier rises, the dot gets wider.

  This follows from the previous assumption and Figure 7.13, until $E_{\mathrm{Ent}} = E_{\mathrm{Exit}}$. As E_{Ent} is further raised above E_{Exit}, the dot gets narrower. The pump operation is commonly explained as the 'squeezing' of a dot, causing electrons to back-tunnel until the desired number remain. However, from split-gate measurements we know that the pinch-off voltage is more negative than the definition voltage. If the gap between the entrance and exit gates is less than half the gap between the split-gates, as is the case for our split-gate pumps, then, at the split-gate pinch off voltage, the gap between the entrance and exit gates is already depleted and cannot be 'squeezed' by the entrance gate.

- At $t = t_0$ all N available energy levels in the dot will be filled, which determines the ideal current.

  This assumption means that no electrons tunnel from the source into the dot after t_0, (the case where T $>$ 0 K will be considered in section 7.8). If there are no error mechanisms and no thermal broadening, no electrons will back-tunnel from the dot to the source after t_0. Therefore, the number of electrons that contribute to current is equal to N, the number of electrons at t_0. This forms an ideal current $I_{\mathrm{Ideal}} = Nef$. Figure 7.14 shows the ideal current (the blue line). It is a series of sharp quantised steps that vary with the initial dot size N, which is determined by V_{Exit}. As there is no mechanism by which pumped current can be higher than the ideal pumped

current, the ideal current sets an upper bound on pumped current. The measured pump current $I_P = \langle n \rangle ef$, where $\langle n \rangle$ is the average number of electrons pumped per cycle. The deviation from the ideal current, ρ_{error}, is due to electrons back-tunnelling into the source.

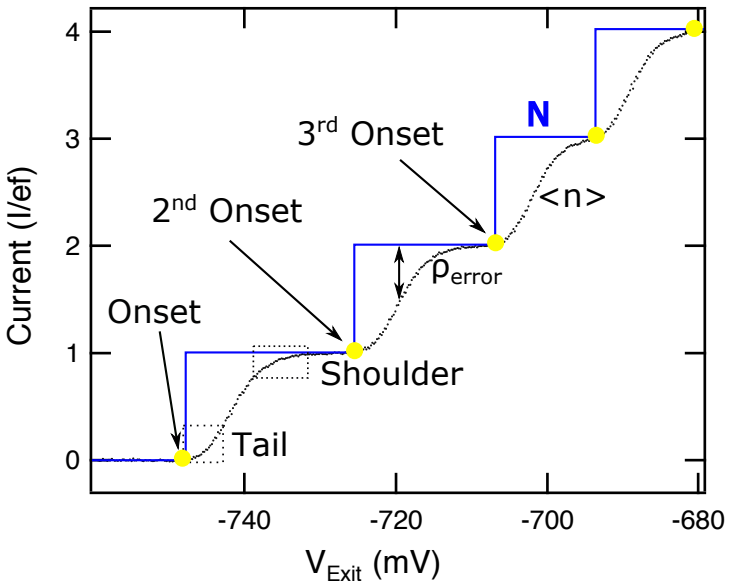

Figure 7.14: A plot of pumped current with the proposed ideal current overlaid.

- Electron tunnelling rates are not affected by the other electrons in the dot.

  Electrons are treated as non-interacting in the dot. We calculate the probability of electrons in a many-electron dot by summing over the probability of each electron contributing to pump current.

$$\langle n \rangle = \sum_{n}^{N} P_n(t_{0n}) \tag{7.4}$$

  where $P_n(t)$ is the probability that the n$^{\text{th}}$ electron is in the dot at time t, and t_{0n} is the time at which $E_n = E_F$.

7.6.2 An equation for pump current

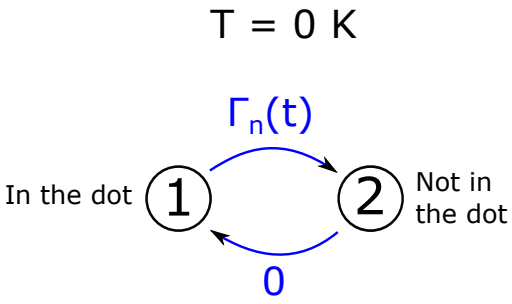

Figure 7.15: A diagram of the two-state birth-death time-continuous Markov process at T = 0 K, which simplifies to a non-homogeneous Poisson distribution.

In calculating the probability of back-tunnelling, we regard tunnelling out of a dot with a time varying tunnelling rate as a two-state non-homogeneous Poisson process, with state 1 being an electron in the dot and state 2 being an electron not in the dot, (Figure 7.15). The probability that an electron will remain in a dot after time t is given by

$$P_n(t) = P_n(t_0)e^{-\langle\Gamma_n(t)\rangle} \tag{7.5}$$

Where

$$\langle\Gamma_n(t)\rangle = \int_{t_0}^{t} \Gamma_n(t')dt' \tag{7.6}$$

This is the solution to the master equation

$$\frac{dP_n}{dt} = -\langle\Gamma_n(t)\rangle P_n(t) \tag{7.7}$$

but with the time independent tunnelling rate replaced with the time averaged tunnelling rate $\langle\Gamma_n(t)\rangle$

To calculate the tunnelling probability through a barrier we use the Wentzel-Kramers-Brillouin (WKB) approximation. Note that this is a probability and not a rate. To get the rate we multiply the tunnelling probability by the density of states, which for a 0D dot is a delta function at a particular energy level ≈ 1, and a constant factor W, which is a function of the time spent at a particular energy level, the inverse of the rise rate, with units Hz. $W \propto 1/(Af)$.

$$\Gamma_n = We^{-k\int_0^L \sqrt{eV(x)-E_n}\ dx} \tag{7.8}$$

Where $k = 2\frac{\sqrt{2m^*}}{\hbar}$ and m^* is the effective mass of the electron. We treat the barrier as parabolic with height $E_B(t)$ and width $L(t)$. For $-L/2 < x < L/2$, $eV(x) - E_n = E_B(1 - (2x/L)^2)$. Because the barrier is symmetric about $x = 0$, we integrate from 0 to $L/2$ and multiply by 2.

$$\int_{-L/2}^{L/2} \sqrt{eV(x) - E_n}\ dx = 2\int_0^{L/2} \sqrt{E_{Bn}(1 - (2x/L)^2)}\ dx \tag{7.9}$$

The tunnelling rate for the parabolic barrier is given by

$$\Gamma_n(\Delta E) = W\exp\Bigg[-2k\int_0^{L/2} \sqrt{E_B(1 - (2x/L)^2)}\ dx\Bigg] \tag{7.10}$$

$$= W\exp\left[\frac{-k\pi}{2}\sqrt{E_B}L\right] \tag{7.11}$$

Substituting 7.2 and 7.3 into 7.11 gives

$$\Gamma_n(\Delta E) = W\exp\left[\frac{-k\pi}{2}\frac{L_0}{E_{B0}}(E_{B0n} + \Delta E)^{3/2}\right] \tag{7.12}$$

$$= W\exp\Big[-\beta(E_{B0n} + \Delta E)^{3/2}\Big] \tag{7.13}$$

where $\beta = \frac{k\pi}{2}\frac{L_0}{E_{B0}}$. As the tunnelling rate will decrease as the dot gets wider until the ground state is at the base of the dot, $\Delta E = \hbar\omega_0$. If this tunnelling rate is considered negligible, integrating $\Gamma_n(\Delta E)$ from $0 \rightarrow \hbar\omega$ is therefore equivalent to integrating from $0 \rightarrow \infty$.

$$\langle \Gamma_n(\Delta E) \rangle = W \int_0^{\infty} \exp\Big[-\beta(E_{B0n} + \Delta E)^{3/2} \Big] \, d\Delta E \tag{7.14}$$

Integrating $\Gamma_n(t)$ is non-trivial. However, if we use the approximation of a first order Taylor expansion, $(a+bt)^{3/2} \approx a^{3/2} + (3/2)\sqrt{a}bt$, we can arrive at a reasonable expression for the pumped current. Although the Taylor expansion is valid only for small t, we justify using it because for large t the negative exponential tends to 0 and becomes negligible.

$$\langle \Gamma_n(\Delta E) \rangle = W \int_0^{\infty} \exp(-\beta(E_{B0n}^{3/2} + (3/2)\sqrt{E_{B0n}}\Delta E)) \, d\Delta E \tag{7.15}$$

$$\langle \Gamma_n(\Delta E) \rangle = W \exp(-\beta E_{B0n}^{3/2}) \int_0^{\infty} \exp(-\beta(3/2)\sqrt{E_{B0n}}\Delta E) \, d\Delta E \tag{7.16}$$

$$\langle \Gamma_n(\Delta E) \rangle = W \exp(-\beta E_{B0n}^{3/2}) \frac{1}{\beta(3/2)\sqrt{E_{B0n}}} \tag{7.17}$$

$$\langle \Gamma_n(\Delta E) \rangle = \frac{2W}{3\beta\sqrt{E_{B0n}}} \exp(-\beta E_{B0n}^{3/2}) \tag{7.18}$$

The resulting probability of the electron remaining in the dot is the average back-tunnelling rate times divided by the rise rate of the entrance barrier, AF, into equation 7.5.

$$P_n(\infty) = P_n(t_0) \exp\Big[-\frac{\alpha}{\beta\sqrt{E_{B0n}}} \exp(-\beta E_{B0n}^{3/2}) \Big] \tag{7.19}$$

Where $\alpha = \frac{2W}{3Af}$.

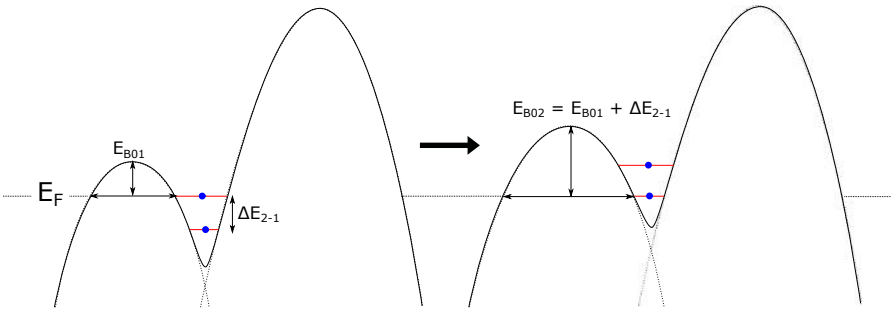

Figure 7.16: Diagram showing how different electrons are treated in the dot.

So far we have considered only a single electron in the dot. In considering a many-electron dot, ignoring Coulomb effects, we treat the electrons as non-interacting, so the back-tunnelling rate of one electron is independent of other electrons in the dot. To accommodate a many-electron dot in our model, we sum over the probabilities of all electrons in the dot. The only difference between the electrons with respect to their back-tunnelling probabilities is their initial barrier height, $E_{B0n} = E_{B0} + (E_n(t_0) - E_1(t_0))$, (Figure 7.16). This is expressed in terms of the exit gate voltage, $E_{B0n} = V_{\text{Exit}} + V_n$.

$$\langle n \rangle = \sum_{n}^{N} P_n(t_0) \exp\left[-\frac{\alpha}{\beta\sqrt{V_{\text{Exit}} + V_n}} \exp(-\beta(V_{\text{Exit}} + V_n)^{3/2}) \right] \tag{7.20}$$

We can begin to fit the data with this equation. Fitting the data with an equation with multiple parameters can be problematic as different combinations of parameter values will produce the same result, (e.g. doubling both W and A has no effect on $\langle n \rangle$). Further, fitting a double exponential function is especially difficult as $\langle n \rangle$ depends strongly on β and there are many local minima in the fitted regression that the fit can converge to, giving poor fits. To ensure a physically meaningful fit, plausible seed values for the parameters consistent with our model must be used.

As our model is based on back-tunnelling through a barrier, one requirement is that $E_{B0} > 0$. If $E_{B0} \not> 0$ there is no barrier to form a dot at t_0, and $\langle n \rangle = 0$. The exit gate voltage at which $E_{B0} = 0$ is V_0, which should form the onset point, (Figure 7.14). We incorporate this requirement into equation 7.20, which we fit

to the amplitude dependence data.

7.7 Amplitude analysis

Figure 7.17a shows the higher resolution data from Figure 7.6b fitted with equation 7.20. We put an upper limit on V_0 and V_1 from the exit gate voltages of the onset lines in Figure 7.6b. Respectively, this requires V_0 and V_1 to be more negative than -404 mV and -379 mV. Figure 7.17a shows the fits (solid lines) overlaid on the data (points). The fitting parameters were $V_0 = -418.18$ mV, $V_1 = -393.04$ mV, and α is plotted against amplitude in Figure 7.17d. The model predicts that the onset line should be pushed out to more negative exit gate voltages as the amplitude increases, which is reflected in the data for all amplitudes, except at $A = 125$ mV. This exception is so marked that we expect external factors impacted the measurement. Physically, the most likely explanation is that at a higher amplitude the barrier rises more quickly, so there is less time for an electron to tunnel out and contribute to error. Respectively, Figures 7.17b and 7.17c show a zoomed-in view of Figure 7.17a of the shoulder and tail. The fit of the tail is better than the fit of the shoulder, where the fit is higher than the data. We attribute this poor fit to the thermal broadening effects. We take thermal broadening into consideration in section 7.8 and extend the model to account for it.

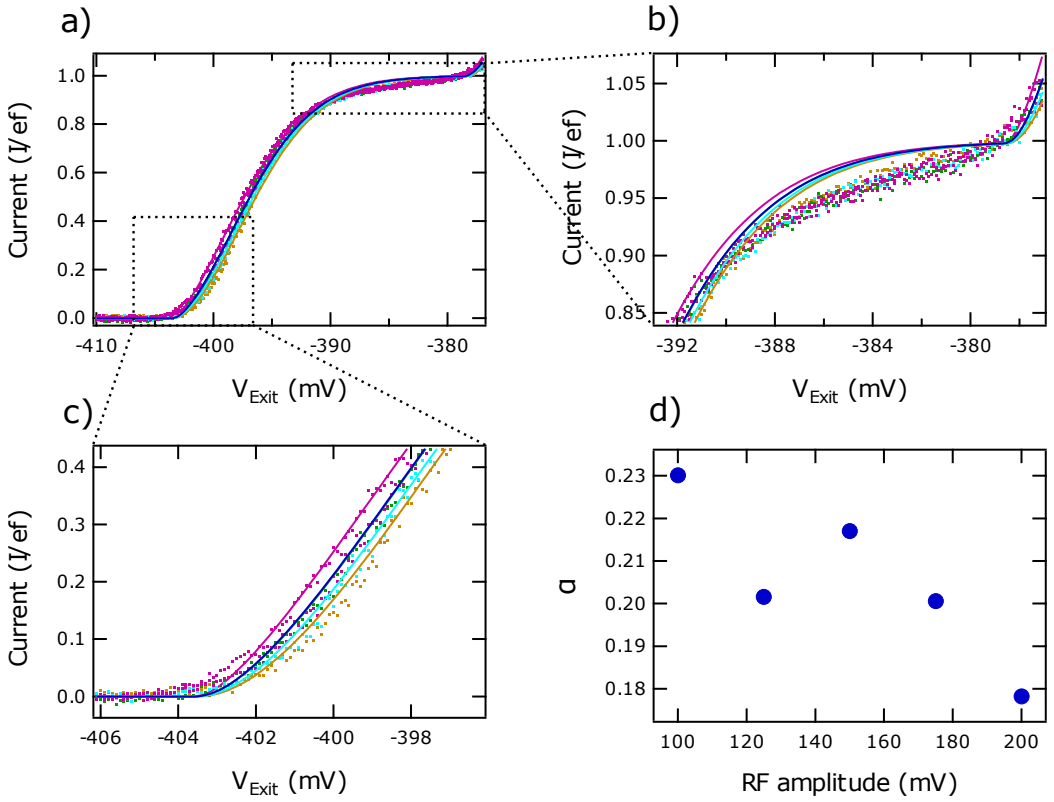

Figure 7.17: (a) A plot of current vs. exit gate voltage for different values of exit gate voltage with fittings overlaid. (b) The residuals of the shoulder highlighted. (c) A zoomed plot of the tail. (d) The α fitting values for the different amplitudes.

Equation 7.20 has a term between the two exponentials; in this it differs from the equation used to fit data in the UDC model. The UDC equation takes the form $\langle n \rangle = \sum_n \exp(-\exp(-(\alpha V_{\text{Exit}} - \delta_n)))$, where α and δ_n are physical constants that are used as fitting parameters [61]. In order to fit this equation to the tail of a pump plateau, $\alpha V_{\text{Exit}} - \delta_n$ must be negative for some values of V_{Exit}. This is not allowed in a model predicated on back-tunnelling errors because $0 < \Gamma_n < 1$: the double exponential term, $\alpha V_{\text{Exit}} - \delta_n$, which is a measure of the tunnelling barrier dimensions, cannot be negative.

The model presented in this chapter does not encounter the same issue, as discussed at the end of section 7.6. Equation 7.20 fits the data without the double exponential term, $\beta(V_{\text{Exit}} + V_n)^{3/2}$, becoming negative. In order to generate the tail of the pump current, whilst keeping the double exponential term positive, the

term between the exponentials, $\frac{\alpha}{\beta\sqrt{V_{\text{Exit}}+V_n}}$, needs to be large. α is proportional to the inverse of the barrier rise rate. If the RF amplitude increases, the barrier rises more quickly, so the probability of back-tunnelling over the decay phase decreases, resulting in the onset line shifting to more negative exit gate voltages. This is observed in Figure 7.17. The model predicts that the onset line will not shift out indefinitely. When the exit gate is made very negative, E_{B0n} goes to 0. From equation 7.19, when $E_{B0} \to 0$, $P_n(t) \to 0$. In this regime a dot never forms, making it impossible to generate pump current.

While equation 7.20 in section 7.6.2 fits the tail of amplitude-dependent data well, it does not fit the shoulder well, nor does our model explain shifts in the capture and ejection lines in Figure 7.4, most noticeably the widening of the onset line in V_{Ent}. In addition to this, the model incorrectly predicts the frequency-dependence of the pump. $\alpha = \frac{2W}{3Af}$ so increasing frequency should have the same effect as increasing amplitude, and increase pumped current. However, from section 7.5, increasing frequency has the opposite effect: it decreases pumped current. Lastly, equation 7.20 has no temperature-dependent term, so the model cannot be used to fit the temperature dependence of the pumped current. To address these limitations, we expand this model to include a temperature-dependent capture term that determines $P_n(t_0)$.

7.8 Modifying the model to account for thermal broadening and capture errors

The above model assumes T = 0 K and that at $P_{\text{n}}(t_0) = 1$. To make predictions about temperature, we rework the above model by including the Fermi distribution of the leads in the master equation, and including the probability of tunnelling into the dot as well as out of it. These inclusions lead to a two-state birth-death Markov process with time-varying tunnelling rates, (Figure 7.18). While doing a precise time-varying calculation is outside the scope of this thesis, we make some approximations that are appropriate to solving the two-state birth-death Markov process with fixed tunnelling rates. The approximations also permit a physical interpretation of the model.

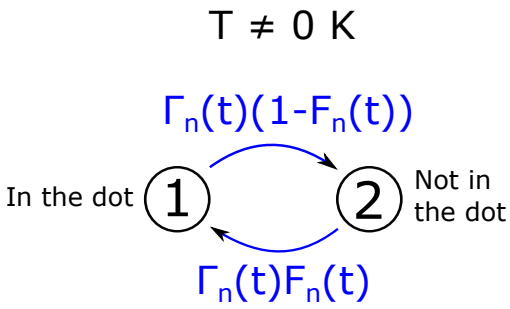

Figure 7.18: A diagram of the two-state birth-death time-continuous Markov process at T $\neq$ 0 K.

Between time t_c and t_0, the dot is below the Fermi level, and electrons tunnel into and back out of it. If the barrier is small and the dot is strongly coupled to the source, the probability of an electron being captured is given by the Fermi distribution.

$$F(E_\mathrm{n}) = \frac{1}{1 + e^{(E_F - E_\mathrm{n})/k_b T}} \tag{7.21}$$

where k_b is the Boltzmann constant and T is the temperature of the leads. As the dot rises the tunnelling probability drops off exponentially. If we model the rise of the dot as a set of discrete steps ΔE, with a dwell time at each step of τ, we can predict the probability of an electron tunnelling into or out of the dot at a given barrier height. We solve the master equation for state 1 (in the dot, $P_\mathrm{n}^{(1)}(t)$, Figure 7.18) for a fixed Γ_n and $F(E_\mathrm{n})$.

$$\frac{dP_\mathrm{n}^{(1)}(t)}{dt} = -\Gamma_\mathrm{n}(1 - F(E_\mathrm{n}))P_\mathrm{n}^{(1)}(t) + \Gamma_\mathrm{n}F(E_\mathrm{n})P_\mathrm{n}^{(2)}(t) \tag{7.22}$$

Substituting $P_\mathrm{n}^{(2)}(t) = 1 - P_\mathrm{n}^{(1)}(t)$

$$\frac{dP_\mathrm{n}^{(1)}(t)}{dt} = -\Gamma_\mathrm{n}(1 - F(E_\mathrm{n}))P_\mathrm{n}^{(1)}(t) + \Gamma_\mathrm{n}F(E_\mathrm{n})(1 - P_\mathrm{n}^{(1)}(t)) \tag{7.23}$$

$$= -\Gamma_\mathrm{n}P_\mathrm{n}^{(1)}(t) + \Gamma_\mathrm{n}F(E_\mathrm{n}) \tag{7.24}$$

Solving the first order linear O.D.E

$$\frac{d}{dt}(P_{\mathrm{n}}^{(1)}(t)e^{\Gamma_{\mathrm{n}}t}) = \frac{dP_{\mathrm{n}}^{(1)}(t)}{dt}e^{\Gamma_{\mathrm{n}}t} + \Gamma_{\mathrm{n}}e^{\Gamma_{\mathrm{n}}t}P_{\mathrm{n}}^{(1)}(t) \tag{7.25}$$

$$\frac{d}{dt}(P_{\mathrm{n}}^{(1)}(t)e^{\Gamma_{\mathrm{n}}t}) = \Gamma_{\mathrm{n}}F(E_{\mathrm{n}})e^{\Gamma_{\mathrm{n}}t} \tag{7.26}$$

$$P_{\mathrm{n}}^{(1)}(t)e^{\Gamma_{\mathrm{n}}t} = \Gamma_{\mathrm{n}}F(E_{\mathrm{n}})\int e^{\Gamma_{\mathrm{n}}t}dt \tag{7.27}$$

$$P_{\mathrm{n}}^{(1)}(t)e^{\Gamma_{\mathrm{n}}t} = F(E_{\mathrm{n}})(e^{\Gamma_{\mathrm{n}}t} + C) \tag{7.28}$$

Using the initial condition $P_{\mathrm{n}}^{(1)}(t) = P_{\mathrm{n}}^{(1)}(0)$ at $t = 0$, and solving for C

$$P_{\mathrm{n}}^{(1)}(0) = F(E_{\mathrm{n}})(1 + C) \rightarrow C = \frac{P_{\mathrm{n}}^{(1)}(0)}{F(E_{\mathrm{n}})} - 1 \tag{7.29}$$

Substituting back into equation 7.28.

$$P_{\mathrm{n}}^{(1)}(t) = \underbrace{F(E_{\mathrm{n}})}_{\text{equilibrium}} + \underbrace{(P_{\mathrm{n}}^{(1)}(0) - F(E_{\mathrm{n}}))e^{-\Gamma_{\mathrm{n}}t}}_{\text{transition to equilibrium}} \tag{7.30}$$

This implies that if the dot is held at a particular energy for a long time, or is coupled strongly, the probability of having an electron in the dot will be the Fermi distribution of the leads at that energy. We assume that the dot is empty when it is first lowered below the Fermi level, at t_c. To form the initial condition for our model, we calculate the probability that the dot will collect an electron between t_c and t_0. If the dot were lowered and raised infinitely slowly, $P_{\mathrm{n}}(E_{\mathrm{n}}) = F(E_{\mathrm{n}})$ throughout the cycle, so no electrons would ever get pumped. However, when the dot is raised so quickly that the dwell time becomes comparable to the inverse tunnelling rate at a particular energy level, it may not have enough time to settle to the equilibrium occupation probability given by the Fermi distribution.

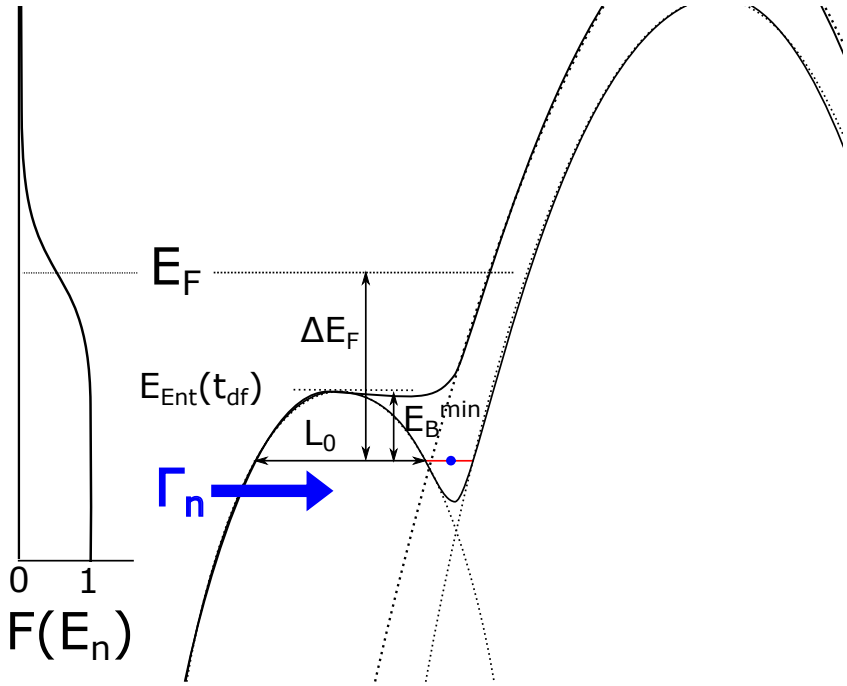

Figure 7.19: Diagram of the pumping cycle during the capture phase showing the dot formation point when V_{exit} is small.

Figure 7.19 shows the loading of the dot in the capture phase. When the exit gate voltage is small, the dot becomes larger. Once the dot is large enough to accommodate an electron, it will contain an electron with the probability of the Fermi distribution at the dot energy.

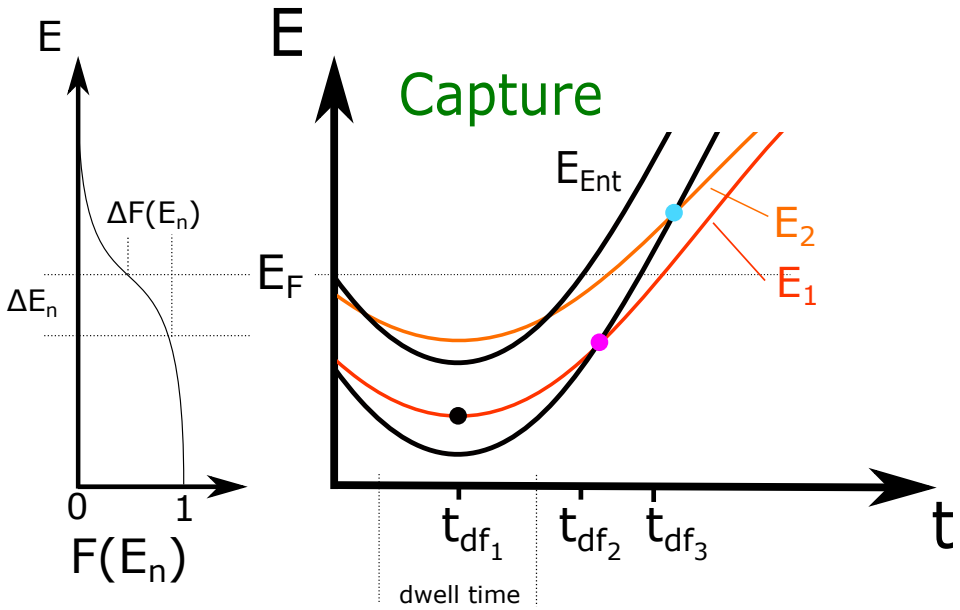

Figure 7.20: Diagram of the rise of energy levels in the dot during the pump cycle. The black, pink, and light blue circles highlight the time at which the dot is most coupled to the source.

In this model, the dot formation point is a function of the exit gate voltage. At very negative exit gate voltage the dot forms above the Fermi level, and at T = 0 K no electrons are captured. When the exit gate voltage is less negative the dot is formed earlier in the pumping cycle. The exit gate voltage associated with the dot forming at the Fermi level is the onset point in Figure 7.14. The time at which the dot forms, t_{df}, can be ascertained from its size at the Fermi level. Figure 7.20 shows three possible scenarios for the dot in the capture phase. Either it remains formed throughout the capture phase, (black circle), it forms when $E_{\mathrm{n}} < E_{\mathrm{F}}$, (pink circle), or it forms when $E_{\mathrm{n}} > E_{\mathrm{F}}$, (light blue circle). The requirements for each scenario depend on the entrance and exit gate voltages.

- Scenario 1 - The dot remains formed throughout the pump cycle; it does not get destroyed and reformed. This scenario occurs when the RF amplitude is small or the DC entrance gate voltage is more negative (near the capture line). The dot enters the Fermi sea empty, so $P_{\mathrm{n}}^{(1)}(0) = 0$; we use equation 7.30 to ascertain the probability of an electron being captured, $P_{\mathrm{n}}(t_{\mathrm{df_1}})$.

There is a possibility that the dot never captures an electron. As the dot is most strongly coupled when E_{n} is at a minimum; we model this as holding the dot at $E_{\mathrm{n}}^{\mathrm{min}}$ for a certain dwell time. The dwell time changes as a function of both frequency and exit gate voltage. If the frequency increases, the dwell time decreases. If exit gate voltage is more negative, the dot is more coupled to the source. The dwell time is given by $E_{\mathrm{B0n}}\tau$, where τ is a constant that maps E_{B0n} to the dwell time and is proportional to $1/f$, with units s/mV. We calculate the probability of capture by substituting these conditions into equation 7.30.

$$P_{\mathrm{n}}(t_{\mathrm{df_1}}) = F(E_{\mathrm{n}})(1 - e^{-\Gamma_{\mathrm{n}} E_{\mathrm{B0n}} \tau}) \tag{7.31}$$

To find the barrier height and Fermi distribution at $E_{\mathrm{n}}^{\mathrm{min}}$, we use the barrier height as $E_{\mathrm{Ent}}^{\mathrm{min}} - E_{\mathrm{n}}^{\mathrm{min}}$, and equation 7.13

$$\Gamma_{\mathrm{n}}(E_{\mathrm{n}}^{\mathrm{min}}) = W \exp\Big[-\beta (E_{\mathrm{Ent}}^{\mathrm{min}} - E_{\mathrm{n}}^{\mathrm{min}})^{3/2} \Big] \tag{7.32}$$

$$\Gamma_{\mathrm{n}}(E_{\mathrm{n}}^{\mathrm{min}}) = W \exp\Big[-\beta (\gamma E_{\mathrm{B0n}})^{3/2} \Big] \tag{7.33}$$

where γ relates E_{B0n} to the minimum barrier height.

The Fermi distribution at $E_{\mathrm{n}}^{\mathrm{min}}$ is also a function of E_{B0n}, as increasing E_{B0n} increases $E_{\mathrm{n}}^{\mathrm{min}}$.

$$F(E_{\mathrm{n}}^{\mathrm{min}}) = F(\eta + \gamma E_{B0n}) \tag{7.34}$$

where η is the energy difference between E_F and $E_{\mathrm{Ent}}^{\mathrm{min}}$.

- Scenario 2 - The dot is formed when $E_{\mathrm{n}} < E_{\mathrm{F}}$. This scenario occurs when the RF amplitude is large, or when the DC entrance gate voltage is less negative (near the ejection line). The dot is formed at $t_{\mathrm{df_2}}$ and the probability of capture is given by the Fermi distribution. Before the dot is formed, the probability of occupancy is clearly 0, $P_{\mathrm{n}}(t < t_{\mathrm{df_2}}) = 0$. At $t_{\mathrm{df_2}}$ the dot is most strongly coupled to the source, and $P_{\mathrm{n}}(t_{\mathrm{df_2}}) = F(E_{\mathrm{n}})$. As the dot rises, the tunnelling rate decreases exponentially. Once the tunnelling rate

becomes small, the dot does not have time to settle to the Fermi distribution at E_{n}. Given that $P_{\mathrm{n}}(t_{\mathrm{df}_2}) = F(E_{\mathrm{n}})$, we calculate the probability that an electron remains in the dot between t_{df_2} and t_0 by modelling the process as raising the dot by an energy ΔE_{n} and holding it there for a certain dwell time. As in scenario 1, the dwell time is given by $E_{\mathrm{B0n}}\tau$. We calculate the probability of capture by substituting these conditions into equation 7.30.

$$P_{\mathrm{n}}(t_{\mathrm{df}_2}) = F(E_{\mathrm{n}}) + (F(E_{\mathrm{n}} - \Delta E_{\mathrm{n}}) - F(E_{\mathrm{n}}))e^{-\Gamma_{\mathrm{n}} E_{\mathrm{B0n}}\tau} \tag{7.35}$$

$$= F(E_{\mathrm{n}}) + \Delta F(E_{\mathrm{n}})e^{-\Gamma_{\mathrm{n}} E_{\mathrm{B0n}}\tau} \tag{7.36}$$

$$= F(E_{\mathrm{n}})(1 + \frac{\Delta F(E_{\mathrm{n}})}{F(E_{\mathrm{n}})}e^{-\Gamma_{\mathrm{n}} E_{\mathrm{B0n}}\tau}) \tag{7.37}$$

- Scenario 3 - The dot is formed when $E_{\mathrm{n}} > E_{\mathrm{F}}$. This scenario occurs when the exit gate voltage is more negative (near the onset line). There is no physical mechanism by which the dot can capture an electron.

Different regions of the pump map will have a current made up of different contributions from each of the scenarios. We focus on Scenario 1 as it is the most plausible mechanism for the reduction of current at higher frequencies. Putting together the contributions of scenario 1 (equations 7.31, 7.33, 7.34) and the decay phase (equation 7.20) gives the final equation

$$\langle n \rangle = \sum_{\mathrm{n}}^{N} \underbrace{F(\eta + \gamma E_{B0n})}_{\text{thermal term}} \underbrace{\left(1 - \exp\left[W e^{-\beta(\gamma E_{\mathrm{B0n}})^{3/2}} E_{\mathrm{B0n}}\tau\right]\right)}_{\text{capture term}} \underbrace{\exp\left[- \frac{\alpha}{\beta\sqrt{E_{\mathrm{B0n}}}} e^{-\beta(E_{\mathrm{B0n}})^{3/2}}\right]}_{\text{decay term}} \tag{7.38}$$

Where $E_{\mathrm{B0n}} = eV_{\mathrm{Exit}} - eV_{\mathrm{n}}$.

While the model explains the shifts in the pump map lines with increased frequency and temperature, it does not adequately explain the degradation of plateau flatness. We use equation 7.38 to fit the amplitude, frequency, and temperature

dependent data, and use the description of the capture model to explain the shift in the pump map lines.

7.9 Amplitude analysis with temperature corrections

In this section we revisit the data discussed earlier in section 7.7 and apply the extended version of the model to it. Figure 7.21a shows the higher resolution data from Figure 7.6b fitted with equation 7.38. The capture term is kept constant as it is independent of amplitude. Figure 7.21b shows the fit of the shoulder, which is much better than in Figure 7.17b. The temperature term in equation 7.38 (a Fermi distribution) is a similar in form to the double negative exponential of the decay term. Because the old fitting equation 7.20 did not include this term, the reduction in the shoulder could not be fitted. Figure 7.21c shows the fit of the tail, which is similar to Figure 7.17c. α in Figure 7.17d is slightly smaller than in section 7.7, but retains the same amplitude dependence. To further emphasise the better fit, Figure 7.22 shows the residuals of the A = 200 mV data for equations 7.20 (red line) and 7.38 (black line). The black line has smaller residuals than the red line, most noticeably at the shoulder. This was true for all amplitudes. The temperature term directly improves the fitting at the shoulder, but as the fitting optimisation procedure is done on all the data, the extra freedom allowed for the fitting parameters by the inclusion of the temperature term means that the new fitting parameters will better fit the data for all of the data including the tail. This is most clearly seen in the reduction of the peak in residuals at -404 mV.

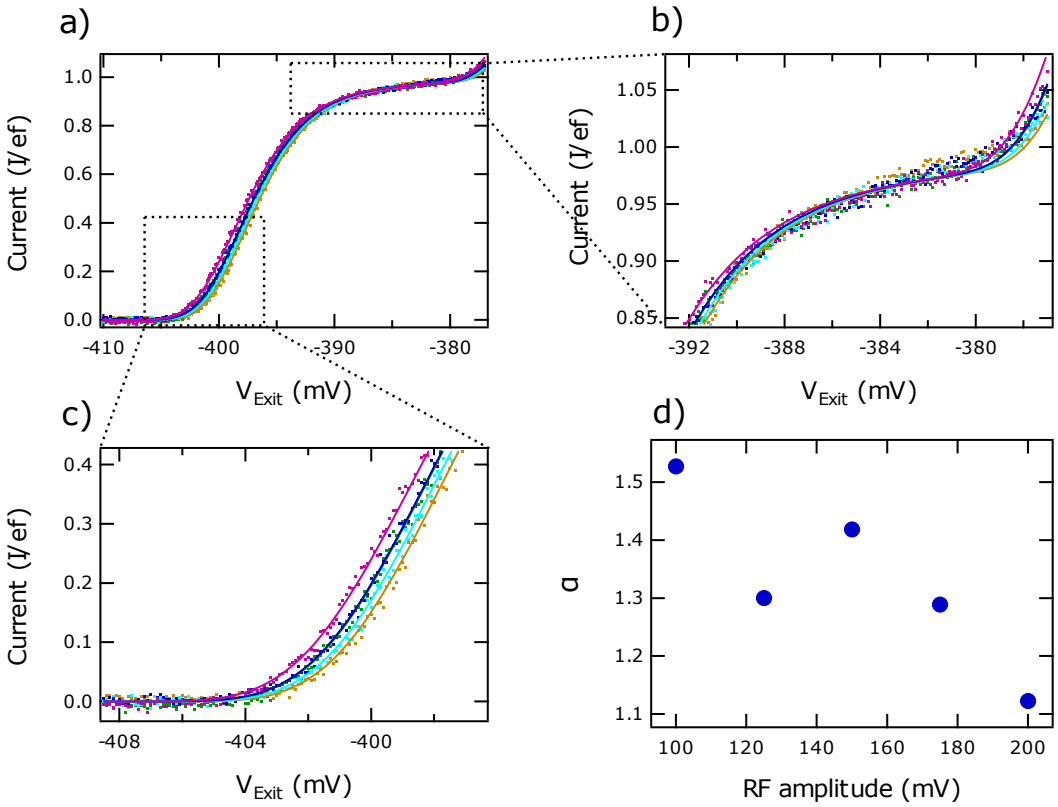

Figure 7.21: (a) A plot of current vs. exit gate voltage for different RF amplitudes with fittings overlaid. (b and c), respectively, a zoomed plot of the shoulder and tail. (d) The α fits for the different amplitudes.

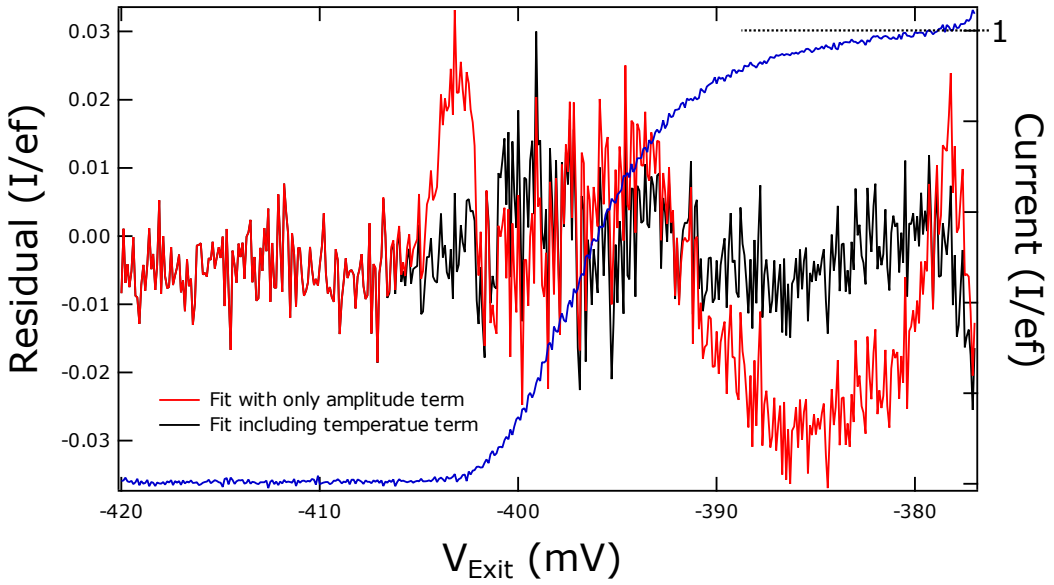

Figure 7.22: Plot of residuals vs. exit gate voltage showing the improvement of adding the temperature term near the shoulder. The residuals are overlaid on the data (blue line), to allow the position of the pump plateau to be seen.

Our model explains the shifts in the onset, capture and ejection lines of the amplitude-dependent data when amplitude is increased. The pump onset line remains fixed in V_{Exit}. This agrees with scenario 3, in which no dot is formed at more negative V_{Exit} past the pump onset line. The capture line gets pushed out indefinitely to more negative V_{Ent}. This occurs because V_{Ent} can be made more negative by the amount the amplitude has increased, with the dot still going below the Fermi level. The ejection line gets pushed out to less negative V_{Ent}. This occurs because V_{Ent} can be made less negative by the amount the amplitude has increased, with the maximum V_{Ent} unchanged.

At higher amplitudes, the slope of the pump onset line becomes more vertical. This is consistent with the model being based on the amount of time the dot spends in the capture phase. We attribute the slope of the pump onset line to a lag between the applied voltage and the energy levels in the dot, described in section 7.5. As V_{Ent} becomes more negative, the dot spends less time under the Fermi level and the current reduces until it never gets loaded with electrons when V_{Ent} is past pinch off. When amplitude is increased, the dot goes deeper below

the Fermi level, and the probability that electrons tunnel into it is higher.

In future work, we will revisit the amplitude dependence at much higher amplitudes. Physically, we think that at a higher amplitude the barrier rises more quickly, so there is less time for an electron to tunnel out and contribute to error.

7.10 Temperature analysis

In this section we investigate the effects of operating a pump at higher temperatures and discuss how such effects are incorporated in our model. Figure 7.23a shows the data from Figure 7.9b fitted with equation 7.38, with all parameters fixed except for η and T. At T = 1.6 K, the fit is good; but at higher temperatures it becomes less good. Figure 7.23b shows the temperature coefficient increases linearly with temperature (blue circles), as predicted by the model. Figure 7.23b shows η decreases linearly with temperature (black squares). The model predicts that η remains fixed, but generating good fits requires it to change. We are yet to fully understand the mechanism at work.

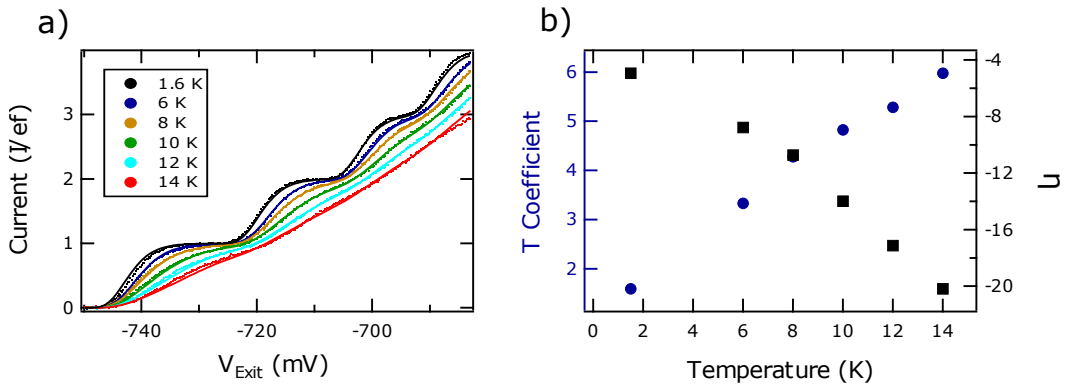

Figure 7.23: (a) A plot of current vs. V_{Exit} with fits overlaid. (b) A plot of the temperature coefficient and η vs. temperature

Our model explains the shifts in the pump map lines as temperature increases:

- Node 1 and the ejection line remain fixed in V_{Ent}; this is consistent with there being little thermal energy applied to the electrons relative to the

dot energy. If the electrons were thermally excited in the dot, the entrance barrier would not need to rise as high to eject electrons, and the ejection line would be pushed out to less negative V_{Ent}.

- Node 2 and the capture line shift to more negative V_{Ent}, from -320 mV $\rightarrow$ -360 mV, until T = 8 K, where they saturate; this is consistent with the dot being loaded with thermally excited electrons. At T = 0 K, there is no pumped current in the area below the capture line, where V_{Ent} is very negative, because the entrance barrier is high enough that the dot never goes below the Fermi level, so electrons never enter it. But, at higher temperatures, the electrons in the lead have sufficient thermal energy to tunnel into the dot and contribute to current.

  The smaller reduction in current near the ejection line compared with near the capture line is consistent with the different capture scenarios. Near the ejection line, the capture mechanism is scenario 2 in section 7.8, where E_{Ent} is so low that the dot forms in the capture phase and will capture an electron. Near the capture line, the capture mechanism is scenario 1 in section 7.8, where E_{Ent} is so high that the dot may be formed throughout the capture phase and not capture an electron.

- In contrast to the capture line, which shifts to more negative V_{Ent} at higher temperatures, the onset line remains fixed in V_{Exit}; considering the differences between the loading mechanisms of the lines, this is consistent with the model. The onset line is at V_{Exit}, where the dot forms at the Fermi level, corresponding to scenario 3 of the capture model. At more negative V_{Exit} the dot forms above the Fermi level; this is because thermally excited electrons would not remain in the dot while it is still strongly coupled to the lead. In contrast, the capture line is at V_{Ent}, where E_{Ent} dips below the Fermi level, scenario 1. At more negative V_{Ent}, E_{Ent} is above the Fermi level, but thermally excited electrons that enter the dot remain there as it is not as strongly coupled to the lead.

These results suggest that our model may offer a satisfactory account of the different loading mechanisms.

The model predicts that at an infinitely high temperature, the thermal term

in equation 7.38 is 1/2 for all values of V_{Exit}, so the pumped current will be half the ideal current. In future work, we will repeat our experiments at higher temperatures and identify where the current saturates. Also, we will test the robustness of the frequency dependence at different temperatures.

7.11 Frequency analysis

The frequency dependence of the pump current is harder to analyse than the amplitude and temperature dependence because of certain experimental limitations. The main limitation is the reduction in RF amplitude associated with increasing frequency. This reduction occurs because in passing high frequency RF signals down the probe, mismatches of impedance cause reflections in the RF line. At different frequencies, the attenuation on the RF signal changes unpredictably. In order to analyse the data, we shifted the line scans so their onset points were the same, (Figure 7.10 at -300 mV). Figure 7.24 shows the shifted data fitted with equation 7.38. The fits are close, and the model provides insight into the loading mechanisms in the capture phase. Figure 7.24d shows that τ is inversely proportional to frequency, as predicted by the capture model; this suggests that scenario 1 is a likely loading mechanism. Additionally, the capture model specifies that the frequency dependence of the pumped current is greatest near the capture line, when V_{Ent} is more negative or the RF amplitude is small.

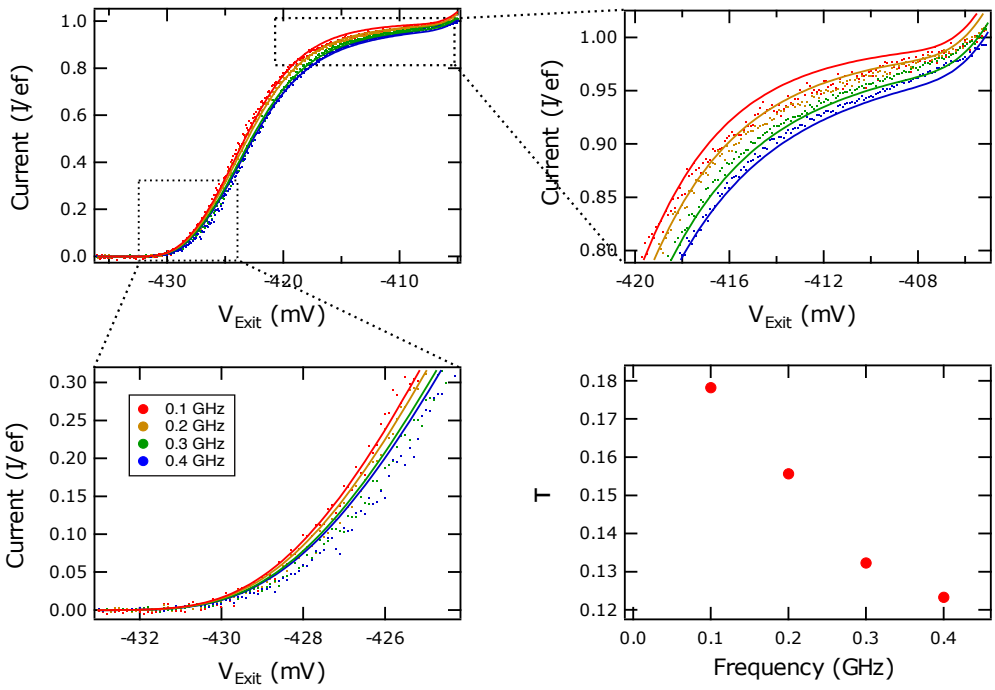

Figure 7.24: (a) A plot of current vs. exit gate voltage for different frequencies with fits overlaid. (b) A zoomed plot of the shoulder and (c) the tail. (d) The fitting values, τ, for the different frequencies.

The model explains why the pump onset line becomes less vertical as frequency is increased until $f = 0.5$ GHz, where it saturates. At low frequencies the onset line should be vertical, because the dot has time to reach equilibrium with the Fermi distribution, irrespective of E_{Ent}. At higher frequencies, the dot spends less time in the capture phase. Increasing frequency does not have a big effect on the capture probability near the ejection line, where E_{Ent} is very negative and the dot is strongly coupled to the lead, but it can have a big effect on the capture probability near the capture line, where E_{Ent} does not go low enough for the dot to couple strongly with the lead. Accordingly, the model predicts that the change in slope will be smaller for larger amplitudes and lower temperatures. In future work, we will test this by exploring the robustness of the frequency dependence at different amplitudes and temperatures.

7.12 Summary

We have developed a model from first principles that explains the shifts in the pump map lines, provides insight into the pumping mechanisms in different parts of the pump map, and predicts regions where the pump current is closest to the ideal current. Since 2DEG quantum pumps were developed in 2007, the only model of the pumped current has been the universal decay cascade model. While it is mathematically rigorous, it has a number of drawbacks. The main two, which are discussed in sections 7.4 and 7.7, are:

- It is based on initial conditions that make it difficult to assign physical meaning to its parameters because the derivation becomes too complicated. In contrast, our model is based on simpler initial conditions that make it relatively easy to assign physical meaning to its parameters.
- It is not designed to explain why pumping does not occur outside of the central pumping region. In contrast, our model is designed to explain those mechanisms, and contains variables that explicitly relate to the physical parameters: amplitude, temperature and frequency.

We observed that at higher RF amplitudes the capture line gets pushed out to more negative entrance gate voltages, the ejection line to less negative entrance gate voltages, and the onset line remains fixed in exit gate voltage. The model explains these observations and the reduction in deviation from the ideal pumped current. It fits these data moderately well, but changing the amplitude alone did not affect the fit of the shoulder; by including a temperature term, we improve the fit.

The model predicts a temperature dependence that is partly consistent with the data. At higher temperatures the onset line remains fixed and the deviation from the ideal pumped current is increased. The model is only partially consistent because fitting the data well requires an extra fitting parameter, η, which is not fixed for different temperatures. We observed that at higher temperatures the capture line gets pushed out to more negative entrance gate voltages, the ejection line remains fixed in entrance gate voltage, and the onset line remains fixed in

exit gate voltage. The model explains the different shifts in the capture and onset lines as being due to different capture scenarios; 1 (capture line) and 3 (onset line). The deviation from the ideal pump current near the capture line is greater than the deviation near the ejection line and, at higher temperatures, this difference becomes even greater. We observed that at higher frequencies the onset line becomes less vertical; this follows from the condition in scenario 1 when the dwell time is reduced. The model fits this well.

In addition to helping us understand the pumping mechanisms, the results will be useful when looking for high accuracy plateaus. Normally, high resolution line scans are taken at V_{Ent} in the middle of the pump map. But they should be taken near the ejection line, where the plateaus are closer to the ideal current.

7.13 Future work

Our future work plan is designed to better understand the capture process and improve and extend our model. The future work described in sections 7.9, 7.10, and 7.11 together require us to repeat the experiments using a broader range of RF amplitudes, temperatures, and frequencies. Towards improving and extending the model we plan to do the following:

- Examine whether the pumps have the same amplitude dependence at much lower temperatures, where errors due to thermal effects are reduced.
- Cover a wider range of amplitudes to see if the plateaus improve at higher RF amplitudes indefinitely or whether they start to degrade.
- Repeat the experiments described in section 7.3 using a broader range of RF amplitudes, to test whether the plateaus improve indefinitely or start to degrade.
- Repeat the experiments described in section 7.4 using a broader range of RF temperatures, and measure the pump current in a high-temperature limit.

- Take line scans in V_{Ent} at constant V_{Exit}, fit the model to them, and compare the tail and shoulder to line scans in V_{Exit} at constant V_{Ent}.
- Measure the frequency dependence of the pump at different amplitudes and temperatures to ascertain if increasing amplitude and decreasing temperature make the pump more robust to changes in frequency.

Finally, we will consider incorporating other factors that may degrade the plateau flatness that have not been discussed in the chapter.

- Local heating, where despite the dot being decoupled from the thermally broadened lead, it changes shape quickly enough that the electron gains energy within the dot and either back-tunnels or is thermally excited out.
- Thermally-broadened resonant tunnelling, where back-tunnelling into the source increases as the dot moves through the resonant tunnelling regime.
- Cross-talk between the gates, where the oscillating entrance gate causes the exit gate to oscillate.
- Magnetic field effects. We will attempt to expand the model to take into account the magnetic field dependence of the pump map.

While a full treatment of the problem would include these factors, their inclusion as part of this thesis would be inconsistent with the direction of this model. The aim in maintaining the simplicity of this model is to allow clear predictions and analysis of the data by deriving it from first principles and by including only a few key parameters.

Chapter 8

Summary

This chapter provides a brief summary of the chapters in this thesis. As quantum pump devices are so electrostatically sensitive, the majority of the work has been towards setting up a new lab in the LCN, and establishing processing and measurement steps that allow us to measure the devices. Respectively, these are outlined in sections 4.3 and 5.6. In an attempt to address the low yield of device, we experimented with pumps with no narrow etched channel, but these generated a large rectified current that swamped out any pumped current. We investigated the possible origins of this rectified current in chapter 6 and compared our model to data taken at different amplitudes, frequencies, and series resistance. We then investigated the viability of using these parameters, and additional circuit components, to suppress rectified current without altering pumped current. After ruling out pumped devices with no etched channel, we returned to etched channel pumps and investigated the physical mechanisms behind the pump current. We investigated how pump current changes as a function of RF amplitude, temperature, and frequency. This lead to the development of a new model to describe pumped current from first principles in chapter 7. Below are the summaries of the key points identified by these chapters.

8.1 Failure modes

Devices fail when they no longer conduct through the channel or the gates blow up. Non-conducting channels result from problems with doing a narrow and shallow etch into the AlGaAs layer of the wafer. Surface roughness in the shallow etch contributes to non-conducting channels. This roughness did not depend heavily on the etch solution; rather, it is a result of bunching of Al, which etches quicker then GaAs during wafer growth. Adding surfactant to the shallow etch solution often created a thin film of surfactant that shielded the etched region from the etch solution. This thin film could not be removed with RF-ashing or HF. Even without surfactant, the edges of the shallow etch were often rough. This was due to water beading in the small features from the HCL dip. We recommend drying the device with N_2 before doing the shallow etch. The gates were problematic because of proximity of the gates to each other (often < 100 nm) and the shallow etch they had to climb. Getting the thickness of the deposited metal for the gates correct was crucial: too thin and they would not climb the shallow etch, too thick and they would short. The mechanism by which gates blow up is not well understood, but it is probable that is due to the breakdown voltage of the dielectric between the gates; they blow up when a static charge or voltage spike is introduced to them. We successfully experimented with protecting the gates with an oxide layer and cross-linked PMMA. The added protection made them much less sensitive to static charges from handling, but voltage spikes still blew them up.

Voltage spikes reach the device when the measurement setup is not set up correctly to avoid ground loops, and when the setup does not provide adequate protection for the device. Towards this, a lot of work was done to isolate the measurement circuit from the cryostat ground and the RF-source ground. In addition, low pass filters were added to the gate lines, and later the Ohmic lines, to protect the device. However, filters cannot be used on RF lines because they attenuate RF signals. Most frequently, devices blew up only when the RF line was connected. An inner/outer DC block prevents a ground loop from the RF source, and the sample holder we developed helps with a good RF connection to the device. The development of this sample holder has been one of the biggest factors in keeping devices working through to measurement.

8.2 Rectified current

Rectified current has been observed by a few groups working with RF, but it is not well documented in the literature. In experiments where rectified current is observed but not intrusive to the experiment it is often noted but not investigated further. In our attempts to develop a pump without a narrow etched channel, rectified current became intrusive because it swamped any quantised pumped current. We developed a model for the rectified current, and made a new device with a central gate and no narrow etched channel that most closely resembled our modelled circuit. We then measured rectified current, with zero source-drain bias, at different RF amplitudes, frequencies, and series resistances. We compared simulations from our model to the measured data and showed that they agree well over certain ranges of the parameters. We then considered if we could take advantage of any of the parameters to suppress rectified current and concluded that RF amplitude and frequency are not good parameters to use, as they also affect pump current. Increasing series resistance suppressed rectified current, and is used to reveal an extra quantised plateau in Figure 6.14. In a 2-gate pump device, the rectified current is much more complex and cannot be modelled using our circuit. We experimented with using a low pass filter on the Ohmic lines to suppress rectified current and found that it had the largest impact. Finally, we experimented with applying a magnetic field and found it suppresses rectified current.

8.3 Pumping model

Once we resolved the problems with the narrow etched channel we investigated the pumping mechanism and why it changes in the different regions of the pump map. We developed a model that provides insight into the possible reasons why there is quantised pump current in the region of entrance and exit gate voltages bound by the pump map lines (the capture, onset, and ejection lines) but there is no current outside of this area. We took pump maps at different RF amplitudes, temperatures, and frequencies, and measured the shifts in the pump map lines. One key point is that for increased temperature, the onset line shifts to less

negative exit gate voltages but the capture line shifts to more negative entrance gate voltages. The difference in the way the lines shift is surprising and suggests a different pumping mechanism at the onset and capture lines. Our model addresses this with different capture scenarios at the two lines. Also, unlike the UDC model, our model is derived using physically pertinent variables that carry through to the final fitting equation. We have developed the model sufficiently to fit it to the data and observe the correct shift in the parameters relating to the RF amplitude, temperature, and frequency. The temperature term required an additional term, η, to fit the temperature data. However, this term does not fit in the model satisfactorily, so further work is required to develop it. Despite this, it is the only model that explains the RF amplitude, temperature, and frequency dependence of the pump maps. We hope it provides a good framework on which a more complete model can be built.

Chapter 9

Additional Future work

The rectified current model in chapter 6 and the pumping model in chapter 7 require additional work to verify and expand on them. Respectively, the future work for these chapters are listed in sections 6.9 and 7.13. The work has been presented in a such a way that it is streamlined and develops the narrative for this thesis, but there is a lot of additional future work that has been started, which does not necessarily fit into the thesis narrative. There are 3 areas we have identified that naturally follow on from this work; they are suggestions for work that has not been started and descriptions of work that has been started but is not developed enough to include in the main thesis:

1. Pumping in a multi-gate dot pump.
2. Electron interferometry.
3. Pumping in other materials that show Coulomb blockade.

9.1 Pumping in a multi-gate dot pump

The spit-gate device used throughout this work has been used as either a 3-gate split-gate pump, pumping to the right, or a 2-gate normal pump, pumping to the left. As an initial step towards integrating devices, we operated the device as

4-gated pump. Figure 9.1 shows a schematic of the measurement setup. An RF signal is applied to the entrance gate (red) and DC voltages are applied to the middle and exit gates (green). With a dot in a double dot setup we could transfer electrons from a dynamic quantum dot on the left to a static quantum dot on the right. The locations of the dots and the direction of pumping are shown in yellow. To operate the pump, the split-gate was held in the far pinch-off regime (≈ -950 mV), the entrance gate had a DC component in the far pinch-off regime (≈ -850 mV), and an AC component large enough to pump electrons, but the middle gate was held at a much lower negative gate voltage (≈ -150 mV). Assuming the split gate does not pull up the middle gate past pinch-off, this suggests that 2 dots form a hybrid double dot.

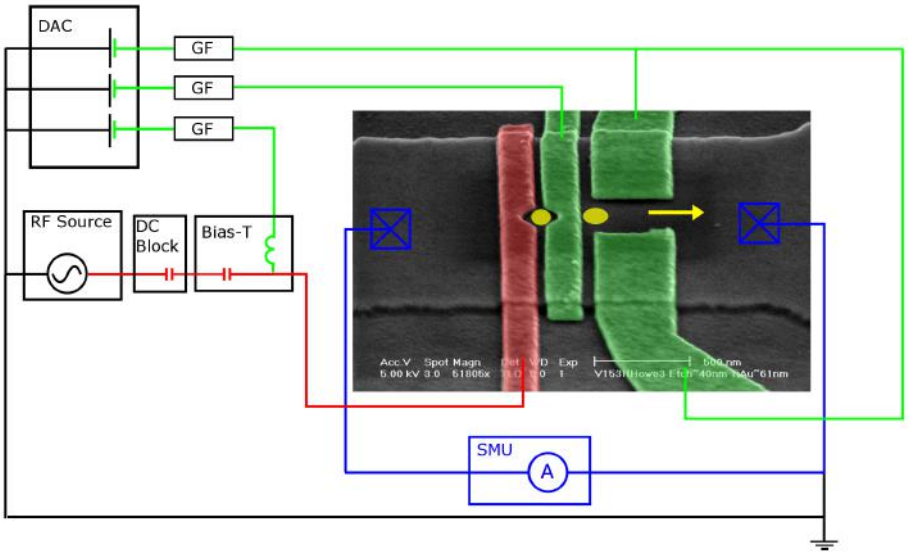

Figure 9.1: A schematic of the measurement setup used in the multi-gate pump.

Initial tests have produced plateau-like features at much greater currents than $1ef$. Figure 9.2 shows current as a function of middle-gate voltage. Though we do not yet know the mechanism behind these plateau-like features, we can speculate as to what they might be by comparing them to 1D conductance measurements and Coulomb blockade oscillations. These plateau-like features are unlike those usually found in 1D measurements and unlike most Coulomb blockade oscillations. The experiment was done in a helium dewar, initially at 4.2 K. Coulomb oscillations in GaAs is usually only seen at ≈ 300 mK, so we repeated the measurements above the helium level, cooling via the helium boil off only,

and found no change in the measured current.

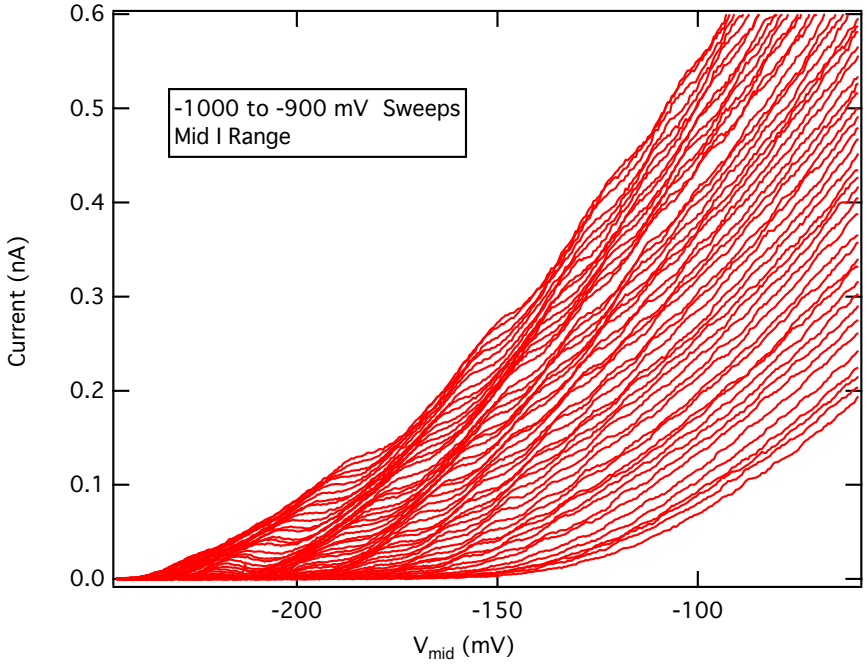

Figure 9.2: A plot of current vs. V_{mid} for different values of exit-gate voltage.

Figure 9.3 shows a colourmap of dI/dV vs. middle and exit gate voltage. There are 17 visible plateaus, which is unusual for a device at temperatures much higher than 4.2 K.

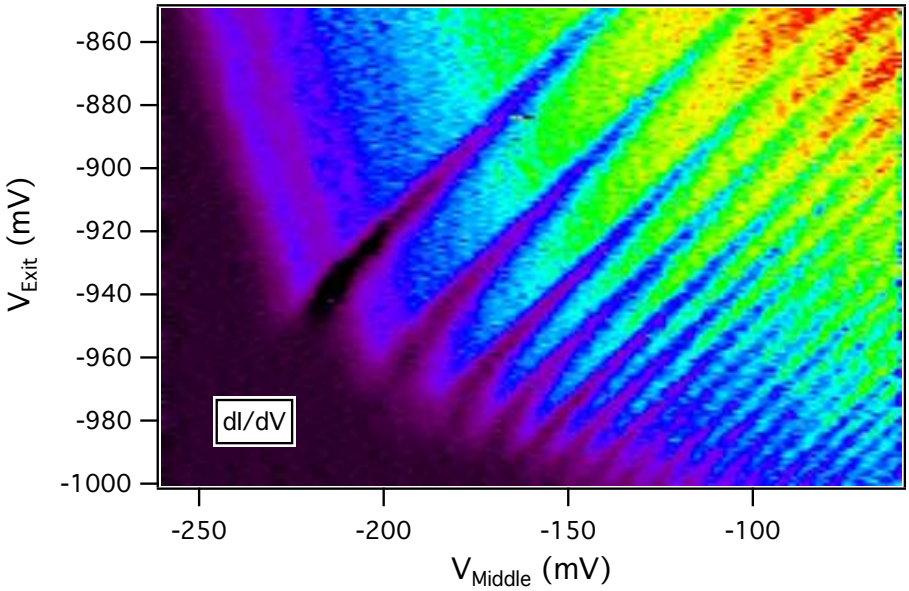

Figure 9.3: A differential colourmap of current vs. mid gate voltage and exit gate voltage

9.2 Electron interferometry

The narrow-etch channel is used to confine the electrons and suppress rectified current. Beyond this, the narrow-etch channel can be used to create separate electron paths that later recombine for interferometry experiments. The most common of these is the Aharanov-Bohm effect. When an electron propagates around a closed loop (AB-ring) in the presence of a magnetic flux, it experiences a phase change. If electrons travel through a quantum wire that splits into 2 channels, they have an equal probability of travelling through one or other of the channels; the electrons later recombine. Similarly, the wave function splits into two coherent partial wave functions that recombine when the wires meet again. If there is an enclosed magnetic flux, the phase change experienced by these partial wave functions is different; accordingly, they will combine either constructively or destructively depending on the enclosed magnetic flux Φ.

$$\Delta\phi = 2\pi\frac{e}{h}\oint \mathbf{A}\cdot\mathbf{dl} = \mathbf{2\pi\frac{e}{h}}\int_{\mathbf{S}}\mathbf{B}\cdot\mathbf{dS} = \mathbf{2\pi\frac{e}{h}\Phi} \tag{9.1}$$

By loading an AB-ring with two electrons from a quantum pump, the electron interference may change due to electrons being entangled in the dot. In addition to the AB effect, there are many other possibilities for electrical analogues of optical interferometry experiments. These include the Hanbury-Brown-Twiss (HBT) effect [62], the Hong-Ou-Mandel (HOM) effect [63], and Mach-Zehnder interferometry [64]. Figure 9.4 shows a schematic of a device for a HOM experiment. It consists of a double dot split-gate pump either side of a tunnelling barrier. In a perpendicular magnetic field, electrons leaving the pumps will follow chiral quasi-1D edge states that squeeze them together at the barrier. If the barrier is set to be 50% transparent, respectively electrons should bunch or anti-bunch depending on whether they form an entangled pair (bosons) or are pumped individually (fermions).

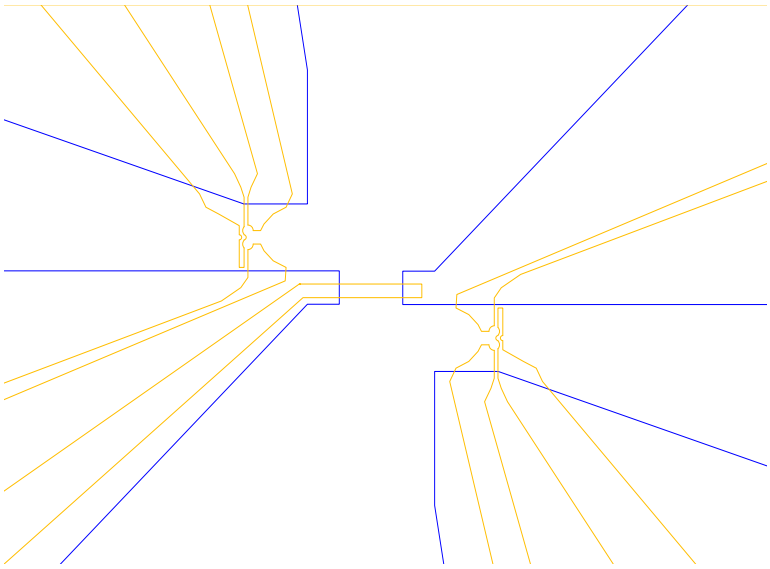

Figure 9.4: A schematic of the device proposed for an electrical HOM experiment, sowing the mesa etch (blue) and the pump and barrier gates (yellow).

9.3 Pumping in other materials

Any gated device that shows Coulomb blockage as a function of gate voltage should be usable as a quantum pump. While the pumping occurs in a more pinched-off regime than Coulomb blockade, the robustness of Coulomb blockade measurements may be an indicator for the robustness of the quantum pumps.

Beyond GaAs, we plan to explore different types of Si devices (etched wires and dropcast nano-fibers), pumping holes for its higher effective mass [65], and InAs for its spin-orbit properties [66]. The processing, protective steps, and measurement setup developed in this work are applicable to experiments in these other materials.

Appendix

Processing steps for EBL-defined pumps

Date: _____

Wafer _____ , Mobility _____ , n Dark _____

Cleave, Clean, Optical Mesa and Ohmics

1. Cleave sample:

   Use scriber, note direction of major axis.

2. Clean sample:

   $$\text{Acetone} \underset{5\text{ min}}{\text{ ultrasonic}} \rightarrow \underset{1\text{ min}}{\text{IPA}} \rightarrow N_2 \text{ Dry}$$

3. Mesa expose and develop:

   $$\text{pre-bake } 125^\circ\text{C} \underset{5\text{ min}}{\rightarrow} \text{Microposit 1805} \underset{45\text{ sec }5500\text{ rpm}}{\rightarrow} \text{bake } 90^\circ\text{C} \underset{2\text{ min}}{\Rightarrow} \text{Mesa expose} \underset{3.5\text{ sec}}{\Rightarrow} \underset{\text{FB + 30 sec}}{\text{MF 319}}$$
   $$\rightarrow \underset{30\text{ sec}}{\text{DI water}} \rightarrow N_2 \text{ Dry}$$

4. Mesa etch:

   $$\underset{40\text{ sec (optional)}}{\text{RF ash}} \Rightarrow \text{Dektak}\_\_\_\_\_ \Rightarrow$$
   $$\underset{15\text{ sec}}{HCL{:}H_2O\ (1{:}5)} \rightarrow \underset{15\text{ sec}}{\text{DI water}} \rightarrow \underset{45\text{ sec}}{H_2SO_4{:}H_2O_2{:}H_2O\ (1{:}8{:}120)} \rightarrow \underset{20\text{ sec}}{\text{DI water}} \rightarrow$$
   $$N_2 \text{ Dry} \Rightarrow \text{Dektak}\_\_\_\_\_ \underset{2\text{ min}}{\Rightarrow \text{Acetone}} \underset{1\text{ min}}{\rightarrow \text{IPA}} \rightarrow N_2 \text{ Dry} \Rightarrow \text{Dektak}\_\_\_\_\_$$

5. Ohmics expose and develop:

$\underset{40\text{ sec (optional)}}{\text{RF ash}} \Rightarrow \text{HCL:H}_2\text{O (1:5)} \underset{15\text{ sec}}{\rightarrow} \text{DI water} \underset{15\text{ sec}}{\rightarrow} \text{N}_2\text{ Dry} \Rightarrow \underset{5\text{ min}}{\text{pre-bake 125°C}}$
$\rightarrow \underset{45\text{ sec 5500 rpm}}{\text{Microposit 1813}} \rightarrow \underset{2\text{ min}}{\text{bake 90°C}} \Rightarrow \underset{6.5\text{ sec}}{\text{Ohmics expose}} \Rightarrow \underset{1\text{ min}}{\text{Chlorobenzeze}} \rightarrow$
$\text{N}_2\text{ Dry} \rightarrow \underset{\text{FB + 30 sec}}{\text{MF 319}} \rightarrow \underset{30\text{ sec}}{\text{DI water}} \rightarrow \text{N}_2\text{ Dry}$

6. Ohmics evaporation:

   $\underset{40\text{ sec (optional)}}{\text{RF ash}} \Rightarrow \text{HCL:H}_2\text{O (1:5)} \underset{15\text{ sec}}{\rightarrow} \text{DI water} \underset{15\text{ sec}}{\rightarrow} \text{N}_2\text{ Dry} \Rightarrow \text{Evaporate AuGeNi (140 nm)} \Rightarrow$

   $\text{Acetone} \underset{1\text{hour}}{\rightarrow} \underset{5\text{ min}}{\text{IPA}} \rightarrow \text{Blow with pipette or squeeze Acetone if necessary} \rightarrow \text{N}_2\text{ Dry}$

7. Ohmics anneal:

   RTA, profile KEN01: 30 sec at 220 °C, 80 sec at 430 °C, 30 sec at 220 °C; do a learn cycle before annealing real sample. Check resistance with the probe station.

Resistance Light				
Resistance Dark				
Resistance Dark LN2				

EBL Mesa and Gates

1. EBL Mesa prep:

   $\underset{40\text{ sec (optional)}}{\text{RF ash}} \Rightarrow \text{HCL:H}_2\text{O (1:5)} \underset{15\text{ sec}}{\rightarrow} \text{DI water} \underset{15\text{ sec}}{\rightarrow} \text{N}_2\text{ Dry} \Rightarrow \underset{20\text{ min}}{\text{Oven bake 150°C}}$
   $\Rightarrow \underset{60\text{ sec 5500 rpm}}{\text{PMMA 950K A4 neat}} \rightarrow \underset{10\text{ min}}{\text{bake 150°C}}$

2. Submit EBL Mesa

3. EBL Mesa develop and etch:

   Scribe one row of devices for calibration

MIBK:IPA:MEK (5:15:1) $\rightarrow$ IPA (8 sec) $\rightarrow$ N_2 Dry $\Rightarrow$ RF ash (10 sec (optional)) $\Rightarrow$ HCL:H_2O (1:5) (15 sec) $\rightarrow$ DI water (15 sec) $\rightarrow$ H_2SO_4:H_2O_2:H_2O (1:8:120) (8 sec) $\rightarrow$ DI water (20 sec) $\rightarrow$ N_2 Dry $\Rightarrow$ Acetone (2 min) $\rightarrow$ IPA (1 min) $\rightarrow$ N_2 Dry $\Rightarrow$ AFM/SEM

Time				
Depth				
Resistance Light				
Resistance Dark				
Resistance Dark LN2				

4. EBL Gates prep:

   RF ash (40 sec (optional)) $\Rightarrow$ HCL:H_2O (1:5) (15 sec) $\rightarrow$ DI water (15 sec) $\rightarrow$ N_2 Dry $\Rightarrow$ Oven bake 150°C (20 min) $\Rightarrow$ PMMA 100K A6 neat (60 sec 8000 rpm) $\rightarrow$ bake 180°C (3 min) $\rightarrow$ PMMA 950K A11:MIBK (1:5) (60 sec 8000 rpm) $\rightarrow$ bake 125°C (3 min) $\Rightarrow$ Oven bake 150°C (10 min)

5. Submit EBL Gates

6. EBL Gates develop and evaporate:

   MIBK:IPA:MEK (5:15:1) $\rightarrow$ IPA (8 sec) $\rightarrow$ N_2 Dry $\Rightarrow$ Evaporate Ti/Au (10 nm/40 nm) $\Rightarrow$ Acetone (overnight in sealed bottle) $\rightarrow$ IPA (5 min) $\rightarrow$ Blow with pipette or sqeeze Acetone if necesarry $\rightarrow$ N_2 Dry

Optical Gates

1. Gates expose and develop:

   pre-bake 125°C (5 min) $\rightarrow$ Microposit 1813 (45 sec 5500 rpm) $\rightarrow$ bake 90°C (2 min) $\Rightarrow$ Ohmics expose (6.5 sec) $\Rightarrow$ Chlorobenzeze (1 min) $\rightarrow$ N_2 Dry $\rightarrow$ MF 319 (FB + 30 sec) $\rightarrow$ DI water (30 sec) $\rightarrow$ N_2 Dry

2. Gates evaporation:

$$\underset{40\text{ sec (optional)}}{\text{RF ash}} \Rightarrow \text{HCL:H}_2\text{O (1:5)} \rightarrow \underset{15\text{ sec}}{\text{DI water}} \rightarrow \text{N}_2\text{ Dry} \Rightarrow$$
$$\text{Evaporate Ti/Au (20 nm/70 nm)} \Rightarrow \underset{\text{overnight in sealed bottle}}{\text{Acetone}} \rightarrow \underset{5\text{ min}}{\text{IPA}}$$
$$\rightarrow \text{Blow with pipette or squeeze Acetone if necessary} \rightarrow \text{N}_2\text{ Dry}$$

Package

Bibliography

[1] S. P. Giblin, M. Kataoka, J. D. Fletcher, P. See, T. J. B. M. Janssen, J. P. Griffiths, G. A. C. Jones, I. Farrer, and D. A. Ritchie, "Towards a quantum representation of the ampere using single electron pumps," *Nat Commun*, vol. 3, p. 930, Jul 2012.

[2] "http://physics.nist.gov/cuu/units/history.html,"

[3] I. M. Mills, P. J. Mohr, T. J. Quinn, B. N. Taylor, and E. R. Williams, "Redefinition of the kilogram, ampere, kelvin and mole: a proposed approach to implementing cipm recommendation 1 (ci-2005)," *Metrologia*, vol. 43, no. 3, p. 227, 2006.

[4] K. Likharev and A. Zorin, "Theory of the bloch-wave oscillations in small josephson junctions," *Journal of Low Temperature Physics*, vol. 59, no. 3-4, pp. 347–382, 1985.

[5] J. E. Mooij and Y. V. Nazarov, "Superconducting nanowires as quantum phase-slip junctions," *Nat Phys*, vol. 2, pp. 169–172, Mar. 2006.

[6] J. H. Davies, *The Physics of Low-dimensional Semiconductors: An Introduction*. Cambridge University Press, 1998.

[7] D. Ferry, S. Goodnick, and J. Bird, *Transport in Nanostructures*. Transport in Nanostructures, Cambridge University Press, 2009.

[8] C. Kittel, *Introduction to Solid State Physics*. Wiley, 2004.

[9] http://britneyspears.ac/physics/dos/dos.html

[10] L. Mino, G. Agostini, E. Borfecchia, D. Gianolio, A. Piovano, E. Gallo, and C. Lamberti, "Low-dimensional systems investigated by x-ray absorption spectroscopy: a selection of 2d, 1d and 0d cases," *Journal of Physics D: Applied Physics*, vol. 46, no. 42, p. 423001, 2013.

[11] "'http://www.clarkson.edu/camp/reports_publications/march08/page4.html',"

[12] D. Neamen, *Semiconductor Physics and Devices: Basic Principles*. McGraw-Hill international edition, McGraw-Hill, 2011.

[13] D. Vaid, "Quantum Hall Effect and Black Hole Entropy in Loop Quantum Gravity," 2012.

[14] "http://commons.wikimedia.org/wiki/file:sketch_energy_edge_channels.svg,"

[15] "http://kouwenhovenlab.tudelft.nl/wp-content/uploads/2011/10/60-electron-transport.pdf,"

[16] V. Kashcheyevs and B. Kaestner, "Universal decay cascade model for dynamic quantum dot initialization," *Physical review letters*, vol. 104, no. 18, p. 186805, 2010.

[17] V. Kashcheyevs and J. Timoshenko, "Modeling of a tunable-barrier non-adiabatic electron pump beyond the decay cascade model," in *Precision Electromagnetic Measurements (CPEM 2014), 2014 Conference on*, pp. 536–537, IEEE, 2014.

[18] V. Kashcheyevs and J. Timoshenko, "Quantum fluctuations and coherence in high-precision single-electron capture," *Physical review letters*, vol. 109, no. 21, p. 216801, 2012.

[19] V. Kashcheyevs, "Derivation of the universal decay cascade distribution," *arXiv preprint arXiv:1412.3024*, 2014.

[20] B. Kaestner and V. Kashcheyevs, "Non-adiabatic quantized charge pumping with tunable-barrier quantum dots," *arXiv preprint arXiv:1412.7150*, 2014.

[21] D. J. Thouless, "Quantization of particle transport," *Phys. Rev. B*, vol. 27, pp. 6083–6087, May 1983.

[22] R. E. Prange, D. R. Grempel, and S. Fishman, "Solvable model of quantum motion in an incommensurate potential," *Phys. Rev. B*, vol. 29, pp. 6500–6512, Jun 1984.

[23] T. A. Fulton and G. J. Dolan, "Observation of single-electron charging effects in small tunnel junctions," *Phys. Rev. Lett.*, vol. 59, pp. 109–112, Jul 1987.

[24] P. Delsing, K. K. Likharev, L. S. Kuzmin, and T. Claeson, "Effect of high-frequency electrodynamic environment on the single-electron tunneling in ultrasmall junctions," *Phys. Rev. Lett.*, vol. 63, pp. 1180–1183, Sep 1989.

[25] P. Delsing, K. K. Likharev, L. S. Kuzmin, and T. Claeson, "Time-correlated single-electron tunneling in one-dimensional arrays of ultrasmall tunnel junctions," *Phys. Rev. Lett.*, vol. 63, pp. 1861–1864, Oct 1989.

[26] L. J. Geerligs, V. F. Anderegg, P. A. M. Holweg, J. E. Mooij, H. Pothier, D. Esteve, C. Urbina, and M. H. Devoret, "Frequency-locked turnstile device for single electrons," *Phys. Rev. Lett.*, vol. 64, pp. 2691–2694, May 1990.

[27] L. P. Kouwenhoven, A. T. Johnson, N. C. van der Vaart, C. J. P. M. Harmans, and C. T. Foxon, "Quantized current in a quantum-dot turnstile using oscillating tunnel barriers," *Phys. Rev. Lett.*, vol. 67, pp. 1626–1629, Sep 1991.

[28] M. W. Keller, J. M. Martinis, N. M. Zimmerman, and A. H. Steinbach, "Accuracy of electron counting using a 7-junction electron pump," *Applied Physics Letters*, vol. 69, no. 12, pp. 1804–1806, 1996.

[29] M. W. Keller, A. L. Eichenberger, J. M. Martinis, and N. M. Zimmerman, "A capacitance standard based on counting electrons," *Science*, vol. 285, no. 5434, pp. 1706–1709, 1999.

[30] J. M. Shilton, D. R. Mace, V. I. Talyanskii, Y. Galperin, M. Y. Simmons, M. Pepper, and et al., "On the acoustoelectric current in a one-dimensional channel," *J. Phys.: Condens. Matter*, vol. 8, no. 24, p. L337, 1996.

[31] J. Shilton, D. Mace, V. Talyanskii, M. Simmons, M. Pepper, A. Churchill, and D. Ritchie, "Experimental study of the acoustoelectric effects in gaas-algaas heterostructures," *Journal of Physics: Condensed Matter*, vol. 7, no. 39, p. 7675, 1995.

[32] J. Shilton, V. Talyanskii, M. Pepper, D. Ritchie, J. Frost, C. Ford, C. Smith, and G. Jones, "High-frequency single-electron transport in a quasi-one-dimensional gaas channel induced by surface acoustic waves," *Journal of Physics: Condensed Matter*, vol. 8, no. 38, p. L531, 1996.

[33] J. Ebbecke, N. Fletcher, F. Ahlers, A. Hartland, and T. Janssen, "Study of the limitations of the quantized acoustic current technique at ptb and npl," *IEEE Trans. Instrum. Meas.*, 2003.

[34] J. Ebbecke, G. Bastian, M. Blöcker, K. Pierz, and F. Ahlers, "Enhanced quantized current driven by surface acoustic waves," *Applied Physics Letters*, vol. 77, no. 16, pp. 2601–2603, 2000.

[35] A. Fujiwara, N. M. Zimmerman, Y. Ono, and Y. Takahashi, "Current quantization due to single-electron transfer in si-wire charge-coupled devices," *Applied Physics Letters*, vol. 84, no. 8, pp. 1323–1325, 2004.

[36] M. D. Blumenthal, B. Kaestner, L. Li, S. Giblin, T. J. B. M. Janssen, M. Pepper, D. Anderson, G. A. C. Jones, and D. A. Ritchie, "Gigahertz quantized charge pumping," *Nature Physics*, vol. 3, pp. 343–347, 2007.

[37] K. Flensberg, Q. Niu, and M. Pustilnik, "Nonadiabaticity and single-electron transport driven by surface acoustic waves," *Phys. Rev. B*, vol. 60, pp. R16291–R16294, Dec 1999.

[38] A. Fujiwara, K. Nishiguchi, and Y. Ono, "Nanoampere charge pump by single-electron ratchet using silicon nanowire metal-oxide-semiconductor field-effect transistor," *Applied Physics Letters*, vol. 92, no. 4, p. 042102, 2008.

[39] B. Kaestner, V. Kashcheyevs, S. Amakawa, M. Blumenthal, L. Li, T. Janssen, G. Hein, K. Pierz, T. Weimann, U. Siegner, *et al.*, "Single-parameter nonadiabatic quantized charge pumping," *Physical Review B*, vol. 77, no. 15, p. 153301, 2008.

[40] B. Kaestner, C. Leicht, V. Kashcheyevs, K. Pierz, U. Siegner, and H. Schumacher, "Single-parameter quantized charge pumping in high magnetic fields," *Applied Physics Letters*, vol. 94, no. 1, p. 012106, 2009.

[41] S. Wright, M. Blumenthal, M. Pepper, D. Anderson, G. Jones, C. Nicoll, and D. Ritchie, "Parallel quantized charge pumping," *Physical Review B*, vol. 80, no. 11, p. 113303, 2009.

[42] S. J. Wright, M. D. Blumenthal, G. Gumbs, A. L. Thorn, M. Pepper, T. J. B. M. Janssen, S. N. Holmes, D. Anderson, G. A. C. Jones, C. A. Nicoll, and D. A. Ritchie, "Enhanced current quantization in high-frequency electron pumps in a perpendicular magnetic field," *Phys. Rev. B*, vol. 78, p. 233311, Dec 2008.

[43] J. Cunningham, V. I. Talyanskii, J. M. Shilton, M. Pepper, A. Kristensen, and P. E. Lindelof, "Single-electron acoustic charge transport on shallow-etched channels in a perpendicular magnetic field," *Phys. Rev. B*, vol. 62, pp. 1564–1567, Jul 2000.

[44] B. Kaestner, V. Kashcheyevs, G. Hein, K. Pierz, U. Siegner, and H. W. Schumacher, "Robust single-parameter quantized charge pumping," *Applied Physics Letters*, vol. 92, no. 19, p. 192106, 2008.

[45] T. Janssen and A. Hartland, "Accurate measurement of currents generated by single electrons transported in a one-dimensional channel," *Science, Measurement and Technology, IEE Proceedings*, vol. 147, no. 4, pp. 174–176, 2000.

[46] J. D. Fletcher, P. See, H. Howe, M. Pepper, S. P. Giblin, J. P. Griffiths, G. A. C. Jones, I. Farrer, D. A. Ritchie, T. J. B. M. Janssen, and M. Kataoka, "Clock-controlled emission of single-electron wave packets in a solid-state circuit," *Phys. Rev. Lett.*, vol. 111, p. 216807, Nov 2013.

[47] D. Taubert, C. Tomaras, G. J. Schinner, H. P. Tranitz, W. Wegscheider, S. Kehrein, and S. Ludwig, "Relaxation of hot electrons in a degenerate two-dimensional electron system: Transition to one-dimensional scattering," *Phys. Rev. B*, vol. 83, p. 235404, Jun 2011.

[48] J. Waldie, P. See, V. Kashcheyevs, J. P. Griffiths, I. Farrer, G. A. C. Jones, D. A. Ritchie, T. J. B. M. Janssen, and M. Kataoka, "Measurement and control of electron wave packets from a single-electron source," *ArXiv e-prints*, Mar. 2015.

[49] S. Wright, "Quantised charge pumping in a perpendicular magnetic field," 2010.

[50] "http://www.npl.co.uk/publications/science-posters/quantum-spillage-in-a-single-electron-pump,"

[51] M. McCluskey and E. Haller, *Dopants and Defects in Semiconductors*. Taylor & Francis, 2012.

[52] C. Wadhwa, *High Voltage Engineering*. New age, New Age International (P) Limited, 2007.

[53] S. Adachi, "Gaas, alas, and alxga1- xas: Material parameters for use in research and device applications," *Journal of Applied Physics*, vol. 58, no. 3, pp. R1–R29, 1985.

[54] "https://www.london-nano.com/research-and-facilities/themes/techniques/molecular-beam-epitaxy,"

[55] "http://cnx.org/contents/0b2614e4-aa98-49c1-bf50-1db3ee3c5ecd@2/molecular_beam_epitaxy,"

[56] "http://large.stanford.edu/courses/2007/ph210/bert2/,"

[57] L. DiCarlo, C. M. Marcus, and J. S. Harris, "Photocurrent, rectification, and magnetic field symmetry of induced current through quantum dots," *Phys. Rev. Lett.*, vol. 91, p. 246804, Dec 2003.

[58] P. W. Brouwer, "Rectification of displacement currents in an adiabatic electron pump," *Phys. Rev. B*, vol. 63, p. 121303, Mar 2001.

[59] G. Ferrari, L. Fumagalli, M. Sampietro, E. Prati, and M. Fanciulli, "dc modulation in field-effect transistors operating under microwave irradiation for quantum readout," *Journal of Applied Physics*, vol. 98, no. 4, pp. –, 2005.

[60] S. P. Giblin, M. Kataoka, J. D. Fletcher, P. See, T. J. B. M. Janssen, J. P. Griffiths, G. A. C. Jones, I. Farrer, and D. A. Ritchie, "Rectification in mesoscopic alternating current-gated semiconductor devices," *Journal of Applied Physics*, vol. 114, no. 16, pp. –, 2013.

[61] V. Kashcheyevs and B. Kaestner, "Universal decay cascade model for dynamic quantum dot initialization," *Phys. Rev. Lett.*, vol. 104, p. 186805, May 2010.

[62] R. H. Brown and R. Twiss, "Correlation between photons in two coherent beams of light," *Journal of Astrophysics and Astronomy*, vol. 15, no. 1, pp. 13–26, 1994.

[63] M. Moskalets and M. Büttiker, "Spectroscopy of electron flows with single- and two-particle emitters," *Phys. Rev. B*, vol. 83, p. 035316, Jan 2011.

[64] Y. Ji, Y. Chung, D. Sprinzak, M. Heiblum, D. Mahalu, and H. Shtrikman, "An electronic mach–zehnder interferometer," *Nature*, vol. 422, no. 6930, pp. 415–418, 2003.

[65] G. Yamahata, K. Nishiguchi, and A. Fujiwara, "Gigahertz single-trap electron pumps in silicon," *Nature communications*, vol. 5, 2014.

[66] A. Fuhrer, C. Fasth, and L. Samuelson, "Single electron pumping in inas nanowire double quantum dots," *Applied Physics Letters*, vol. 91, no. 5, p. 052109, 2007.